Politecnico di Torino

Corso di Laurea Magistrale in Ingegneria Aerospaziale

Anno Accademico 2024-2025

Sessione di Laurea Ottobre 2025

Finite Element Simulation of drilling in titanium alloy plates

Burr Formation and Structural Implications

Relatore: Professor Marco Gherlone

Candidato: Lorenzo Bettinardi

Contents

List of Figures

List of Tables

1 Introduction

Burrs are unwanted material projections generated during manufacturing operations, deviating from the ideal geometry of the workpiece. Machining burrs typically form on free edges after processes such as milling, drilling, turning, or grinding. The operation aimed to remove burr is known as *deburring*.

The effect of not removing burrs has been widely investigated in the literature due to their detrimental impact on both components and processes. From a structural point of view, burrs seem to reduce mechanical strength under fatigue loading [26]. On a functional level, they may interfere with part assembly, causing misalignments or angular deviations. Additionally, burrs can damage protective coatings, lowering their resistance against corrosion. They are often associated with other defects, such as subsurface cracks, excessive surface roughness, or interface contamination. These effects are especially critical in mechanically fastened assemblies. Burrs may also complicate subsequent manufacturing steps, including machining, surface treatments, and assembly/disassembly operations. For these reasons, deburring is a common industrial practice. However, it represents a non-value-added activity, since it does not directly increase the final value of the product. Moreover, deburring can alter edge geometry and surface quality, and it entails significant costs. Depending on the source, deburring may account for between 5% and 30% of the overall manufacturing cost [5, 8, 22, 28, 31, 39]. Such expenses are largely driven by the manual, labor-intensive, and difficult-to-automate nature of the operation, particularly for small, high-precision components [43]. As a result, manpower requirements, cycle time, rejection rates, and machine downtime increase [5]. Burr prevention or minimization through process optimization should be investigated.

Drilling operations represent one of the most common machining processes in the aerospace industry. For example, the structure of a fighter jet requires about 3,000 drilled holes, while a civil aircraft may require between 1.5 and 3 million [51]. These holes typically serve to mechanically fasten stacks of plates made of lightweight alloys such as aluminum or titanium, or hybrid stacks combining metals and composites. Current aerospace manufacturing standards require drilling burrs to remain below 100 μm in height [37].

Mechanical fastening in aeronautics generally follows a standardized multi-step procedure. Among the five phases involved, only three add value to the final product [55]. Pre-assembly and intermediate disassembly steps are required for cleaning and deburring and do not contribute to product value. An alternative approach, known as One-Shot or One-Way-Assembly, eliminates these non-value-added steps by drilling the holes directly during assembly, without separation for cleaning or deburring. This method reduces costs and lead times, simplifies production planning, and facilitates automation, since manual deburring is no longer necessary. The process has been recognized and adopted by major aircraft manufacturers such as Boeing [44, 77] and Airbus [80], and is also considered highly promising for future military aircraft production. Figure 1.1 represents schematically the phases of the two different procedures. Nevertheless, One-Way-Assembly involves significant challenges. Skipping deburring raises the risk of interface contamination due to burr formation and chip entrapment, which may critically affect the mechanical strength of joints [15, 24, 44]. To mitigate these risks, precise control of drilling conditions, particularly clamping to minimize inter-part gaps, is essential. Additionally, non-destructive inspection methods capable of detecting small contaminations on non-accessible surfaces, as well as robust engineering assessment tools to evaluate their impact, are needed. Addressing these challenges remains one of today's key industrial priorities.

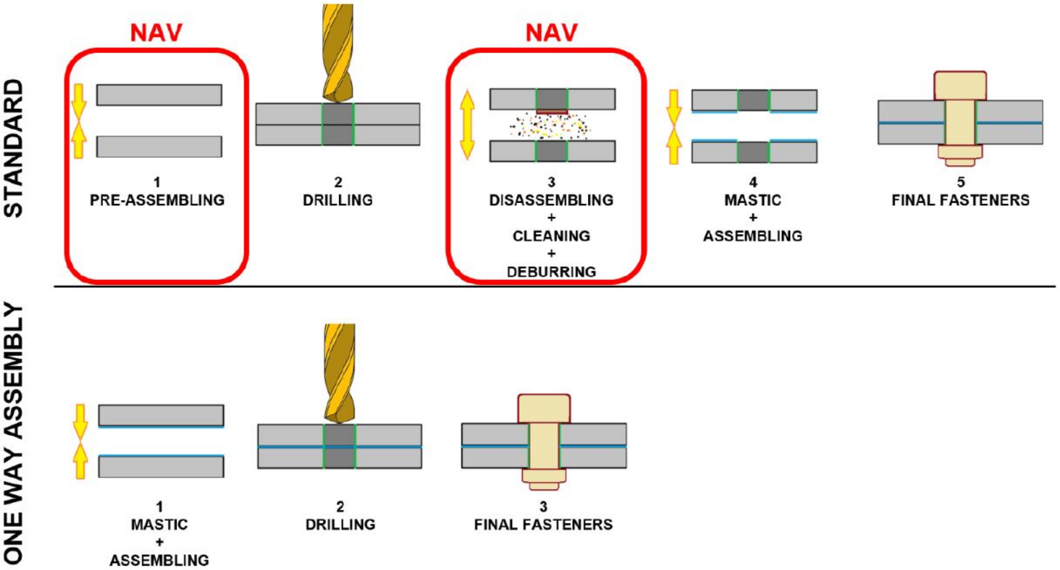

Figure 1.1: Standard and One Way Assembly processes [16]

Research on machining burrs has a long history. Since the 1940s, numerous studies have focused on burr formation, chip generation, and geometrical classification across different processes [56]. From the 1980s onward, analytical models of burr formation began to emerge [13, 47], while investigations specifically addressing drilling of stacked materials only appeared after the 2000s. The predominant research focus has been the optimization of manufacturing parameters to reduce burr size and, in turn, lower deburring costs. Despite this extensive body of work, there is still limited knowledge on how burrs affect the mechanical behavior of structures. Experimental studies confirm that burrs negatively influence both static and fatigue strength [26], yet very few works have quantified or explained the mechanisms behind this detrimental effect.

This thesis reports the work conducted during an internship at Institut Clément Ader (Toulouse), within the framework of the PhD research of Santiago Frutos Taravillo. In his work, he conducted fatigue tests on Ti6Al4V specimens with different burr sizes to study the effect of burrs on fatigue for open hole specimens. The purpose of this project is to develop a finite element numerical model capable of reproducing the entire specimen manufacturing process. The model is first validated in terms of the drilling forces and torques, and subsequently with respect to the burr geometry obtained. Once validated, the three-dimensional residual stress field resulting from the drilling operation is extracted and used as input for a second finite element model simulating the fatigue loading conditions. This approach enables the numerical evaluation of the effect of drilling-induced residual stresses on the fatigue life of the material. In conclusion, the work carried out consists in developing a finite element model to reproduce burr formation during drilling in titanium and to extract the corresponding residual stress field, together with a second finite element model to assess the impact of these stresses on the fatigue behavior of the component.

2 State of the Art

2.1 Burr geometry and geometrical characterization

There is no single, universally accepted definition of a burr. The ISO 13715 standard [42], which focuses on edge quality, defines a burr as a rough projection of material beyond the ideal geometrical shape of an external edge, typically resulting from a machining or forming process. A definition of burr size is also provided in Figure 2.1. However, burr morphology and location can vary considerably, which is not captured by this standard definition. Other sources emphasize that burrs are formed due to plastic flow of material during cutting or shearing operations [7, 11, 40, 46, 47, 67]. Incorporating this concept, a more general definition can be stated: a burr is a rough projection of material beyond the ideal edge geometry, resulting from the plastic flow induced by machining operations.

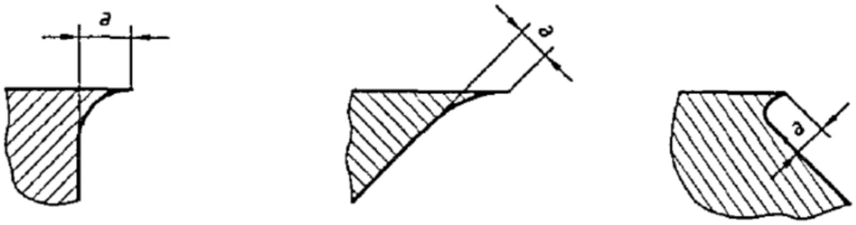

Figure 2.1: ISO 13715 burr size definition [42]

In the context of composite materials, burrs can be defined simply as any measurable excess material left on the part. These defects are typically different from burrs formed during metal machining, as illustrated in Figure 2.2.

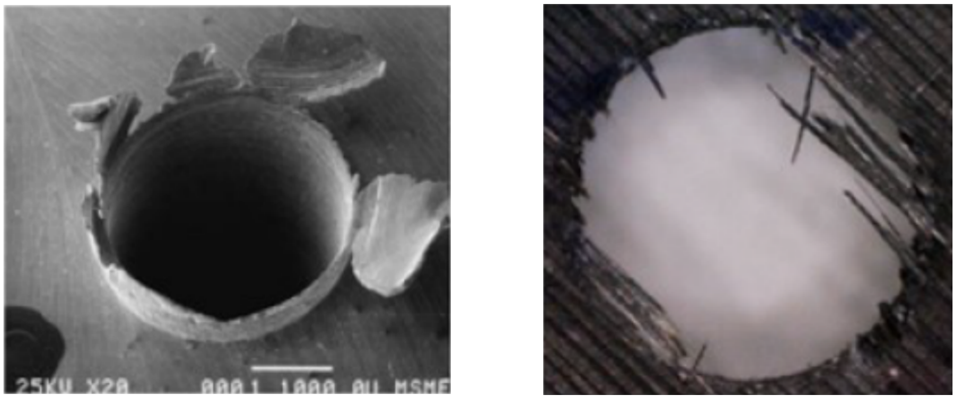

(a) Metallic Burr

(b) Composite Burr

Figure 2.2: Burr for different materials [19]

To assess the impact of a burr, both qualitatively and quantitatively, it is necessary to describe its geometry with specific parameters. Ideally, a small set of measurable characteristics would suffice to quantify the burr and evaluate its effect on structural performance. In reality, burr geometry is highly variable and influenced by multiple factors, so there is no universal characterization method. The level of detail used depends on the study's purpose. In the literature, three levels of drilling burr characterization are reported [19], but this work considers only the lowest level, which is sufficient for the intended analysis.

This approach describes the 2D profile of the burr using a small set of parameters, as proposed by Schafer [74] (Figure 2.3). While this idealized geometry simplifies the characterization, in practice, only two parameters, height and thickness, are widely used, and sometimes even the height alone is employed.

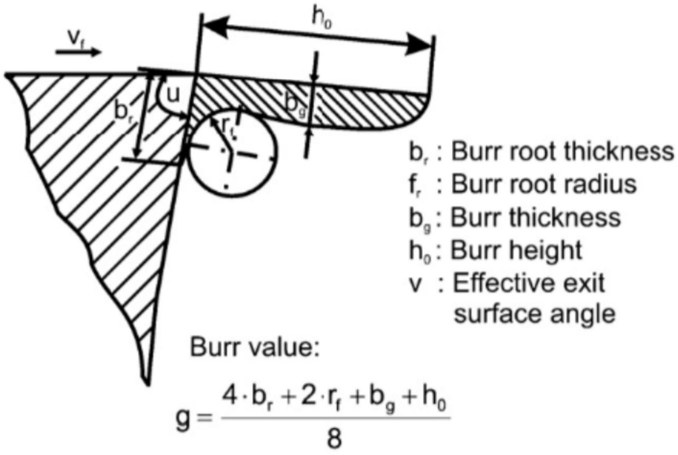

Figure 2.3: Burr profile parametrization by Schafer [74]

Even these parameters lack a universal definition. According to Aurich [6], the burr height is the distance from the nominal workpiece edge to the highest point of the burr cross-section, which aligns with most literature conventions. Burr thickness, following Schafer [74] and Aurich [6], is defined as the thickness parallel to the burr root at a distance equal to the tangent circle radius, measured in cross-section. This definition can be difficult to apply in practice. An alternative is to define thickness as the maximum radial distance of the burr from the nominal hole surface at a given fraction of the burr height.

It is important to note that this geometrical description considers only a single radial profile. When burr height or thickness varies circumferentially, multiple measurements at equidistant points around the hole are typically taken. A statistical value (maximum, mean, or median) is then used to represent burr height and thickness with a single value.

2.2 Burr classification

Given the considerable diversity in burr morphology, a correct classification of machining burrs is essential. Such a classification helps in understanding the underlying formation mechanisms, assessing the potential impact of specific burrs on subsequent deburring operations, and evaluating their influence if left unremoved. Three criteria have been proposed in the literature for classifying burrs.

1. Classification by **formation mechanism**

   This classification is applicable across all machining types. Gillespie [32] identified four distinct mechanisms, resulting in four corresponding burr types (Figure 2.4 and Table 2.1): Poisson burr, rollover burr, tear burr and cut-off burr. While this classification provides valuable insight into the physics of burr formation, it is rarely applied in practice because multiple mechanisms often act simultaneously during the formation of a single burr [32].

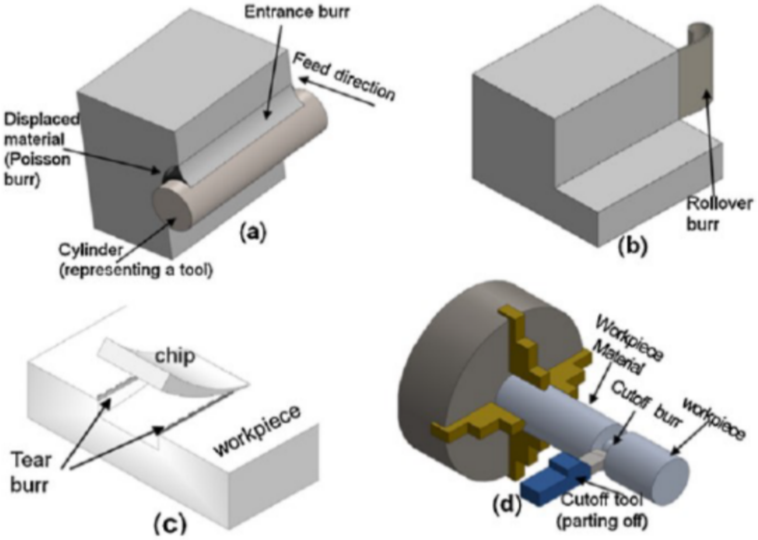

Figure 2.4: (*a*) Poisson burr (b) Rollover burr (c) Tear burr (d) Cut-off burr [76]

Formation Mechanism	**Burr classification**
Lateral extrusion	Poisson burrs
Chip plastic bending and rotation	Rollover burrs
Tearing or failure in shear	Tear burrs
Separation of the workpiece from raw material before the separation cut is finished	Cut-off burr

Table 2.1: Burr classification according to formation mechanism

2. Classification by **burr location**

   Burr location often is linked to with the dominant formation mechanism [6]. For drilling operations, which are the focus of this study, burrs are typically classified as entry or exit burrs, with exit burrs generally being larger, thus requiring a greater deburring effort. When multiple plates are drilled together, interface burrs can also form at the contact surfaces of the mating parts.

3. Classification by **morphology**

   For drilling, Kim et al. [45] proposed a distinction between uniform, crown, and transition burrs (Figure 2.5). Ko and Lee [48] introduced a similar three-type system (A, B, and C) corresponding to uniform burrs without a drill cap, uniform burrs with a drill cap, and non-uniform burrs with a drill cap, respectively (Figure 2.6). The drill cap is a portion of material that remains attached to the burr while rotating. Dornfeld et al. [23] presented a four-type classification (types I–IV: uniform burrs, lean-back burrs, rolled-back burrs, and rolled-back burrs with widened exit) shown in Figure 2.7. Newman [60] offered yet another morphological classification, identifying curling burrs, triangular burrs, and bulge burrs (Figure 2.8).

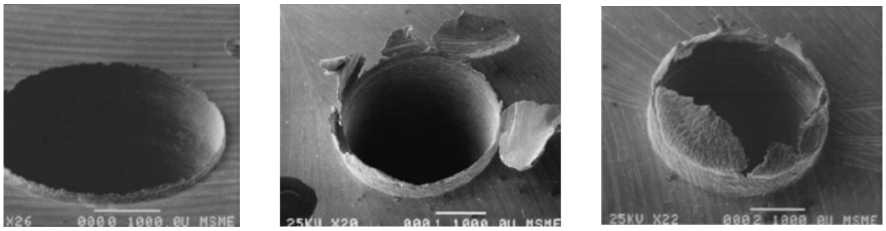

(a) Uniform Burr (b) Transient Burr (c) Crown Burr

Figure 2.5: Drilling burr types from Kim et al. [45]

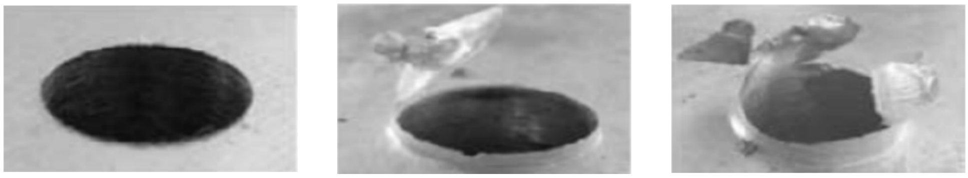

(a) Uniform Burr without cap (b) Uniform Burr with cap (c) Burst Burr with cap

Figure 2.6: Drilling burr types from Ko and Lee [48]

2.3 Burr formation

Burr formation has been extensively studied due to the industrial interest in developing predictive models capable of estimating burr size and mechanical effects under different machining conditions. Such models enable process optimization to minimize or even eliminate the need

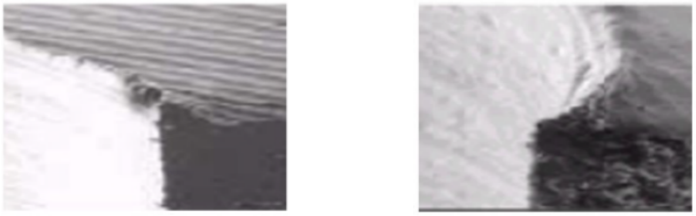

(a) Uniform Burr (b) Uniform leaned back burr

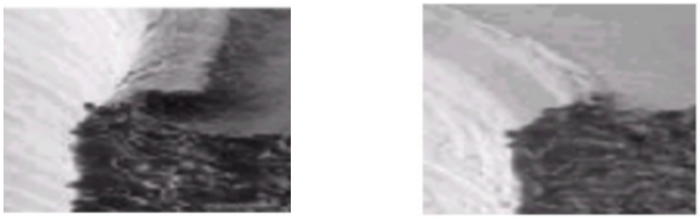

(c) Rolled back Burr (d) Rolled back Burr with widened exit

Figure 2.7: Drilling burr types from Dornfield et al. [23]

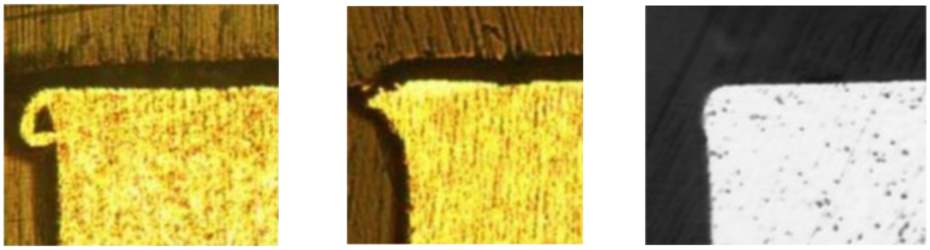

(a) Curling Burr (b) Triangular Burr (c) Bulge Burr

Figure 2.8: Drilling burr types from Newman [60]

for deburring. Additionally, predictive models allow engineers to assess, in advance, the post-machining material state and the potential impact of burrs on structural performance.

This section first examines the main burr formation mechanisms identified in the literature (previously summarized in Table 2.1) and then discusses the mechanics of burr formation in both orthogonal cutting and drilling.

2.3.1 General burr formation mechanisms

Gillespie's extensive experimental studies [29, 30, 32] identified three fundamental burr formation mechanisms, depicted in Figure 2.9.

- **Lateral extrusion (Poisson burrs)**

  In this mechanism, contact between the tool and workpiece causes local material compression, which may result from pressure at the effective cutting edge, flank surface, lateral tool face, or initial tool indentation. To satisfy plastic incompressibility, material is forced outward and remains plastically deformed after the load is removed. Burrs formed in this way are known as Poisson burrs, driven by the Poisson effect.

- **Plastic bending (Rollover burrs)**

  Here, the material bends plastically rather than shearing when the energy required to bend the chip is less than that required to cut it. The chip rotates around a plastic hinge, forming a rollover burr. This is the dominant mechanism observed in orthogonal cutting operations.

- **Plastic tearing (Tear burrs)**

  This mechanism involves shearing through plastic flow, where material undergoes both bending and pure shear, resulting in a tear burr.

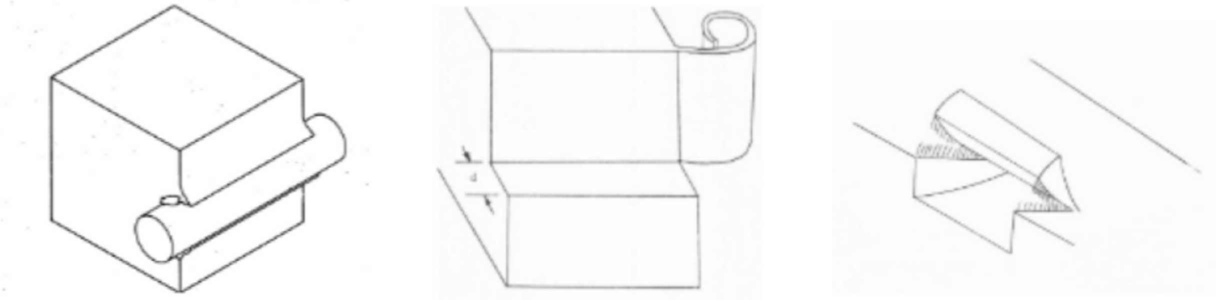

(a) Lateral Extrusion

(b) Plastic Bending

(c) Plastic Tear

Figure 2.9: Burr formation mechanisms from Gillespie [32]

While these mechanisms are useful for understanding the physics behind burr formation, it is common in practice for multiple mechanisms to act simultaneously during burr generation.

2.3.2 Orthogonal cutting burr formation mechanics

Orthogonal cutting is defined as a two-dimensional machining process under plane strain conditions, where the cutting edge of the tool is perpendicular both to the relative motion between tool and workpiece and to the side face of the workpiece. As the simplest machining operation, it has been extensively studied in the literature and is often used as a first step to understand burr formation in more complex processes such as drilling. Indeed, some authors have approached the drilling problem by modeling it as a local orthogonal cutting operation, where the cutting angles vary dynamically along the tool edges.

The mechanics of orthogonal cutting have been divided into four main stages. These stages have been experimentally observed using Scanning Electron Microscopy (SEM) [57],and corroborated by finite element simulations through accumulated plastic strain contours [26] (Figure 2.10).

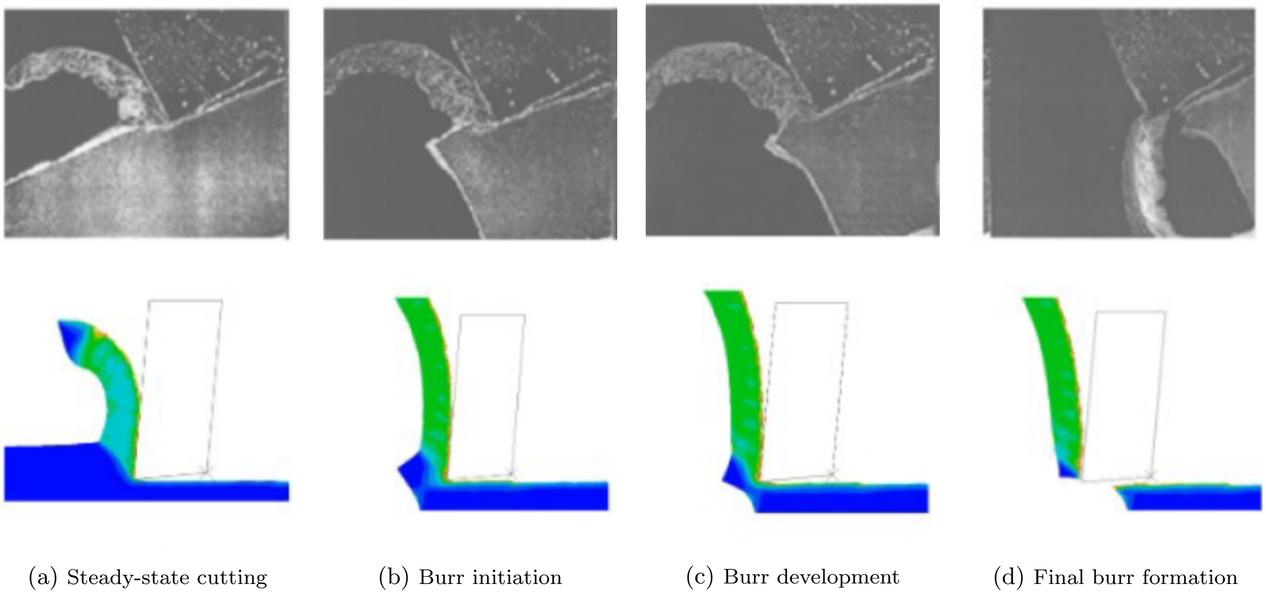

(a) Steady-state cutting (b) Burr initiation (c) Burr development (d) Final burr formation

Figure 2.10: Burr formation stages in orthogonal cutting - Experimental [57] and FEM simulation [26, 60]

1. Steady-state cutting (Figure 2.10a):

   In this initial stage, material removal occurs primarily through concentrated shear along the primary shear zone [56, 66]. The size and orientation of this zone depend on both cutting conditions and tool–workpiece geometry. A secondary shear zone forms near the rake face, where complex thermo-mechanical interactions occur between the chip and the tool. Plastic deformation is therefore concentrated within the shear zones and just ahead of the tool tip, while the rest of the workpiece material remains elastic (see representative schematic in Figure 2.11).

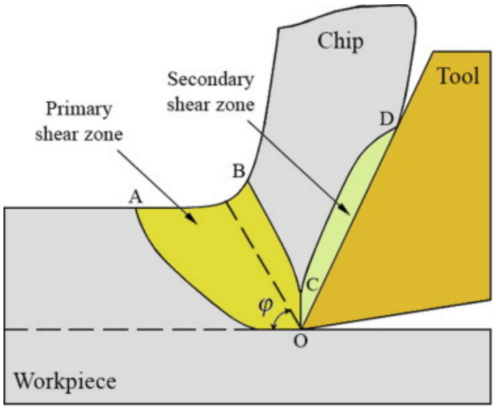

Figure 2.11: Shear zones in orthogonal cutting [4]

2. Burr initiation (Figure 2.10b):

   As the tool approaches the end surface of the workpiece, the elastic stress and strain fields extend to the free edge, producing elastic bending. With increasing intensity, this bending reaches plastic conditions, initiating localized deformation at the workpiece edge. At this point, a new negative shear zone forms, connecting the plasticized region near the tool tip with the plastified edge surface. Originally proposed by Iwata et al. [54], this third shear zone has since been widely recognized as the region where the dominant mechanisms of burr formation occur. Its existence has been confirmed both experimentally through SEM [26, 37, 55] and numerically via FEM [38, 53, 57].

3. Burr development:

   During this stage, a distribution of normal stresses develops along the negative shear zone, driving plastic bending (Figure 2.12). As a result, the uncut material at the edge undergoes a plastic rotation under near-incompressible conditions, gradually displacing the material outward and forming the precursor of the burr [47].

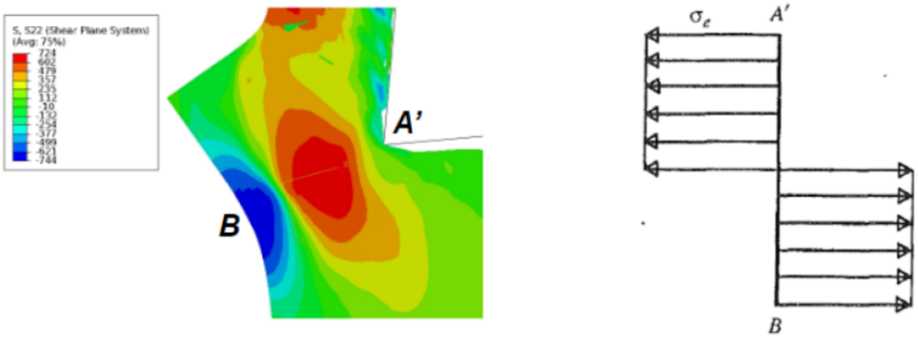

(a) FEM

(b) Graphical [47]

Figure 2.12: Burr development stage: plastic bending normal stress distribution

4. Tool exit and final outcome:

   The final stage occurs when the tool leaves the workpiece. The material's ductility plays a decisive role in the outcome:

   - For ductile materials, the process leads to the formation of a final burr. The chip separates along the same direction as steady-state cutting, leaving behind a protrusion of plastically deformed material.
   - For less ductile or brittle materials, the edge may fail through edge breakout, producing a rough chamfer instead of a burr. According to Chern [12], two mechanisms can cause edge breakout: (i) normal stresses perpendicular to the negative shear plane, opening a crack via mode I propagation, or (ii) shear stresses along the same plane, promoting mode II propagation. In the latter case, micro-burrs may still form due to friction effects during crack propagation.

Overall, these four stages highlight that ductility is the key factor determining whether burrs or edge breakout occur during orthogonal cutting.

2.3.3 Drilling burr formation mechanics

Before describing the burr formation process, it is useful to define the main parts of a twist drill, which will be frequently referenced in this section. Figure 2.13 illustrates the geometry of a standard twist drill [1], with its most relevant features labeled.

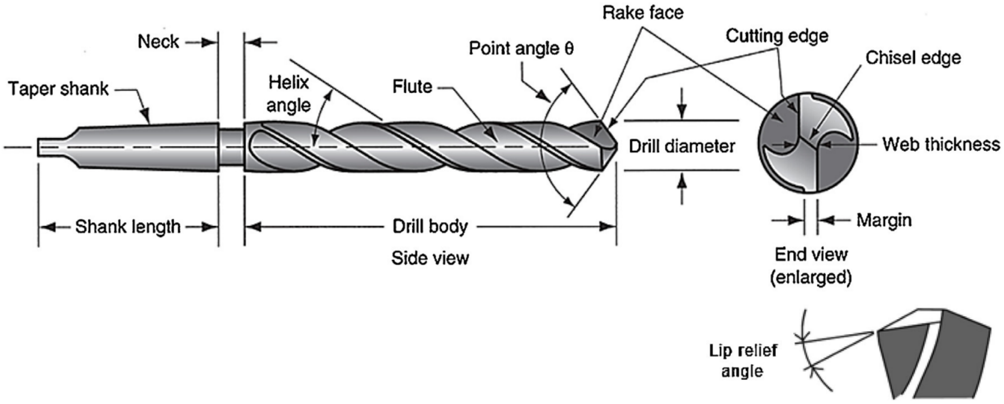

Figure 2.13: Geometry of twist drill [1]

Burr formation during drilling is a non-axisymmetric, three-dimensional process, strongly dependent on the cutting conditions and on the detailed geometry of the tool. Unlike other machining operations, its study is particularly challenging, since the cutting zone is not directly accessible and therefore difficult to observe experimentally [52].

Entry burr formation

Entry burrs are generally smaller than exit burrs. Two main mechanisms, acting simultaneously, have been identified:

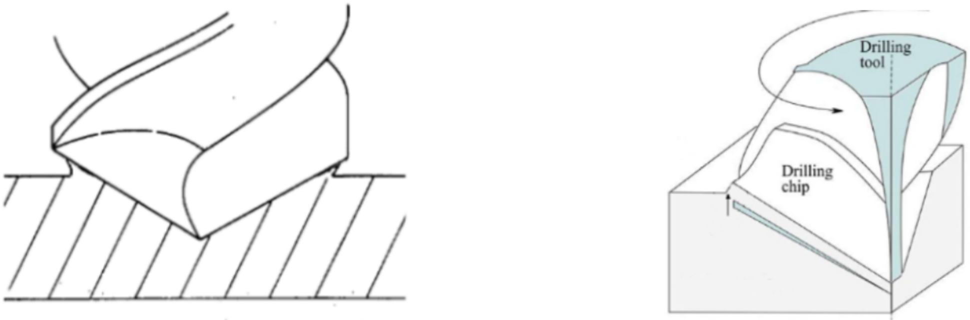

(a) Poisson effect [29]

(b) Pure shear [37]

Figure 2.14: Entry burr formation mechanism

- Lateral extrusion at drill margins (Figure 2.14a).

  This mechanism corresponds to the Poisson burr formation described by Gillespie [32]. It results from local compression of the material by the drill margins, and becomes more significant when the tool flanks are worn.

- Vertical shear (Figure 2.14b).

  As the cutting lips penetrate the workpiece, the chip begins to move upward along the flanks of the drill. While still attached to the hole edge, this upward displacement generates a vertical shear state that plastically deforms the material near the entry edge. When the chip is eventually torn away, a tear burr remains at the entry surface [29, 32, 36].

These mechanisms have not been thoroughly validated experimentally or numerically in the literature.

Exit burr formation

Exit burrs have been studied much more extensively, as they are typically larger, more irregular, and more detrimental to both deburring effort and structural performance. Their formation has been divided into four main stages:

1. Steady-state cutting (Figure 2.16).

   This stage starts once the tool has fully penetrated the material. Cutting conditions vary locally across the drill bit: the chisel edge mainly produces indentation, with material displaced outward due to the Poisson effect, while the flanks and lip regions behave as oblique cutting operations with variable angles, forces, and speeds [49, 74]. This complexity is often simplified by treating flank cutting as local 2D orthogonal cutting under changing conditions. Ahead of the drill tip, an elastic compression zone develops, which extends to the exit surface. Close to the tool edge, this zone transitions to plastic deformation.

2. Initiation (Figure 2.16a).

   When plastic deformation reaches the exit surface, a bulge forms ahead of the drill tip. This corresponds to the same initiation mechanism identified in orthogonal cutting. Interrupted drilling tests, such as those by Debard [17], clearly show this bulge development (Figure 2.15).

Figure 2.15: Drilling plastic bulge evolution at exit surface [17]

3. Development (Figure 2.16b).

   The plastic bulge enlarges as the affected zone of compression and shear migrates toward the exit surface, progressively displacing material outward.

4. Final formation (Figure 2.16c).

   The breakthrough and final burr shape occur in three sub-stages [50, 51, 65, 69, 73, 78]:

   - Drill breakthrough (Figure 2.16d). The thrust force causes fracture beneath the drill tip, producing a drill cap, which may detach or remain attached to the workpiece.
   - Plastic bending (Figure 2.16e). The remnant material rotates around a plastic hinge near the hole edge, undergoing elongation by shear and bending, similar to entry burr formation.
   - Final fracture (Figure 2.16f). If fracture occurs at the drill edges, a well-defined burr forms. Otherwise, a more irregular crown burr results.

(a) Steady-State cutting (b) Burr initiation (c) Burr development

(d) Drill breakthrough (e) Burr plastic bending (f) Final burr formation

Figure 2.16: Drilling exit burr formation stages [57]

Thrust force is the primary driver of exit burr formation [18]. Material ductility and local temperature rise (from friction and plastic work) promote larger and more irregular burrs. Microstructural studies (Figure 2.17) confirm significant strain hardening in burr material, evidenced by refined grain size and higher hardness values. Residual stresses in the burr region are typically complex, with both tensile and compressive components [75].

Industrial practices such as step drilling [54] and post-drilling reaming [29] often partially remove burrs or alter their morphology, modifying the material conditions near the hole edge.

Interface burr formation

In stack drilling, where two or more plates are drilled simultaneously, interface burrs form at the contacting surfaces. These are characterized by the simultaneous generation of an exit burr on the upper plate and an entry burr on the lower one. Their development is constrained

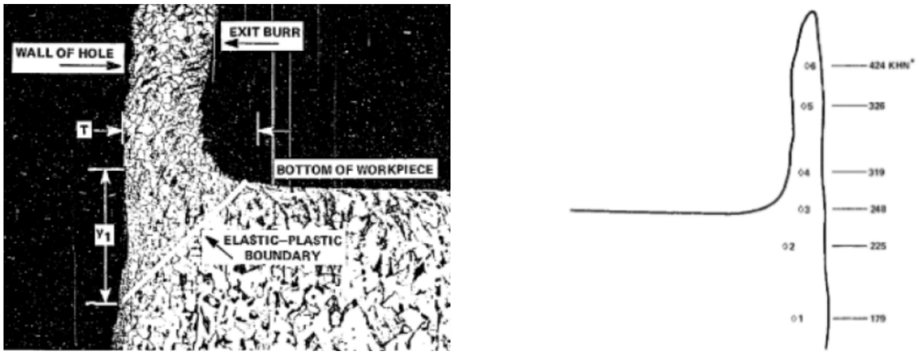

(a) Microstructural evolution in burr zone (b) Hardness evolution in burr zone

Figure 2.17: Micrographic cross-section [19]

by the nearby backup surface, which tends to favor lateral bulging of the displaced material [36, 38].

The key factor influencing interface burrs is the gap between plates. Ideally, this gap should be zero, but in practice it may result from imperfect positioning, lack of parallelism, insufficient clamping, or deformation under the thrust force [67, 68, 77, 82]. Even if negligible initially, the applied thrust force can increase separation during drilling, thus enlarging the space for burr growth and promoting chip entrapment between plates [55].

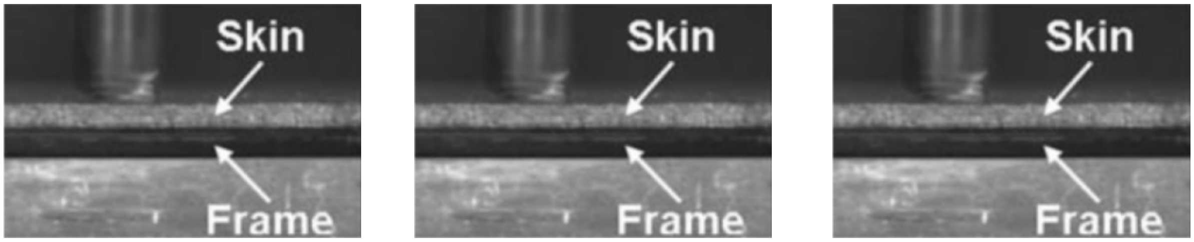

(a) Steady-State cutting (b) Drill breakthrough (c) Entry and exit interface burrs formation

Figure 2.18: Drilling interface burr formation stages [55]

The process can be divided into five stages:

1. Steady-state cutting of the upper plate (Figure 2.18a). Similar to free-surface exit burrs, but accompanied by elastic bending of the plates due to thrust force.
2. Breakthrough of the upper plate (Figure 2.18b). The first plate experiences spring-back, while the thrust force further opens the inter-plate gap.
3. Simultaneous burr formation. An exit burr develops on the upper plate, while an entry burr forms on the lower plate. In some cases, the exit burr of the first plate may penetrate into the second (Figure 2.18c), particularly if the lower plate has low transverse strength.

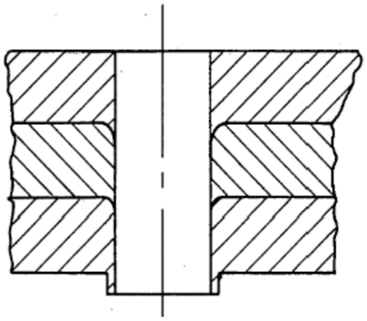

Figure 2.19: Interface burr penetrating backup plate in multi-stack material [26]

4. Advancement and spring-back. As drilling progresses, the plates attempt to return to their original position, crushing the newly formed burrs.
5. Final morphology. The result depends on the interplay between thrust force, gap size, and material properties, often yielding irregular burrs at the interface.

Since direct observation is not possible, experimental verification of interface burr formation is more challenging than for orthogonal cutting. Nevertheless, methods such as high-speed imaging of the exit surface [25], interrupted tests [17, 65], and monitoring of thrust force and torque profiles [27, 70, 79] have been used successfully to identify stages and validate both theoretical and numerical models of interface burr growth.

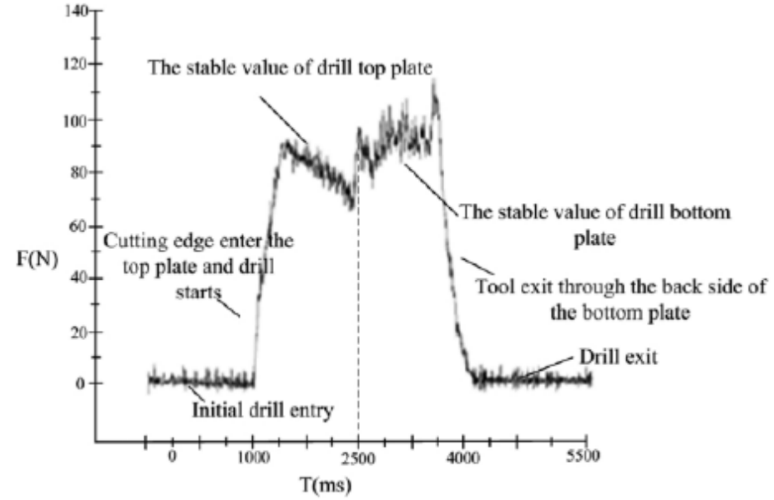

Figure 2.20: Drilling thrust force profile for bi-metallic stack drilling surface [83]

2.4 Modeling of burr formation

The development of burr formation models is of great relevance for both industry and research, as they enable the assessment of how machining parameters influence burr generation without incurring the high costs of extensive experimental campaigns. Accurate burr formation models can also provide reliable predictions of burr size and the post-machining condition of the workpiece.

In the literature, three main modeling approaches can be distinguished: data-driven, mechanistic, and hybrid (fusion) models. Data-driven approaches rely on databases of experimental results and range from simple regressions to advanced machine learning algorithms. While they can yield accurate predictions under specific conditions, they do not capture the underlying physical mechanisms of burr formation and their reliability depends heavily on the quality and extent of the calibration data.

By contrast, mechanistic models aim to reproduce the physics of burr formation. These can be classified as analytical or numerical, with the latter being the focus of this project and discussed in detail below. Fusion models combine both philosophies: they start from a simplified physical formulation and then incorporate elements from data-driven approaches.

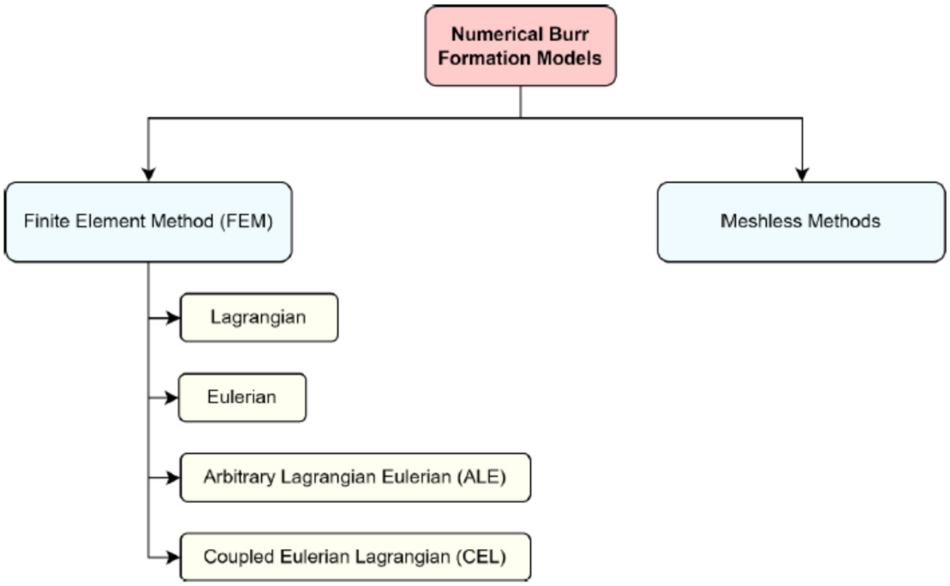

Figure 2.21: Numerical burr formation models classification [16]

Analytical models are derived from simplified formulations of burr formation mechanics, typically based on material behavior theories [26]. Despite their name, these models often require numerical techniques for their solution. They have been widely studied for various machining processes, particularly 2D orthogonal cutting and drilling. In drilling, distinct analytical formulations are required for entry, exit, and interface burrs. Literature shows limited development of models for entry burrs, somewhat more for interface burrs, while exit burr formation has received the most attention.

This project, however, focuses on numerical models. These rely on explicit simulations where time-integration schemes replace the step-by-step iterative convergence typical of implicit methods [81]. Such an approach is well suited to machining simulations, as it significantly reduces computation time when dealing with the highly dynamic problems of cutting, which involve large deformations and displacements.

Numerical burr formation models can be divided into two major categories depending on the computational method employed: Finite Element Method (FEM) models and meshless models. FEM is by far the most widely adopted in machining simulations, whereas meshless methods eliminate the mesh altogether, avoiding issues related to distortion that often arise in FEM.

2.5 Finite elements modeling

Within FEM-based approaches (Figure 2.21), different mesh strategies exist:

- Lagrangian models: the mesh is attached to the deforming workpiece material, and deforms accordingly. This is the most common approach found in literature for chip and burr formation [53, 71].
- Eulerian models: the mesh is fixed in space, a strategy typical in Computational Fluid Dynamics (CFD). While rarely applied in machining, this method avoids mesh distortion problems.
- Arbitrary Lagrangian–Eulerian (ALE) models: employ an adaptive mesh that continuously adjusts to the material's deformation. This reduces distortion but increases computational cost.
- Coupled Eulerian–Lagrangian (CEL) models: combine both strategies, using an Eulerian region for large-deformation areas and a Lagrangian mesh for less critical regions.

Among machining operations, 2D orthogonal cutting has been the most widely studied for predictive modeling of burr formation, due to its relative simplicity. Both analytical and numerical models are extensively documented. Numerical models have been used not only for burr formation but also for edge breakout, as demonstrated by Hashimura et al. [35]. Park and Dornfeld [63, 64] developed a Lagrangian model that explored different damage initiation and evolution criteria to capture burr formation stages and studied the influence of rake angle and backup material. Many other Lagrangian studies can be found [20, 72, 75]. ALE approaches have also been proposed, such as Huang et al. [40], who investigated rake angle, tool edge, and cutting speed in micro-cutting. Movahhedy et al. [58, 59] highlighted ALE's advantages over pure Lagrangian models due to reduced mesh distortion.

For drilling burr formation, which is inherently more complex than 2D orthogonal cutting because of its three-dimensional nature and the role of tool geometry, research has also been extensive. The degree of coverage varies depending on the burr type—entry, exit, or interface.

- Entry burrs: Few models exist. Choi et al. [15] proposed a Lagrangian FEM model, though results remain unvalidated. Abdelhafeez et al. [2] developed a CEL model for aluminium and titanium, validated against experiments, with accurate predictions of burr height under different cutting speeds.
- Exit burrs: This category has been studied most extensively. All FEM strategies (Lagrangian, ALE, CEL) have been employed. Guo and Dornfeld [33] proposed a Lagrangian model with variable ductile damage criteria adapted to burr formation stages. Min et al. [57] predicted drilling thrust force in steady-state cutting, though not during burr formation. Other works include Isbilir and Ghassemieh [41], Abdelhafeez et al. [2], and Gajrani et al. [27], with models validated for burr height, cutting forces, and torque in titanium drilling. Non-Lagrangian approaches also exist, such as the ALE model by Efstathiou et al. [25], validated experimentally, and CEL simulations from Abdelhafeez et al. [2], which showed strong agreement with experiments.
- Interface burrs: Some studies address the prediction of the gap's evolution during drilling. Choi and Min [14] developed a Lagrangian model, while Choi et al. [15] provided thrust force predictions validated against experiments, with rough predictions of burr geometry (height and thickness).

In this section, the constitutive laws reported in the literature are presented. These equations are implemented in numerical codes to describe the underlying physics of the problems.

2.5.1 Plasticity Models

Plasticity models define the behavior of the material once plastic deformations are obtained.

- **Ludwick law**

  It is the simplest plasticity law. It considers plastic deformation as the sole cause of strain hardening. As a result, there is a direct correspondence between the strain value and the stress. According to Harzallah's thesis [34], the range of strain on the test should not exceed 0.7.

  $$\sigma = A + B \cdot \varepsilon_p^n \tag{2.1}$$

  The equation's parameters 2.1 represents:

  - A: Flow stress at zero plastic strain
  - B: Strain-hardening module
  - n: Strain-hardening exponent

- **Johnson-Cook law**

  The Johnson–Cook law is by far the most widely used in the literature. It accounts for the effects of strain rate and temperature on plasticization. These terms appear as multiplicative factors of the Ludwick law, keeping the overall formulation relatively simple.

$$\sigma_y = [A + B \cdot \varepsilon_p^n] \left[1 + Cln\left(\frac{\dot{\varepsilon}_p}{\dot{\varepsilon}_0}\right)\right] \left[1 - \left(\frac{T - T_0}{T_f - T_0}\right)^m\right] \tag{2.2}$$

  The new parameters appearing are, respectively:

  - C: Strain rate sensibility
  - m: Thermal-softening exponent
  - T_f: Melting temperature
  - T_0: Reference temperature
  - $\dot{\varepsilon}_0$: Reference strain rate

  In his thesis [34], Harzallah compiles values from the literature for the Johnson–Cook model parameters for Ti6Al4V. Table 2.2 summarizes the studies considered, including the parameters from Abdelhafeez [2] and Harzallah himself.

	A $[MPa]$	B $[MPa]$	n	C	m
Johnson 1989	862	331	0.34	0.012	0.8
Lee 1998	724.7	683.1	0.47	0.035	1
Macdougall 1999	984	520.3	0.5102	0.015	0.82
Lesuer 2000	1098	1092	0.93	0.014	1.1
Nemat-Nasser 2001	1119	838.6	0.4734	0.01921	0.6437
Shivpuri 2002	870	990	0.25	0.011	1
Meyer 2001	862	331	0.34	0.012	0.8
Özel 2004	859	640	0.22	0.000022	1.1
Khan 2004	1080	1007	0.5975	0.001304	0.7701
Seo 2005	997.9	653.1	0.45	0.0198	0.7
Li 2006	968	380	0.421	0.0197	0.577
Umbrello 2008	782.7	498.4	0.28	0.028	1
Buchnak 2010	983	348	0.32	0.024	0.69
Abdelhafeez 2016	860	683	0.47	0.035	1
Harzallah 2018 (1)	838	626.92	0.394	0.0274	0.7852
Harzallah 2018 (2)	798.87	396.85	0.23	0.056	0.42

Table 2.2: Johnson-Cook model identifications for Ti6Al4V [2, 34]

- **Johnson-Cook law with modifications**

  The Johnson–Cook model has found wide application in the literature, as previously mentioned. Frequently, depending on the materials and processes considered, authors have introduced adjustments and modifications to obtain a formulation more suitable for the problem under investigation. Table 2.3 presents several notable examples taken from Debard's paper [16].

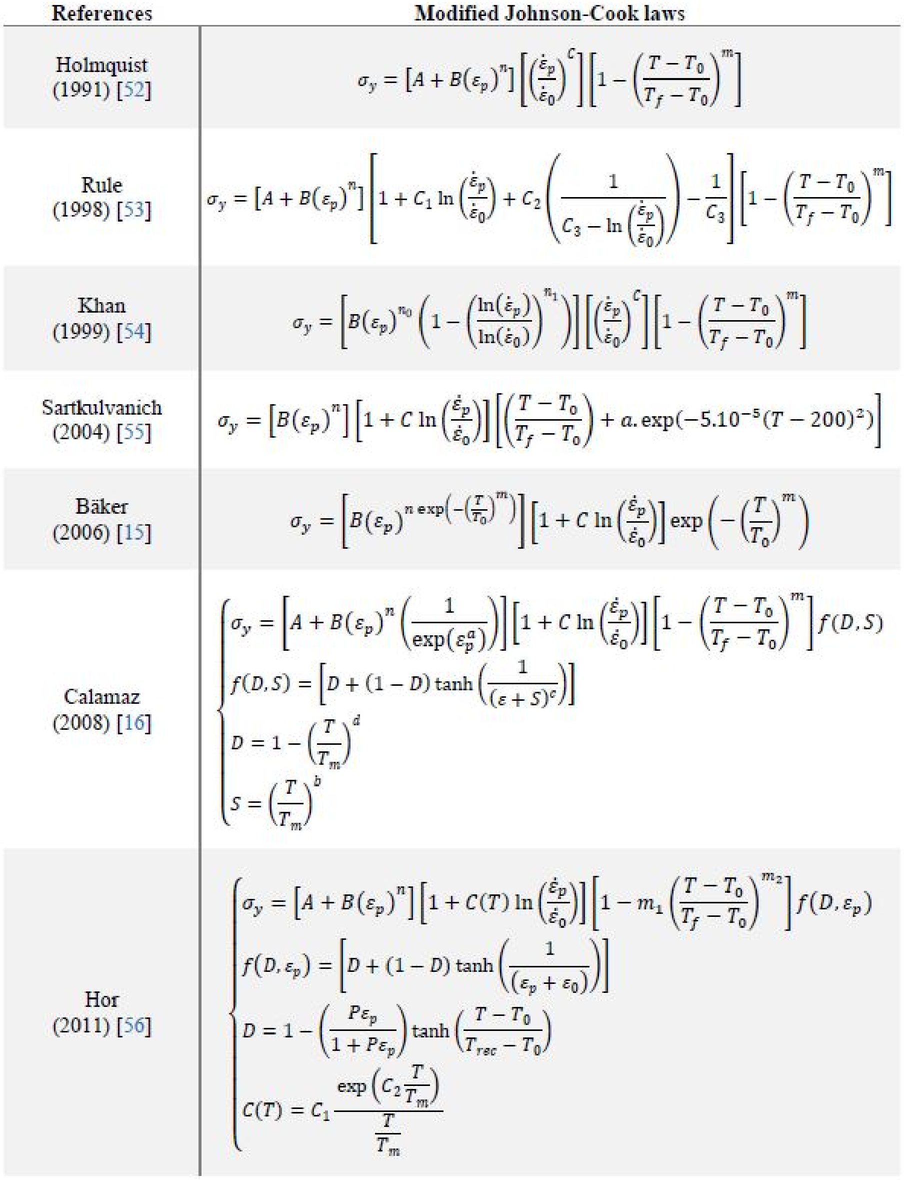

References	Modified Johnson-Cook laws
Holmquist (1991) [52]	$\sigma_y = [A + B(\varepsilon_p)^n]\left[\left(\frac{\dot{\varepsilon}_p}{\dot{\varepsilon}_0}\right)^C\right]\left[1 - \left(\frac{T - T_0}{T_f - T_0}\right)^m\right]$
Rule (1998) [53]	$\sigma_y = [A + B(\varepsilon_p)^n]\left[1 + C_1 \ln\left(\frac{\dot{\varepsilon}_p}{\dot{\varepsilon}_0}\right) + C_2\left(\frac{1}{C_3 - \ln\left(\frac{\dot{\varepsilon}_p}{\dot{\varepsilon}_0}\right)}\right) - \frac{1}{C_3}\right]\left[1 - \left(\frac{T - T_0}{T_f - T_0}\right)^m\right]$
Khan (1999) [54]	$\sigma_y = \left[B(\varepsilon_p)^{n_0}\left(1 - \left(\frac{\ln(\dot{\varepsilon}_p)}{\ln(\dot{\varepsilon}_0)}\right)^{n_1}\right)\right]\left[\left(\frac{\dot{\varepsilon}_p}{\dot{\varepsilon}_0}\right)^C\right]\left[1 - \left(\frac{T - T_0}{T_f - T_0}\right)^m\right]$
Sartkulvanich (2004) [55]	$\sigma_y = \left[B(\varepsilon_p)^n\right]\left[1 + C \ln\left(\frac{\dot{\varepsilon}_p}{\dot{\varepsilon}_0}\right)\right]\left[\left(\frac{T - T_0}{T_f - T_0}\right) + a.\exp(-5.10^{-5}(T - 200)^2)\right]$
Bäker (2006) [15]	$\sigma_y = \left[B(\varepsilon_p)^{n \exp\left(-\left(\frac{T}{T_0}\right)^m\right)}\right]\left[1 + C \ln\left(\frac{\dot{\varepsilon}_p}{\dot{\varepsilon}_0}\right)\right]\exp\left(-\left(\frac{T}{T_0}\right)^m\right)$
Calamaz (2008) [16]	$\begin{cases} \sigma_y = \left[A + B(\varepsilon_p)^n\left(\frac{1}{\exp(\varepsilon_p^a)}\right)\right]\left[1 + C \ln\left(\frac{\dot{\varepsilon}_p}{\dot{\varepsilon}_0}\right)\right]\left[1 - \left(\frac{T - T_0}{T_f - T_0}\right)^m\right] f(D, S) \\ f(D, S) = \left[D + (1 - D) \tanh\left(\frac{1}{(\varepsilon + S)^c}\right)\right] \\ D = 1 - \left(\frac{T}{T_m}\right)^d \\ S = \left(\frac{T}{T_m}\right)^b \end{cases}$
Hor (2011) [56]	$\begin{cases} \sigma_y = \left[A + B(\varepsilon_p)^n\right]\left[1 + C(T) \ln\left(\frac{\dot{\varepsilon}_p}{\dot{\varepsilon}_0}\right)\right]\left[1 - m_1\left(\frac{T - T_0}{T_f - T_0}\right)^{m_2}\right] f(D, \varepsilon_p) \\ f(D, \varepsilon_p) = \left[D + (1 - D) \tanh\left(\frac{1}{(\varepsilon_p + \varepsilon_0)}\right)\right] \\ D = 1 - \left(\frac{P\varepsilon_p}{1 + P\varepsilon_p}\right) \tanh\left(\frac{T - T_0}{T_{rec} - T_0}\right) \\ C(T) = C_1 \frac{\exp\left(C_2 \frac{T}{T_m}\right)}{\frac{T}{T_m}} \end{cases}$

Table 2.3: Modified Johnson-Cook laws [16]

- **Other formulations**

  The previously reported examples consider the effect of strain rate and temperature as a multiplicative parameter of the Ludwick law. However, in the literature, models can be found that explicitly account for the influence of these variables on the coefficients A, B, and n. One such example is the model proposed by Harzallah [34], in which Equation 2.1 becomes:

$$\sigma = A(\dot{\varepsilon}, T) + B(\dot{\varepsilon}, T) \cdot \varepsilon^{n(\dot{\varepsilon}, T)} \tag{2.3}$$

The effects of strain rate and temperature are incorporated into the coefficients of the Ludwick law. Consequently, they are no longer constant but become functions of $\dot{\varepsilon}$ e T. In particular, in his formulation, Harzallah shows that the values of these parameters can be approximated by a three-dimensional planar distribution.

2.5.2 Damage Laws

When studies about predicting ductile fracture of metals are approached, the majority of authors agrees on the three main points [21]:

- Ductile fracture is driven by plastic strain, rather than stress.
- The plastic strain at fracture depends on the state of stress.
- This dependency requires a minimum of two stress-state descriptors: one related to the first invariant, and the other one related to the third invariant.

Three different approaches have been developed to achieve a good description of the phenomenon: micro-mechanics models, thermodynamic models and empirical models. Between those ones, the empirical approaches are the simplest to implement and are the most used in literature. They intend to predict the fracture of the material, regardless of how the damage evolution has led to it. These models focus on the plastic strain evolution, so that when this parameter reaches the corresponding fracture criterion, fracture of the material occurs.

Here are presented empirical laws which describe material damage, as reported by Debard [16].

- **Oyane law**

  This model calculates the parameter I, which represent the void volume inside the material. When this parameter reaches the value 1, the fracture of the material occurs.

  $$I = \frac{1}{b} \int_0^{\overline{\varepsilon}_f} \left(1 + a \frac{\sigma_H}{\sigma_{eq}} \right) d\overline{\varepsilon}_p \tag{2.4}$$

  where:

  - σ_{eq}: Von Mises equivalent stress.
  - σ_H: Hydrostatic stress.
  - $\overline{\varepsilon}_f$: Fracture equivalent strain.

  - $d\overline{\varepsilon}_p$: Plastic equivalent strain increment.
  - a and b: Material's parameters to be identified.

- **Johnson-Cook damage law**

  This law is the most used used to model damage in cutting simulations. It is defined by the *Damage parameter* D, which is defined as the ratio between plastic strain and equivalent fracture strain:

  $$D = \sum \left(\frac{\Delta \overline{\varepsilon}^{pl}}{\overline{\varepsilon}_f^{pl}} \right) \tag{2.5}$$

  Damage occurs when $D = 1$. The equivalent plastic strain n at the onset of damage is given by:

  $$\overline{\varepsilon}_f^{pl} = \left[d_1 + d_2 exp \left(d_3 \frac{\sigma_H}{\sigma_{eq}} \right) \right] \left[1 + d_4 ln \left(\frac{\dot{\varepsilon}_p}{\dot{\varepsilon}_{p0}} \right) \right] \left[1 + d_5 \left(\frac{T - T_0}{T_f - T_0} \right) \right] \tag{2.6}$$

- **Mohr-Coulomb law**

  Fracture occurs when Equation 2.7 is verified:

  $$\tau + c_1 \sigma_n = C_{MC} \tag{2.7}$$

  Where:

  - σ_n: Normal stress
  - τ : Tangential stress
  - c_1: Friction parameter
  - C_{MC}: Critical value

- **Tresca law**

  This law is a special case of the Mohr-Coulomb law, where $c_1 = 0$.

  $$\tau = C_{MC} \tag{2.8}$$

According to this Harzallah, a pertinent damage model needs to follow two criteria:

- It needs to be dependent on temperature and strain rate.
- It needs to be applicable for values of triaxiality η and Lode angle θ encountered during metal cutting processes.

These parameters are descriptors of the stress state in the material, and influence the fracture. The triaxiality is a function of the first invariant I_1:

$$\eta = \frac{\sigma_H}{\sigma_{eq}} = \frac{I_1}{3 \cdot \sigma_{eq}} \tag{2.9}$$

Lode angle, instead, depend on J_2 and J_3, the second and the third invariant of the stress deviator tensor.

$$cos(3\theta) = \frac{I_3}{2}\left(\frac{3}{I_2}\right)^{\frac{3}{2}} \tag{2.10}$$

Moreover, also the equivalent stress σ_{eq} can be calculated from J_2.

$$\sigma_{eq} = \sqrt{3J_2} \tag{2.11}$$

In his paper, Harzallah studied several fracture laws at different values of triaxiality and Lode angle, and concluded that both the Mohr-Coulomb law and the Tresca law are the ones that better describe the Ti6Al4V alloy's fracture behavior.

2.5.3 Contact/Friction Laws

The drilling process generates high friction forces and significant amounts of heat due to the interaction between the tool and the workpiece. These interactions also affect chip morphology. Tribology is defined as the study of friction, wear and lubrication, and design of bearings, science of interacting surfaces in relative motion [61].

Several laws can be found in the literature to model the phenomenon. A few examples, taken from Debard [16], are reported below.

- **Coulomb law**

  This is one of the most used laws to model the contact, but studies have shown that a more complex contact model is more suited to solve thermomechanical problems [16]. Generally, a constant friction coefficient is implemented.

  In the Lagrangian model developed by Abdelhafeez for a drilling process [2], the friction between the tool and the workpiece was modeled using this following law:

$$\begin{cases} \overline{\tau}_{fric} = \mu p, & if \quad \mu p \leq \overline{\tau}_{max} \quad (Sticking) \\ \overline{\tau}_{fric} = \overline{\tau}_{max}, & if \quad \mu p \geq \overline{\tau}_{max} \quad (Sliding) \end{cases} \tag{2.12}$$

  where

$$\overline{\tau}_{max} = \frac{A}{\sqrt{3}} \tag{2.13}$$

This relation can also be corrected by accounting for the effect of temperature. By substituting Equation 2.2 into the Von Mises criterion:

$$\sigma_{eq} = \sqrt{3} \cdot \tau_{max} \tag{2.14}$$

and considering this σ_{eq} at the onset of plasticity ($\varepsilon_p \approx 0,\ \dot{\varepsilon}_p = \dot{\varepsilon}_0$), the following equation is obtained:

$$\overline{\tau}_{max} = \frac{A'}{\sqrt{3}} = \frac{A}{\sqrt{3}}\left[1 - \left(\frac{T - T_0}{T_f - T_0}\right)^m\right] \tag{2.15}$$

- **Zorev's model**

  Another law with wide application in machining simulations is the Zorev's model. It considers two different interaction/contact behaviors on the rake face (*stick-slip phenomenon*):

  - *Sticking* area: sliding speed of the chip is very low compared to the tool. Shear stress is constant and equal to the limit flow stress of the material. This area is typically modeled with the Tresca's friction law:

    $$\vec{\tau} = -m_k \frac{\sigma_0}{\sqrt{3}} \frac{\vec{V}_g}{|\vec{V}_g|} \tag{2.16}$$

    Where $\vec{\tau}$ is the stress induced by friction, m_k is the Tresca's friction coefficient, σ_0 is the elastic strain limit of the material and V_g is the sliding speed.

  - *Sliding* area: zone where the chip easily flows on the tool rake face (low friction coefficient). If the friction coefficient is constant, the equation used is called Coulomb's friction law. However, models can be found in which nonlinear coefficients μ_{app} are employed. Among these is, for instance, Harzallah's modified Coulomb friction law [34].

    $$\vec{\tau} = -\mu_{app}(V_g) \frac{\sigma_0}{\sqrt{3}} \frac{\vec{V}_g}{|\vec{V}_g|} \tag{2.17}$$

    Where σ_n is the normal stress and the apparent friction coefficient μ_{app} is function dependent on V_g.

    So the stick-slip zone can be modeled with Tresca's friction law and the modified Coulomb's friction law:

    $$\begin{cases} \vec{\tau} = -m_k \frac{\sigma_0}{\sqrt{3}} \frac{\vec{V}_g}{|\vec{V}_g|}, & if \ \ \mu\sigma_n \leq m_k \frac{\sigma_0}{\sqrt{3}} \quad (Sticking) \\ \vec{\tau} = -\mu_{app}(V_g) \frac{\sigma_0}{\sqrt{3}} \frac{\vec{V}_g}{|\vec{V}_g|}, & if \ \ \mu\sigma_n \geq m_k \frac{\sigma_0}{\sqrt{3}} \quad (Sliding) \end{cases} \tag{2.18}$$

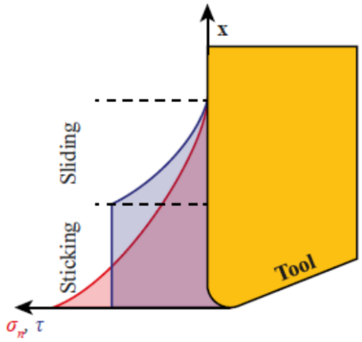

Figure 2.22: Modelization of the stick-slip contact from Zorev [19]

2.5.4 Temperature Laws

As previously mentioned, metal cutting processes generate heat, particularly at the tool cutting edge. The two main sources are the plastic deformation of the material during chip formation and the friction between the workpiece and the drill bit. This last phenomenon occurs at the rake face of the tool (tool-chip interface) and at the flank face of the tool (tool-generated surface interface). Tool's coating and lubricants are often used in production to reduce frictional forces, thus thermal effects. Another option is the use of coolants, to increase heat dissipation.

Several temperature laws have been developed to describe the physics of the problem. Some of the most notable ones, discussed in Debard's paper [16], are reported here.

- **Heat generation by plastic deformation**

  The heat generated by plastic deformation can be described as a volumetric heat power $\dot{q}_p$.

  $$\dot{q}_p = \beta_{TQ} \, \boldsymbol{\sigma} : \dot{\boldsymbol{\varepsilon}} \tag{2.19}$$

  The parameters that appear in the equation are:

  - β_{TQ}: Taylor-Quinney's coefficient. It's the portion of energy generated by plastic deformation converted into heat. The rest of it $(1 - \beta_{TQ})$ is the responsible for the plastic deformation of the material. It is directly related with the adiabatic heat fraction in ABAQUS.
  - $\boldsymbol{\sigma}$: stress tensor
  - $\dot{\boldsymbol{\varepsilon}}$: strain rate tensor

  It is common to consider the Taylor-Quinney's coefficient a constant. Debard observed that many authors showed that it is dependent on the plastic deformation, the strain rate and the deformation path. Bonnet [10] studies its dependence with the damage parameter D (Equations 2.20 and Figure 2.23).

$$\begin{cases} \beta_{TQ} = 0.625 & if \quad D < 0.8 \\ \beta_{TQ} = 1.87D - 0.88 & if \quad D > 0.8 \end{cases} \tag{2.20}$$

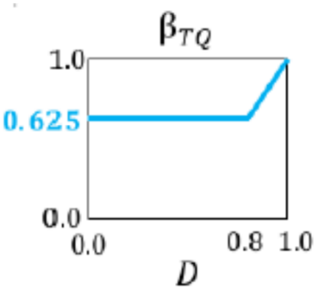

Figure 2.23: Taylor-Quinney's coefficient [10]

- **Heat generation by friction**

  It can be described as a surface heat power ($\dot{q}_f$). $\dot{q}_{fw}$ is the *surface heat power* seen by the workpiece, instead, and it' formulated as showed down here:

$$\dot{q}_{fw} = \beta_{fw} \cdot \eta_f \cdot \tau \cdot V_g \tag{2.21}$$

  where:

  - β_{fw}: the fraction of this dissipated heat that goes into the workpiece
  - η_f : fraction of the friction power ($\tau \cdot V_g$) that is dissipated as heat (typically 0.9 in the literature)
  - τ : friction stress
  - V_g: sliding speed

  β_{fw} is also called *thermal effusivity barycenter* of the materials in contact and is defined as:

$$\beta_{fw} = \frac{\zeta_w}{\zeta_w + \zeta_t} \tag{2.22}$$

  where ζ_i is the *thermal effusivity* of the material i, which, in turn, can be calculated as:

$$\zeta_i = \sqrt{\lambda_i \rho_i c_{pi}} \tag{2.23}$$

  where:

  - λ_i: thermal conductivity

  - ρ_i: density
  - c_{pi}: specific heat capacity

  The part of heat which goes into the tool β_{ft} can be calculated with:

$$\beta_{ft} = 1 - \beta_{fw} \tag{2.24}$$

- **Heat generation by convection**

  The heat dissipated by convection can be describe as a surface heat power $\dot{q}_{conv}$.

$$\dot{q}_{conv} = h_{fluid}(T_{surf} - T_{fluid}) \tag{2.25}$$

  where:

  - h_{fluid} is the convection coefficient of the fluid (air and lubricant).
  - T_{surf} and T_{fluid} are, respectively, the temperature of the surface in contact with the fluid and the temperature of the fluid.

- **Heat equation** Heat generated by friction and plastic deformation propagates in the workpiece during the cutting process through conduction.

$$\nabla \cdot (\lambda \nabla T) + P_{th,v} - \rho c_p \frac{\partial T}{\partial t} = 0 \tag{2.26}$$

  where:

  - λ is the thermal conductivity of the material
  - T is the temperature
  - $P_{th,v}$ is the volumetric heat power generated
  - ρ is the density
  - c_p is the specific heat capacity fo the material

2.6 Conclusions

Following the evaluation of the current state of the art on burr formation, it is evident that most existing models have been developed primarily to predict burr size, with the ultimate goal of minimizing it in order to reduce deburring costs or to mitigate the consequences of leaving burrs unremoved.

However, significant knowledge gaps remain regarding the effect of drilling burrs on the mechanical strength of components when they are not eliminated. In particular, there is a lack of models capable of predicting the post-burr formation condition of the material and assessing how burrs influence the structural performance of the assembly. This aspect is rarely addressed in the literature, as deburring is generally applied in most industrial contexts. Nevertheless, in applications involving One-Way-Assembly joints, it becomes essential to consider scenarios where burrs remain in place.

3 Analysis' Methodology

Once the most suitable set of equations to describe the problem is defined, the FEM model for simulating the axial drilling of a titanium plate can be established.

Figure 3.1 shows the complete life cycle of the specimen. The first stage corresponds to the manufacturing process, in which an initial drilling operation produces a hole with a diameter of 9.48 mm, followed by a reaming step that enlarges it to 9.52 mm. Two different levels of tool wear, creating different burrs, have been used to manufacture different specimens. Once the open-hole specimens are manufactured, they are divided into two series: one is heat-treated to relieve the residual stresses induced during manufacturing before being tested under fatigue, while the other is directly tested without any intermediate treatment.

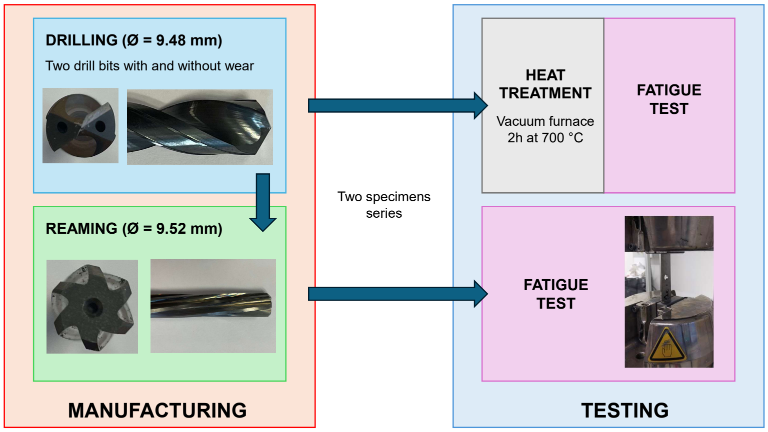

Figure 3.1: End-to-End specimen's life

The purpose of this study is to numerically reproduce the entire process, aiming to develop a reliable tool capable of predicting the material state after each step. To achieve this, several finite element models are created and validated by comparison with experimental results obtained in the laboratory.

Phase	**Model**	**Input**	**Result**
Drilling	Steady-State	Convergence analysis Sensitivity analysis	Force and Torque magnitude validation
	Full-Drilling	Parameters from Steady-State simulations	Force and Torque full signal validation
	Burr Formation	Parameters from Steady-State simulations	Validation by burr geometry, Material state after drilling
Reaming	Burr Formation	Material state after drilling	Validation by burr geometry, Material state after reaming
Fatigue Test	Fatigue Test	3D stress distribution	Fatigue life

Table 3.1: FE modelization

Table 3.1 summarizes the modeling framework. The drilling phase is divided into three simulations: Steady-State, Full-Drilling, and Burr Formation. These models are validated in terms of forces, torque, and burr geometry, in order to extract the material state at the end of the drilling process. The subsequent Reaming simulation, also validated against burr geometry, provides the material state after the complete manufacturing process. These simulations are then repeated using a worn drill bit to assess the influence of tool wear on the final outcome. Finally, the three-dimensional residual stress field is extracted and implemented in the last simulation (Fatigue Test), which reproduces the fatigue testing phase for both heat-treated and as-drilled specimens.

3.1 Steady-State simulation

This model is developed with the objective of validate the material laws, tool geometry and position, in order to guarantee that we are globally representative of the cutting process. As figure of interest we use force and torque. Specially important is the thrust force because it is the main driver of burr formation. Four drill-bit revolutions are simulated in order to check the positioning of the tool and to validate the model, while avoiding the significant computational cost of representing the entire drilling process.

For this model, the material in the center of the workpiece is removed according to the point angle and the chisel edge angle of the drill bit. The purpose of this simplification is to further reduce computational cost and to initialize the tool already "inside" the workpiece. However, since these cutting edges are not perfectly straight lines, a small transient phase still occurs before the tool becomes fully engaged with the workpiece.

Figure 3.2 shows the simulation assembly, including the tool and the workpiece.

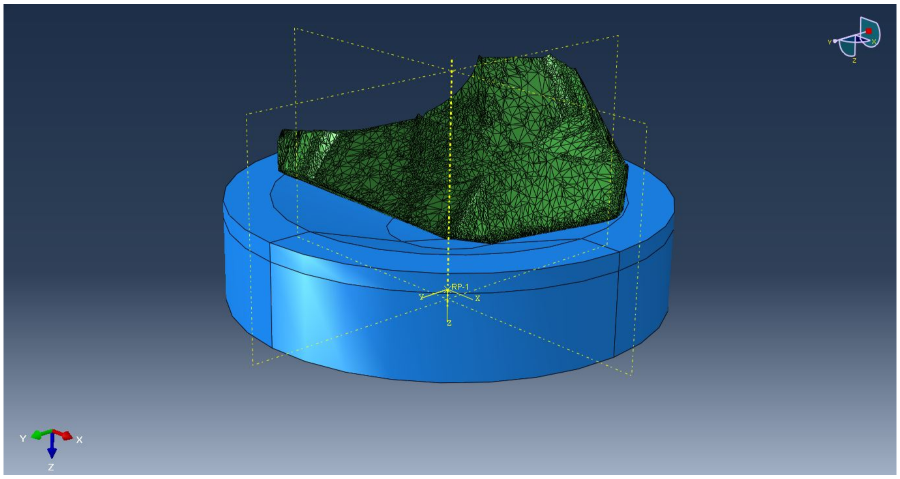

Figure 3.2: Steady-State simulation: Assembly

3.1.1 Part

The workpiece is a cylinder with a radius of 6 *mm* and a height of 2.8 *mm*. A countersink with a radius of 4.77 *mm* is created at its center. It features two different slopes: 10.75° for the inner section and 18.03° for the outer section. The thickness at the center of the workpiece is thus reduced to 1.48 *mm*.

Additionally, a partition following the profile of the upper surface is created, located at a depth of 0.5 *mm*.

Figure 3.3 shows a 3D view of the part and a sectional view of the cylinder.

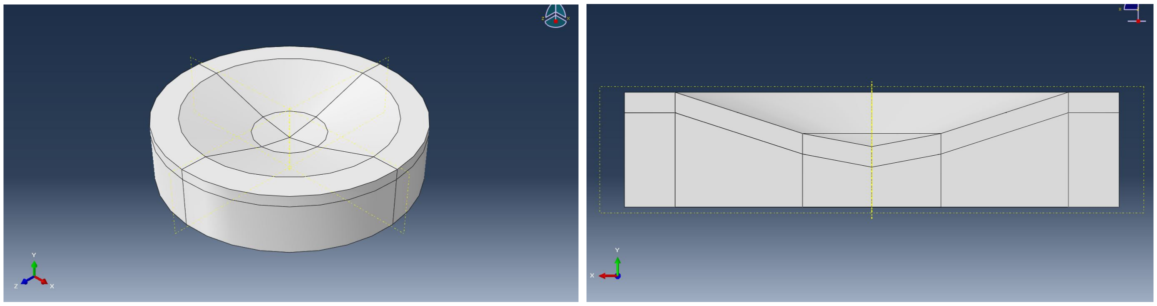

Figure 3.3: Steady-State simulation: Workpiece

3.1.2 Mesh

The mesh must be fine in the region where the drill bit indents, and the contact must be as uniform and continuous as possible.

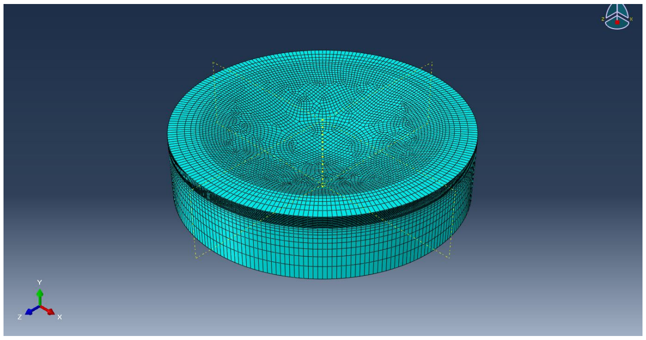

Figure 3.4: Steady-State simulation: Mesh

To ensure that the drill bit is indenting at every instant, the element height must be at most equal to the drill advancement per half revolution:

$$h_{max} = \frac{f}{2\omega} = \frac{46\ mm/min}{793\ rpm} = 0.029mm$$

A value of 0.025 *mm* is imposed for the elements of the upper partition.
In the indented area, a mesh with hexahedral elements is chosen, randomly distributed and as similar to each other as possible. The size of these elements is defined by seeding the entire part. The chosen value comes from a convergence analysis, which will be presented in a later stage.

To reduce the total number of elements, the lower partition contains 9 elements with a height bias of 8, while the outermost radial region of the workpiece uses a mesh seed with a bias from 0.15 *mm* to 0.35 *mm*.

The element type chosen is C3D8R: 8-node linear brick, reduced integration, default hourglass control. This type of elements is implemented in every simulation.

3.1.3 Boundary conditions

An encastre is imposed on the external walls of the workpiece. Moreover, also the temperature is a boundary condition of the model: an initial temperature of 500 °C is applied throughout the entire model.

3.2 Full-Drilling simulation

This model (Figure 3.5) simulates the entire drilling process, starting from the entry of the chisel edge into the plate and continuing until its exit.

As this is a particularly long and computationally expensive simulation, it is performed only after all model parameters have been studied and tuned in the Steady-State simulation.

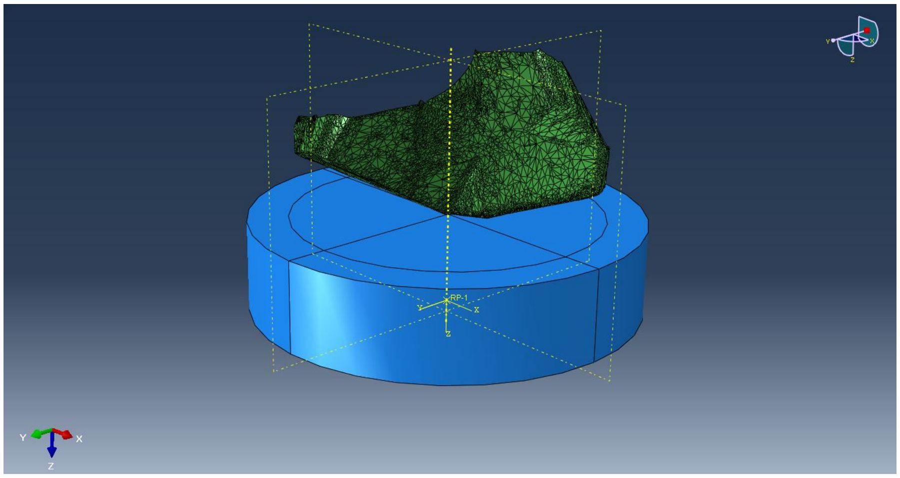

Figure 3.5: Full-Drilling simulation: Assembly

3.2.1 Part

In this case (Figure 3.6), the workpiece has the same dimensions as the one in the Steady-State simulation. However, the countersink and the partition are not present.

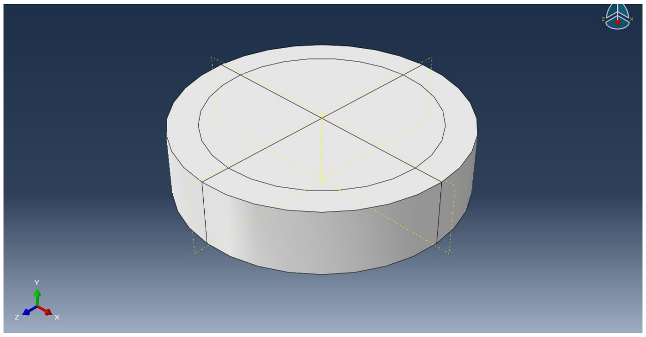

Figure 3.6: Full-Drilling simulation: Workpiece

3.2.2 Mesh

A mesh seed of 0.025 mm is applied in the axial direction, while a general mesh seed of 0.18 mm is imposed in order to avoid excessively increasing the computational cost of the simulation.

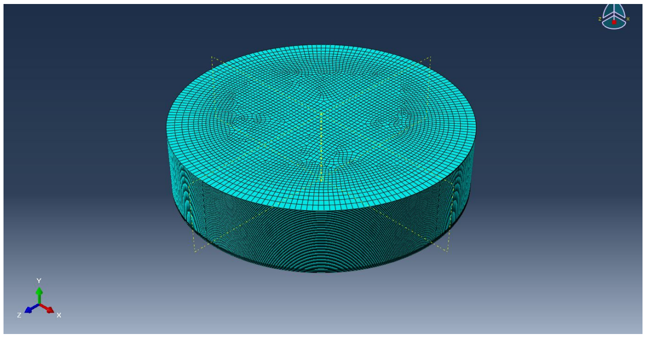

Figure 3.7: Full-Drilling simulation: Mesh

3.2.3 Boundary conditions

As for the Steady-State simulation, an encastre is imposed on the external walls of the workpiece. The same goes for the temperature: an initial temperature of 500 °C is applied throughout the entire model.

3.3 One-Way-Assembly simulation

This final model is created to simulate the drilling process of two stacked plates. In manufacturing processes, the plates to be joined are typically stacked first and then drilled, ensuring coaxial holes and significantly reducing manufacturing time. The objective of this model is to represent how the addition of material beneath the top plate affects the generated forces and the final burr geometry.

As in the previous simulations, two cylinders are created to represent the portion of the panels to be drilled. The upper cylinder is countersunk to accommodate the drill bit during the final phases of machining the first plate and to significantly reduce computational time. Two 3D shell surfaces are also added to the model to represent the remainder of the panels. This addition is necessary to study the differential bending of the plates.

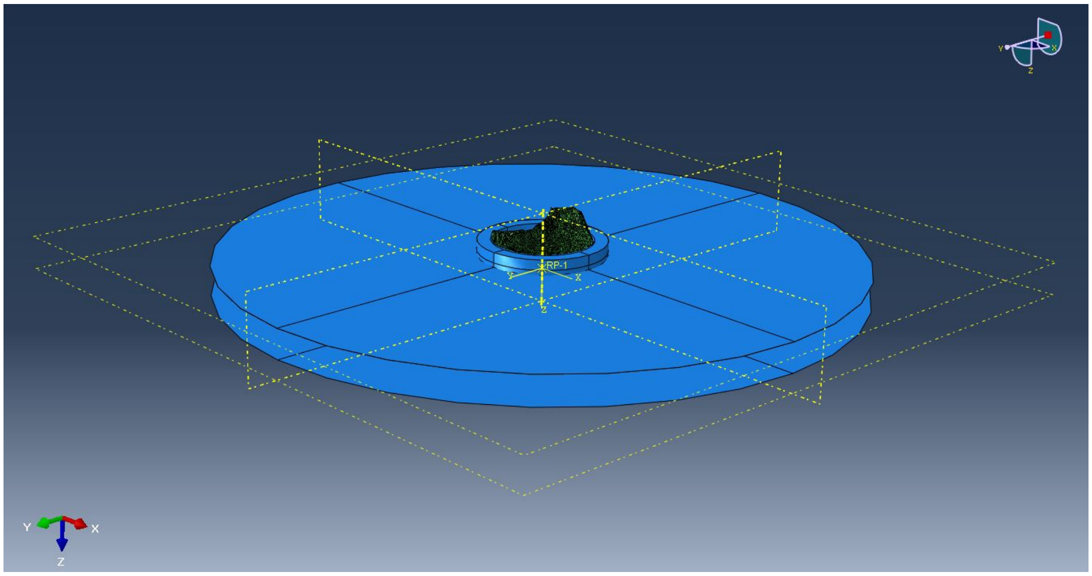

Figure 3.8: One-Way-Assembly simulation: Assembly

3.3.1 Part

The OWA model is composed of three parts:

- First part – A cylinder similar to that used in the Steady-State simulation, with identical dimensions. However, the countersink is lowered by 0.98 *mm* to simulate the process from a more advanced stage;
- Second part – Identical to the one used in the Full-Drilling simulation. A partition is added at a depth of 1.3 *mm*;
- Third part – Modeled as a 3D shell-type part. It has an outer radius of 30 *mm* and an inner radius of 6 *mm*. The plate thickness is set to 2.8 *mm*.

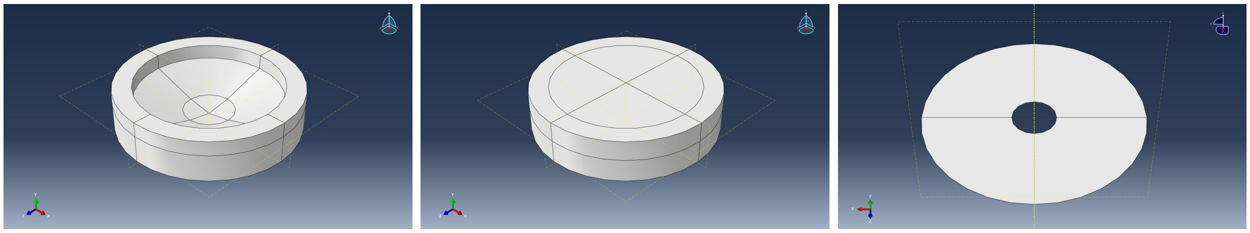

Figure 3.9: One-Way-Assembly simulation: Workpiece

3.3.2 Mesh

The three parts are meshed as follows:

- Upper panel – The mesh is similar to that used in the Steady-State simulation. However, the partition from that simulation is not present. The indented zone has a mesh seed of 0.025 *mm* in height, while the upper part uses a mesh seed growing from 0.05 *mm* to 0.35 *mm*. The general mesh seed is 0.18 *mm*;
- Lower panel – Partitioned into two regions: the upper region has a mesh seed of 0.025 *mm*, while the lower region contains 7 elements with a bias of 8. Again, the general mesh seed is 0.18 *mm*;
- 2D panel – The general mesh seed is 2 *mm*. The element type is S4R: a 4-node doubly curved thin or thick shell, with reduced integration, hourglass control, and finite membrane strains.

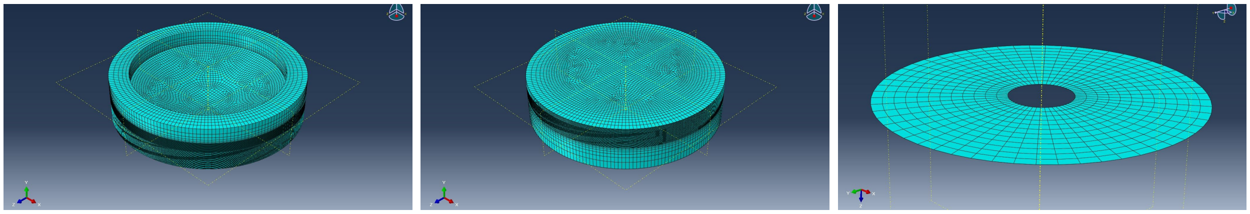

Figure 3.10: One-Way-Assembly simulation: Mesh

3.3.3 Boundary conditions

An encastre is imposed on the external radius of the shell parts and an initial temperature of 500 °C is applied throughout the entire model.

Furthermore, a Shell-to-Solid coupling is defined between the 2D parts and their corresponding 3D workpieces.

3.4 Burr Formation simulation

The model was validated through the Steady-State and Full-Drilling simulations in terms of force and torque. The Burr Formation simulation is now performed to extract the final material state after hole machining and the resulting residual stress distribution. This simulation is validated in terms of burr geometry. To achieve this, very fine meshes are required to accurately capture the formation mechanics, which was not feasible in the Full-Drilling simulation due to the prohibitive computational cost. Moreover, a refined mesh allows for a more detailed extraction of the residual stress profile at the hole's walls.

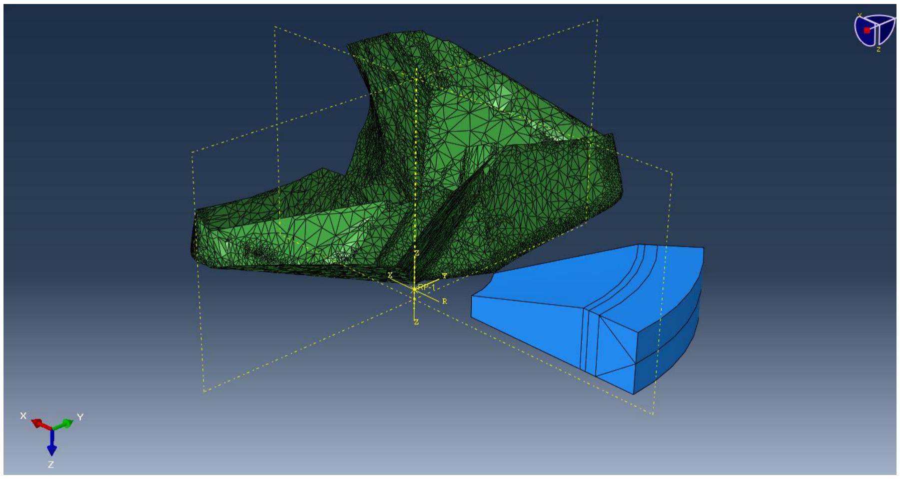

Figure 3.11: Burr Formation simulation: Assembly

To meet these requirements, a 40° circular sector (one-ninth of the full model) is isolated. This sector includes a countersink similar to that of the steady-state simulation, but the central region in contact with the chisel edge is removed and the height is reduced, in order to minimize the total number of elements. Figure 3.11 shows the setup of this model.

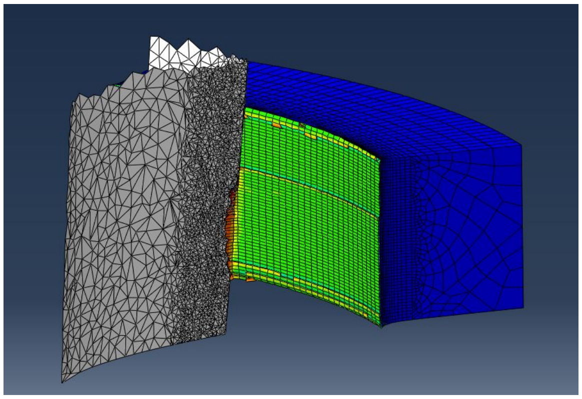

Figure 3.12: Burr Formation simulation: Reaming step

However, drilling with a twist drill is not the only step in the hole-making process. A second operation is performed using a reamer, designed to circularize the hole and remove any geometric defects. The final hole radius increases by approximately 2 *mm*. It is therefore important to assess the condition of the hole after this operation and to study the differences between the two processes.

3.4.1 Part

Figure 3.13 shows the workpiece used. It consists of a 40° circular sector taken from the workpiece of the steady-state simulation. The outer radius of the part is 6 *mm*, while the inner radius is 1.68 *mm*. The slope is again 18.03°. In addition, three partitions are created at radii of 4.65 *mm*, 4.81 *mm*, and 5.05 *mm*, respectively. Finally, a triangular partition is created in the outermost radial section.

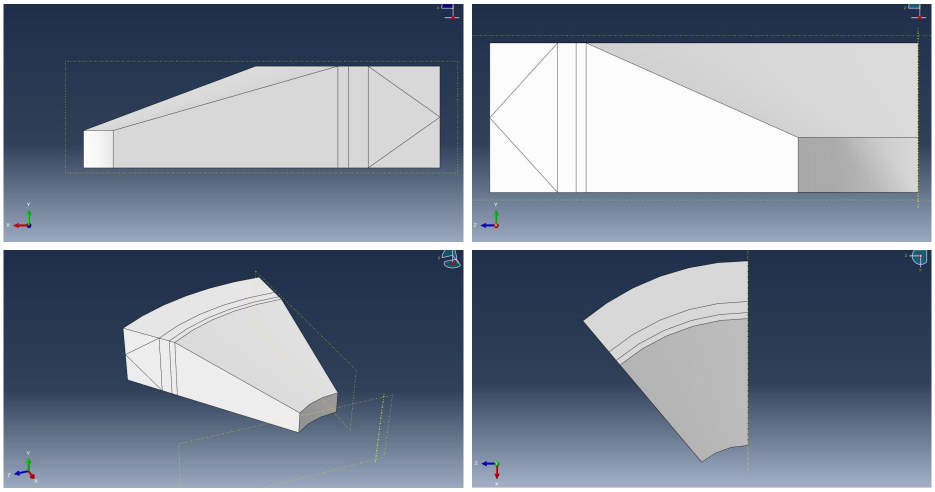

Figure 3.13: Burr Formation simulation: Workpiece

3.4.2 Mesh

In this model, the area of interest is the region near the hole walls. Therefore, the mesh seed is refined in the zones where the drill bit margins and the reamer will indent. Observing Figure 3.14 from left to right in the radial direction: in the outermost partition, a mesh seed from 0.25 *mm* to 0.06 *mm* is defined, followed by one from 0.05 *mm* to 0.012 *mm*, then 0.01 *mm* in the area of greatest interest, and finally 81 elements with a bias of 9 in the region where the main lips indent.

The mesh is divided into two regions: the zone in contact with the tools uses a structured mesh control with hexahedral elements. In the outer region, a sweep mesh with hexahedral elements is chosen to reduce the total number of elements. A triangular partition is created to facilitate the transition from small to larger elements.

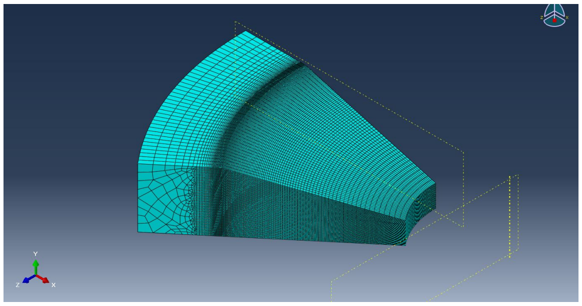

Figure 3.14: Burr Formation simulation: Mesh

3.4.3 Boundary conditions

An encastre is imposed on the external walls of the workpiece, while the outer radial band is bounded in the azimuthal direction. The initial temperature is imposed equal to 500 °C in the whole model.

3.5 Thermal Stresses simulation

A dedicated simulation was performed to obtain a first approximation of the thermal stresses generated during the drilling process. To achieve this, an initial temperature profile is imposed, and the workpiece is allowed to cool down for 5 seconds, until it reaches room temperature.

3.5.1 Part

The thermal model consists of an axisymmetric rectangular workpiece of 5.21 $mm \times 2.8$ mm. Two partitions are created, starting from the left: one at 0.25 mm and one at 1.21 mm.

3.5.2 Mesh

Elements with a height of 0.025 mm are created through the thickness of the workpiece, and the same dimension is imposed in the first partition. In the following partition, a biased mesh seed is defined, ranging from 0.025 mm to 0.1 mm, while in the last partition the bias ranges from 0.1 mm to 0.5 mm. At the rightmost end, six elements are defined through the thickness.

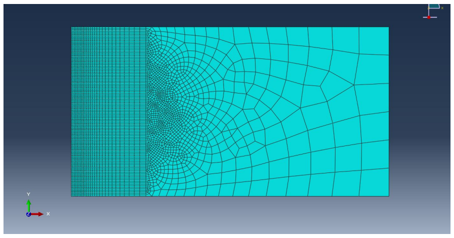

Figure 3.15: Thermal Stresses simulation: Mesh

3.5.3 Boundary and initial conditions

An encastre is imposed in the right edge of the workpiece. In the same edge, a temperature of 25°C acts as a boundary condition.

An initial parabolic temperature distribution, similar to that observed by Debard [17] near the cutting region, was imposed on the workpiece (Figure 3.16). Four temperature are considered at the hole's walls: 200°C, 300°C, 400°C and 500°C and simulations are performed considering the 4 distributions.

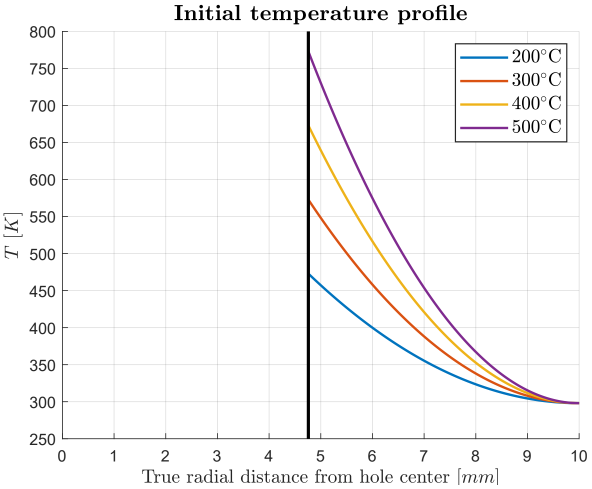

Figure 3.16: Thermal Stresses study: Temperature profile

3.6 Fatigue Test simulation

The previous steps served to validate the model and obtain the post-drilling material state. The objective of the present simulation is to draw conclusions regarding the fatigue life of the specimen. Two configurations are investigated, with and without residual stresses, in order to reproduce the experimental conditions of heat-treated and non-heat-treated specimens.

An implicit simulation is performed to reproduce a single loading cycle. First, a stress relaxation step is applied to allow the stresses to redistribute and reach equilibrium. Then, a tensile load is applied, with the minimum load level corresponding to 10% of the maximum load.

Fatigue life is evaluated using the Dang Van fatigue criterion [3], which allows predicting the fatigue crack initiation in metallic materials from the full load history while accounting for multiaxial stress conditions. This approach is particularly suitable for variable or non-proportional loading conditions, as in fatigue tests. The parameters used in the model were calibrated based on values found in the literature [9].

3.6.1 Part

Fatigue tests are carried out on specimens conforming to standard EN 6072, with dimensions of 146 $mm \times 26$ mm and a thickness of 2.8 mm (Figure 3.17).

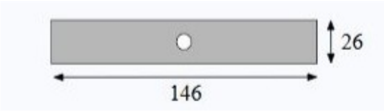

Figure 3.17: Specimen (EN 6072)

To simulate the test, only one quarter of the specimen was modeled. The hole has a diameter of 9.58 mm, corresponding to the final diameter obtained in the reaming simulation.

A horizontal partition was created 13 mm from the hole center to reduce the number of elements. Additional partitions were defined near the hole, similarly to the Burr Formation simulation: three circular partitions with radii of 4.81 mm, 5.05 mm, and 6 mm, respectively, and a triangular partition in the outer region to enable a smooth transition from smaller to larger elements. The resulting geometry is shown in Figure 3.18.

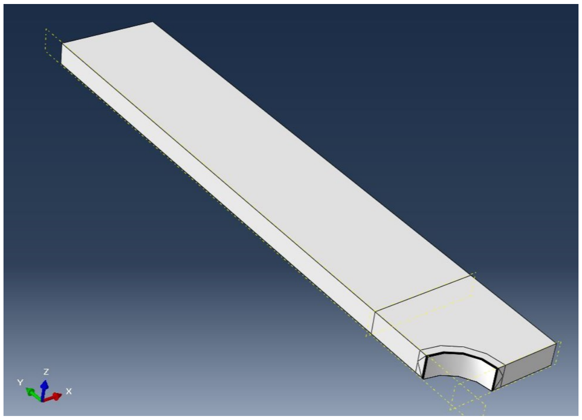

Figure 3.18: Fatigue Test simulation: Workpiece

3.6.2 Mesh

Far from the hole, a mesh seed of 2 mm was applied in the plane, with eight elements through the thickness.

The mesh around the hole closely reproduces that obtained at the end of the Burr Formation simulation, enabling straightforward mapping of the stress distribution into the model. In the innermost region, the elements have a radial size of 0.01 mm. The second partition features a radially biased mesh seed from 0.012 mm to 0.05 mm, while the third ranges from 0.06 mm to 0.25 mm. Finally, to connect the hole region to the rest of the mesh, another biased mesh seed from 0.25 mm to 2 mm was created. A sweep mesh was used in this region to ensure a smooth element transition. Along the z-direction, the element height is 0.1 mm.

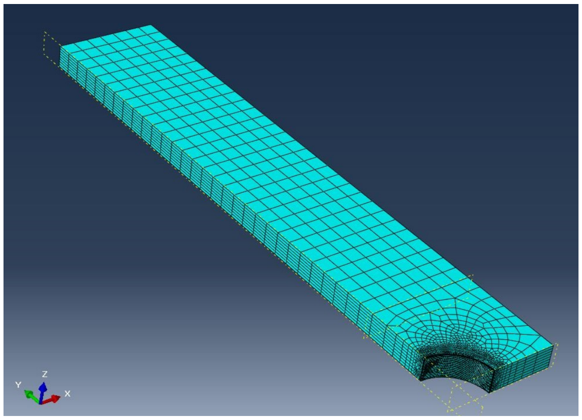

Figure 3.19: Fatigue Test simulation: Mesh

3.6.3 Boundary conditions and Loads

Two symmetry boundary conditions are applied to the inner surfaces of the specimen to reproduce the full geometry.

A uniaxial tensile load is applied on the upper surface in the y-direction. Different load levels are tested to reconstruct the fatigue curves.

3.6.4 Subroutine SIGINI

ABAQUS allows the use of Fortran subroutines to initialize the stress state in the model. Starting from the 3D stress state extracted from the Burr Formation simulation, expressed in cylindrical coordinates, the stresses are transformed into global coordinates and assigned to the integration points of the elements. It is crucial to reproduce the mesh of the Burr Formation simulation, particularly in the radial direction, to correctly assign the stresses as extracted and accurately reproduce their profile. The inserted stresses vary along the radial direction but maintain the same profile along the z-axis.

3.7 Tools

Three different tools are used in the simulation: a new drill bit, with the nominal dimensions declared by the manufacturer; a worn drill bit, following its use in previous drilling operations; and finally, a reamer lip.

The CAD models of the tools can be found on the manufacturer's website. However, these models often do not accurately represent the real tool geometry. Therefore, the drill bit is scanned in order to capture its complex features. The same modeling procedure is followed for all three tools.

Using the Alicona 3D scanner, the selected tool is first scanned. From the scan, an STL file is generated, containing a very dense triangular mesh of the tool, with millions of elements.

Since such a mesh is too heavy and problematic for FEM simulations, an additional software tool, Blender, is used to simplify the file. In particular, the "Modeling" tab is the most useful for working on the mesh. First, loose elements are removed using the dedicated function, while unnecessary parts of the mesh are manually deleted. Then, using the "Decimate Geometry" function, the number of elements in the mesh is reduced by a chosen percentage. This function is ideal for the task, as it decreases the file size without significantly altering the macro-geometry of the tool. Finally, the "Merge > By Distance" function is applied to reduce the number of elements in the less critical regions of the tool, such as the rake face, while missing elements are manually created to fill any gaps in the mesh.
The final mesh is then ready to be used in ABAQUS/CAE. The "Import" tab allows the STL file to be converted into an INP file, ready to be used in the models.
This meshes contain between 10,000 and 20,000 triangular elements. The part is defined as Discrete Rigid.

Figure 3.20 shows different views of the new drill bit.

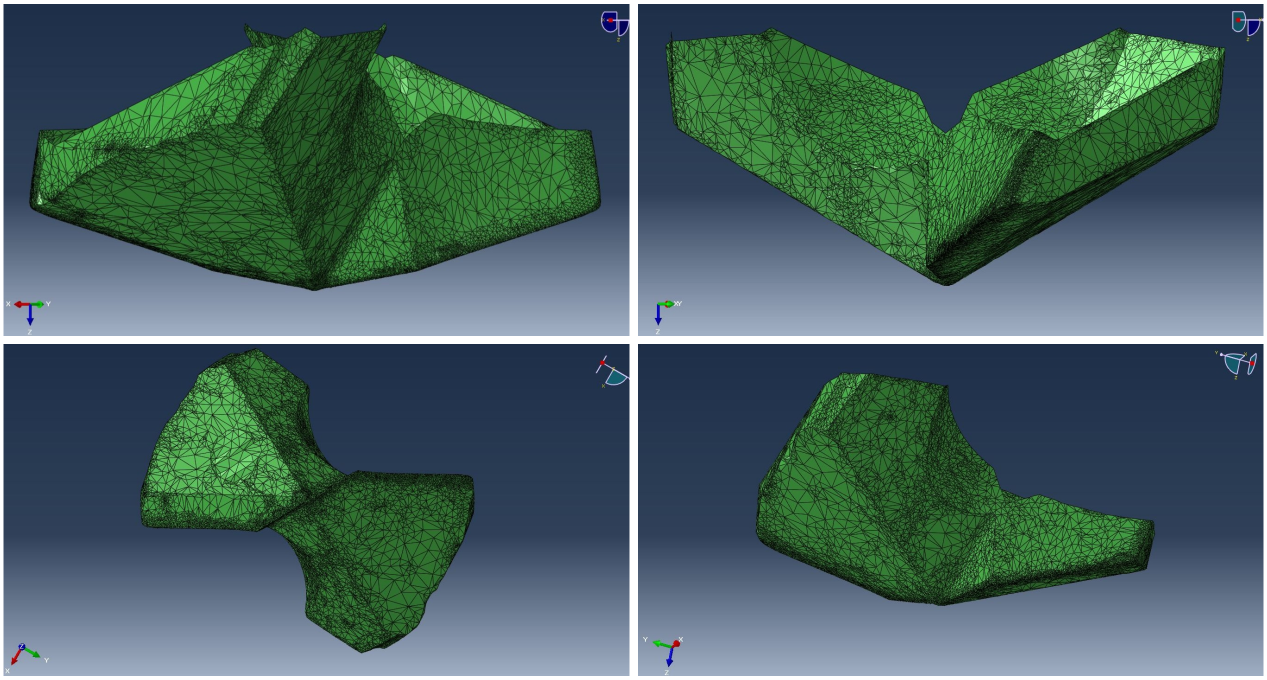

Figure 3.20: New Drill Bit CAD

By observing Figure 3.21, and in particular the top-left view, the defect of the worn tool near the drill bit margins can be clearly seen.

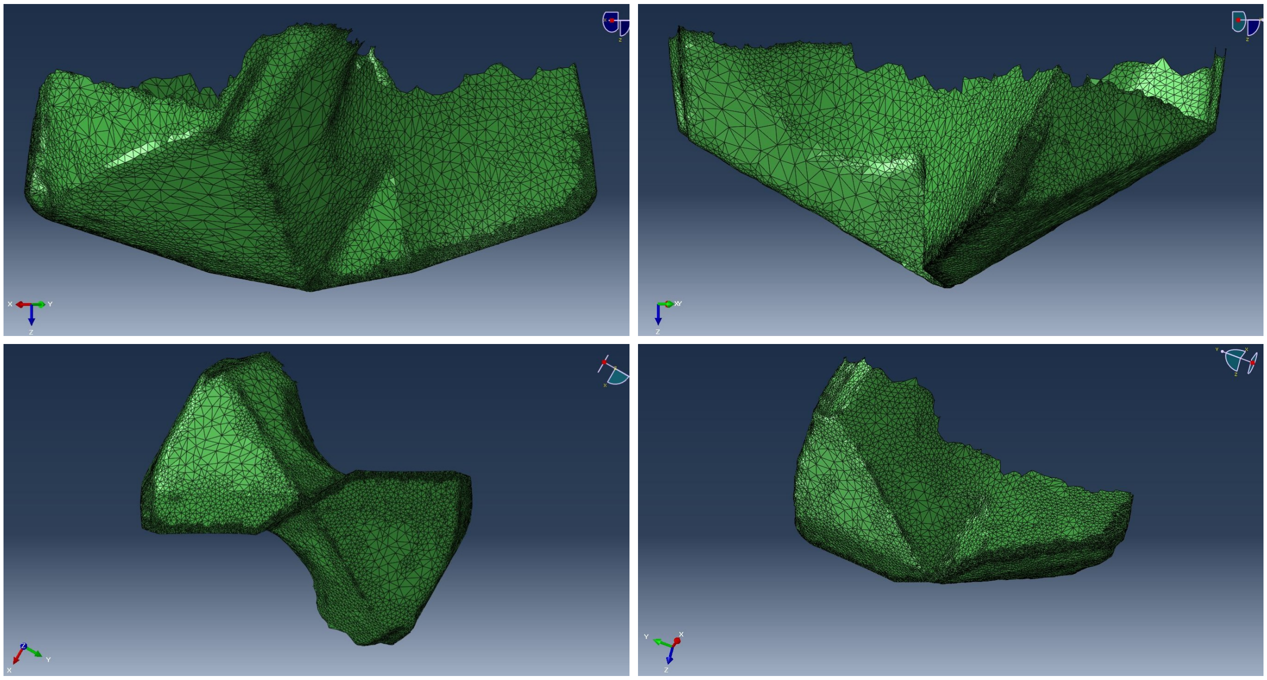

Figure 3.21: Worn Drill Bit CAD

Only one lip of the reamer is modeled, as it is the only part of the tool in contact with the hole walls and this choice significantly reduces the number of elements (Figure 3.22).

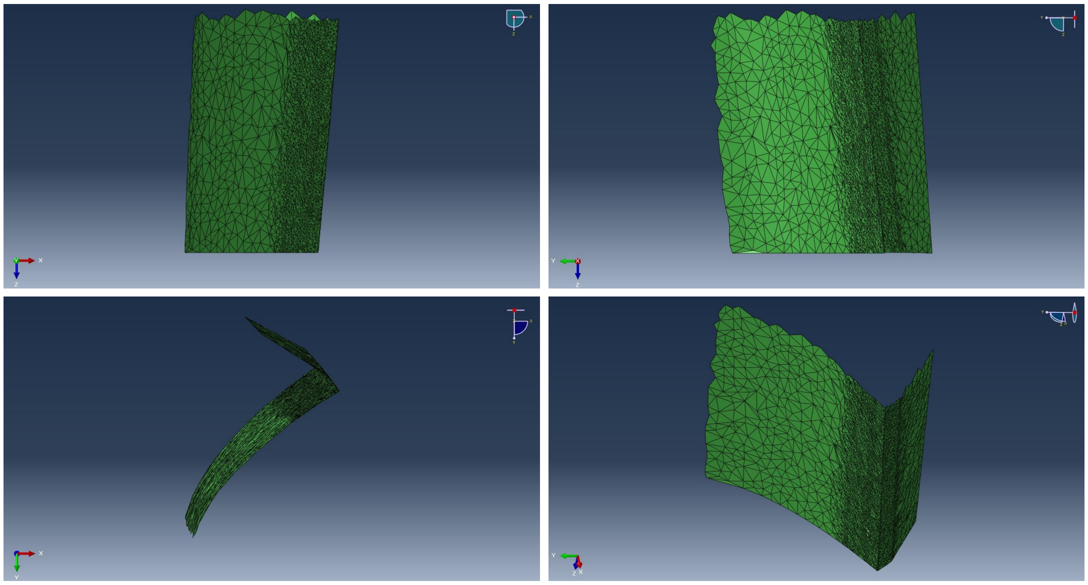

Figure 3.22: Reamer CAD

3.7.1 Boundary conditions

The tools are considered as rigid bodies, and their motion is constrained to that of their reference point.
Two parameters describe the tool's motion: feed and rotational speed. They are imposed as boundary conditions for the tools movement.

Regarding the drilling process:

- Feed: $f = 46\ mm/min = 0.7665\ mm/s$
- Rotational speed: $\omega = 793\ rpm = 83.004\ rad/s$

while during reaming:

- Feed: $f = 134\ mm/min = 2.233\ mm/s$
- Rotational speed: $\omega = 670\ rpm = 70.162\ rad/s$

3.8 Model setup

In this section, the needed inputs to create an ABAQUS/CAE simulation are described.

3.8.1 Material definition

The material properties used in the model are derived from static tests performed in the laboratory on Ti6Al4V specimens. These tests were used to characterize the Young's modulus E, the Poisson's ratio ν, and the plasticization (hardening) curve.

Density [kg/m^3]	4430
Young's Module [MPa]	109500
Poisson's Ratio [kg/m^3]	0.34
Melting Temperature [K]	1877

Table 3.2: Material properties for Ti6Al4V

The material behavior is described using the Johnson–Cook plasticity law, selected for its simplicity, ease of calibration, and the wide availability of experimental data in the literature. This law has also been extensively employed in previous modeling efforts, consistently yielding reliable results. Table 3.3 reports the measured parameters used to represent the Johnson–Cook plasticity model. The reference strain rate is initially set to 1, although its actual value will be discussed in the following sections.

Damage initiation is defined according to Equation 2.6, while damage evolution is modeled through an exponential energy criterion, chosen for its robustness and reduced sensitivity to mesh refinement. Damage modeling is often complex to describe and evaluate; therefore, the

A [MPa]	**B** [MPa]	**n**	**C**	**m**	**T**$_r$ [K]	**T**$_m$ [K]
927	565	0.46	0.035	1	298	1877

Table 3.3: Johnson-Cook plasticity model parameters for Ti6Al4V

values used for the Johnson–Cook damage model are taken from the literature. Specifically, reference is made to Abdelhafeez's paper [2], where the following parameters were used in a CEL-type FE drilling simulation.

d_1	d_2	d_3	d_4	d_5
-0.09	0.25	0.5	0.014	3.87

Table 3.4: Johnson-Cook damage model parameters for Ti6Al4V

The damage criterion is modeled using an energy-based approach, expressed in terms of the damage evolution parameter D. It is based on the fracture energy G_f with exponential softening, as shown in the following equation.

$$D = 1 - exp\left(- \int_0^{u_p} \frac{\tilde{\sigma}}{G_f} \right) du_p \tag{3.1}$$

Again referring to the same source, the fracture energy is evaluated using the following formula:

$$G_f = K_{IC}^2 \frac{1 - \nu}{E} \tag{3.2}$$

where K_{IC} is the fracture toughness of the material, reported as 60 $MPa\sqrt{m}$ in the paper. This leads to a calculated value of $G_f = 27.93\ mJ/mm^2$.

As mentioned in the previous section, since the tools are modeled as rigid bodies, no material is assigned to them.

3.8.2 Physical approach

In all models, the influence of temperature on the material behavior is not considered. Therefore, the thermo-mechanically coupled problem is not solved, but rather a purely dynamic one. Temperature is included in the simulation only as a parameter in the Johnson–Cook laws, but it is not treated as a degree of freedom of the elements.

Nonetheless, neglecting the thermal effect might be an excessive simplification of the problem. At a later stage, a simple thermal model will be introduced to obtain an initial estimate of the contribution given by temperature. For these simulations, the following values are considered, which are again taken from Abdelhafeez's paper [2], plus the coefficient of thermal expansion taken from [62].

Conductivity [W/mK]	6.7
Specific Heat [J/kgK]	526.3
Inelastic Heat Fraction	0.9
Expansion Coefficient [$\mu m/(m°C)$]	$3 \cdot 10^{-9}T + 7 \cdot 10^{-6}$

Table 3.5: Thermal properties for Ti6Al4V

3.8.3 Contact

The contact defined between the parts is specified as a General Contact (Explicit). This allows modeling the interaction between the tool and the workpiece. To define it, two surfaces are required:

- Tool surface – element-based, containing all the elements of the tool;
- Workpiece surface – node-based, defined over the entire workpiece. Its definition is not implemented directly in ABAQUS/CAE, but is possible only by modifying the INP file.

An additional General Contact is applied between the two cylinders in the OWA simulation. All possible surfaces of the elements from both meshes are selected, and contact is imposed between them.

The chosen contact properties are:

- Normal behavior: with "Hard" contact and the Lagrange multiplier method for constraint enforcement. This is set to model how the pair of surfaces interact perpendicularly. Hard contact avoids that surfaces penetrate each other.
- Tangential behavior: Coulomb's model that was presented in the previous chapter is used to model the friction between the tool and the material. Initially, the friction coefficient is set to 0.4, but following a sensitivity analysis, the final value is chosen as 0.6. This choice is justified in the next chapter. The maximum shear stress is derived from formula 2.15:

$$\overline{\tau}_{max} = \frac{A'}{\sqrt{3}} = \frac{927}{\sqrt{3}}\left[1 - \left(\frac{773-298}{1877-298}\right)^{0.46}\right] = 374.2\ MPa$$

3.9 Computational cost reduction techniques

The choice of explicit schemes for the simulation is dictated by the need to reduce the computational time required to obtain results. Due to the large nonlinearities that arise in machining processes, implicit methods are more complex and often struggle to converge. However, this choice has a drawback: the problem becomes conditionally stable, i.e., dependent on the chosen integration time step.

The stability condition for an explicit simulation is given by

$$\Delta t \leq \Delta t_{stable} = \frac{L_e}{C_e} \tag{3.3}$$

where L_e is the characteristic size of the element and C_e is the highest characteristic wave speed of the material. This condition therefore requires using integration time steps smaller than the minimum Δt_{stable}, otherwise the simulation will not converge. This also means that the smaller Δt_{stable}, the longer the simulation time. Considering the need for fine meshes to accurately capture the physical behavior of the problem, L_e is often very small. Therefore, solutions that allow faster simulations become necessary.

It should be noted that the material wave speed C_e is defined as

$$C_e = \sqrt{\frac{E}{\rho}} \tag{3.4}$$

and, consequently, substituting into the equation above, the relationship

$$\Delta t_{stable} = L_e\sqrt{\frac{\rho}{E}} \tag{3.5}$$

is obtained. It is evident that Δt_{stable} depends on the material density.

Mass scaling refers to scaling the mass of the problem to increase the minimum required integration time step. ABAQUS provides several methods to apply mass scaling. Mass scaling can also be applied selectively to specific parts of the model, such as regions where some elements do not require the minimum time increment.

- Fixed mass scaling: it scales the original nodal mass matrix at the beginning of the step at which it is specified (unless a variable mass scaling is applied as well), which makes it computationally efficient. Two different approaches can be used, in turn, to apply a fixed mass scaling:
    - Mass scaling factor definition: this is the factor by which the density will be multiplied. Thus, Δt_{stable} will be increased by the square root of this factor (see Equation 3.5).
    - Desired minimum stable time increment definition: the required scaling factor by which the density is multiplied is computed so that the minimum stable time increment matches the imposed value.
- Variable mass scaling: the mass of the elements is periodically scaled during a step. It can be applied alongside fixed mass scaling. For this type of mass scaling, the specification need to be a desired minimum stable time increment, and the scaling factor will be automatically computed and applied, as required, throughout the step.
  This type of mass scaling is useful when the stable time increment changes drastically during a step. For example, when elements are highly compressed or crushed, as happens in machining operations like drilling.

The parameter that linearly multiplies the minimum integration time step is called the *Mass Scaling Factor* (MS).

$$\Delta t_{stable}^{simulation} = MS \cdot \Delta t_{stable}^{real} = L_e \sqrt{\frac{MS^2 \rho}{E}} \tag{3.6}$$

Another commonly used method in this type of analysis is *time/load scaling.* This technique consists of accelerating the operational conditions of the process. The loading rate is scaled by a parameter called the *Time Scaling Factor* (TS). Accelerating the simulation reduces the simulation time and therefore the computational cost.

$$V_{simulation} = TS \cdot V_{real} \iff TS = \frac{t_{total}^{simulation}}{t_{total}^{real}} \tag{3.7}$$

These methods are very useful for achieving faster simulations but must be applied carefully. Increasing the density of a material leads to a linear increase in kinetic energy. The dynamic effects of the problem may then dominate the simulation, producing invalid results. Similarly, increasing the load rate introduces large artificial inertial forces, which also increase kinetic energy, quadratically proportional to the velocity.

In explicit solutions, it is therefore important to monitor the kinetic energy as an indicator of the simulation's quality. Its contribution must remain negligible to treat the problem as quasi-static. This limit is often set at 5% of the simulation's internal energy.

Additionally, it is particularly important to be cautious when accelerating the simulation if strain rates are considered in the material behavior. As demonstrated in Vazquez del Rey Perdomo's report [19], it has to be scaled with the TS factor used in the simulation.

3.9.1 Mass scaling

The mass scaling is set as a variable one that is applied every 1 time increments on those elements whose stable time increment is under the specified one.
The mentioned target time increment is initially set to $5 \cdot 10^{-8}$ for the steady-state simulation. Subsequently, the effect of this value on the simulation is studied. Table 3.6 reports the results for force, torque, and the ratio between kinetic and internal energy (K/I).

MS	**Force [N]**	**Torque [Nmm]**	**K/I [/]**
$2.5 \cdot 10^{-8}$	270.58	1085	0.60
$5 \cdot 10^{-8}$	280.25	1149	0.75
$1 \cdot 10^{-7}$	291.42	1212	1.07
$5 \cdot 10^{-7}$	273.72	1324	7.98

Table 3.6: Mass scaling sensitivity analysis

The upper limit for Δt_{stable} is $5 \cdot 10^{-7}$, as the energy ratio exceeds the imposed limit. The effect of mass scaling is essentially negligible in the range $2.5 \cdot 10^{-8} \div 1 \cdot 10^{-7} (\sim 5\%)$. Therefore,

$\Delta t_{stable} = 5 \cdot 10^{-8}$ confirmed for the steady-state simulation, corresponding to a mass scaling factor (MS) of 25. For the other, much longer simulations, $\Delta t_{stable} = 1 \cdot 10^{-7}$is employed. For the burr formation simulation, where elements are smaller, the MS is set to 100.

3.9.2 Time scaling

Regarding time scaling, the simulations are accelerated compared to the original machining conditions.
Again the effects of the speed up are studied. Table 3.7 shows force, torque and K/I trends.

TS	**Force** $[\boldsymbol{N}]$	**Torque** $[\boldsymbol{Nmm}]$	**K/I** [/]
2	350.34	1098	0.48
5	377.30	1173	0.63
10	383.78	1249	0.93
20	373.95	1247	1.77

Table 3.7: Time scaling sensitivity analysis

The reference value for the time scaling factor (TS) is 5. Reducing the TS factor leads to a 6–7% decrease in both force and torque. Increasing this value, instead, has a negligible effect on the force but causes a significant increase in torque.

Therefore, TS = 5 is chosen for the Steady-State simulation, while TS = 20 is applied for the other, considerably more computationally expensive simulations. The machining conditions are thus:

- $V_{3,ss} = 3.8325\ mm/s$
- $\omega = 415.02\ rad/s$

and

- $V_{3,fd} = 15.33\ mm/s$
- $\omega = 1660.08\ rad/s$

In consequence, the reference strain rate is set as 5 and 20, respectively.

4 Drilling Simulation results

In this chapter, the results obtained from the simulations are showed. A comparison will be performed with an experimental benchmark, obtained by coupon testing.

4.1 Experimental results

The first phase of the study consisted of collecting experimental data obtained from specimen testing. The objective was to expand the available drilling database and serve as a validation point for the FE models that had been developed.

The experimental tests were carried out on specimens with different burr heights. To produce the holes, an initial drilling phase was performed, followed by a reaming phase. The first drilling step was conducted using a Tivoly drill bit, a twist drill with two cutting lips. Initially a hole with a diameter of 9.48 *mm* is produced. Subsequently, a Mapal reamer was employed to obtain the final diameter of 9.52 *mm*.

To control burr formation, different drill bits were used. Debard [17] demonstrates how the presence of tool wear affects the final burr size. For this reason, a defect was artificially introduced on the drill bit by *sanding* its corners. Apart from this variation, the remainder of the drill geometry was equivalent to that of a new tool. The drills were labeled according to the expected burr height generated by the process: new for the unmodified tool, worn for the drill bit that generates burr of 0.4 *mm*.

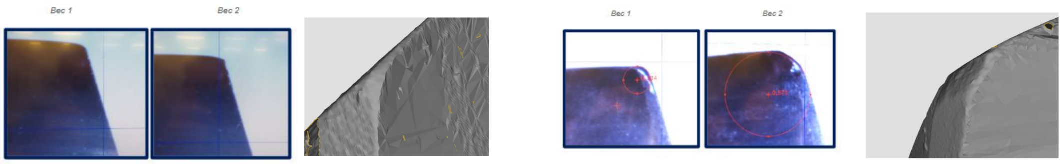

(a) New drill bit

(b) Worn drill bit

Figure 4.1: Drill bits comparison

Figure 4.1 reports the details of the corner wear for the new tool and the one that generates 0.4 *mm* burrs. A significant wear is present on the corners, with a radius of about 0.25 *mm*.

4.1.1 Thrust force and torque

A Kistler load cell was mounted at the center of the drilling setup and used to acquire force and torque data for each specimen. The measurements were recorded at a sampling frequency of 10,000 *Hz*. The resulting signals exhibit noise across all channels, particularly for torque values. Consequently, a low-pass *Butterworth* filter (order $n = 4$, cutoff frequency $f_{crit} = \omega/2 = 6.7\ Hz$) was applied to the data. Results are shown in Figure 4.2.

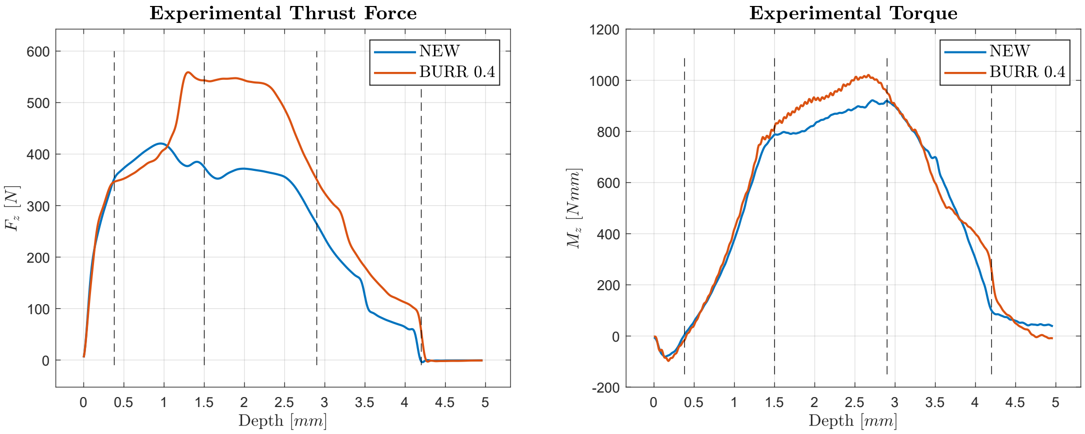

Figure 4.2: Experimental results: Thrust Force and Torque for the different drill bits

The results of the different specimens are subsequently collected, and an average is computed across the datasets. By observing the resulting curves, four key instants can be identified, each representing a distinct stage of process progression. Reference is made to Figure 4.3, which schematically illustrates the position of the tool relative to the workpiece at each of the analyzed moments.

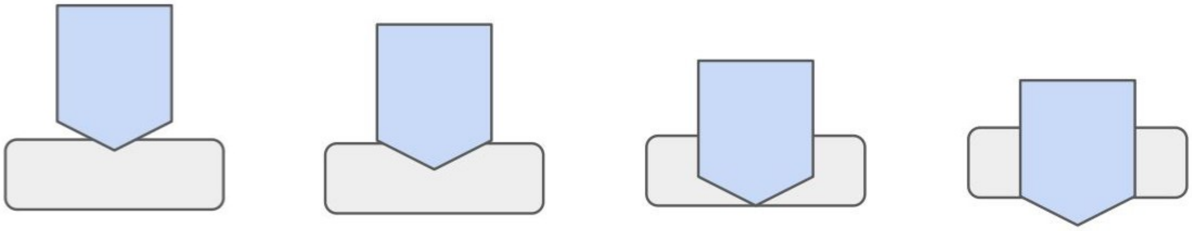

(a) $z = 0.34$ mm (b) $z = 1.49$ mm (c) $z = 2.80$ mm (d) $z = 4.18$ mm

Figure 4.3: Different phases of the drilling process

The first stage considered is the instant when the main cutting edge enters the workpiece. Up to this point, only the chisel edge was engaged with the plate, resulting in a rapid increase in thrust force, reaching nearly its maximum value. The torque, on the other hand, remains negligible.

In the second stage, the corners begin to engage. The thrust forces decrease slightly due to the reduced amount of material to be removed, while the torque rises significantly as contributions from regions farther from the process center become dominant.

At the third instant, the drill has reached the lower surface of the panel. As in stage two, a decrease in cutting force is observed, likely influenced by the reduced distance between the drill tip and the bottom of the workpiece. The torque, however, continues to increase due to the contribution of the margins and remains present as cutting is still occurring at the periphery.

Finally, the last stage corresponds to the exit of the corners from the workpiece. Both thrust force and torque drop to zero, indicating the completion of the drilling process. Residual torque signals are still present due to flanks friction.

Subsequently, the signals obtained from the two drill bits are compared (Figure 4.2).

Overall, the behavior observed during stages 1 and 3 is very similar across the different tests. The most significant differences are found in stages 2 and 4. When the corners engage, a substantial increase (up to 100%) in thrust force is observed. The torque does not exhibit major differences, although a slight increase in values can be noticed. The other major difference in the curves occurs at stage 4. At corner exit, a delay in the signal is observed, attributable to flank wear. Residual torque can still be observed at the end of the drilling process.

4.1.2 Burr measurement

Once the drilling of the specimens is completed, the geometry of the burr is measured for each of them. The measurements are acquired using Alicona 3D Focus and DTI techniques. Exit burrs are measured on 10 specimens for each drill bit, while entry burrs are analyzed only on 5 specimens per drill bit.

The procedure followed is briefly reported below. For the Alicona scanning:

- Data acquisition: 8 radial measurements taken at 45° intervals;
- Data cleaning: invalid values and points with negative z-coordinates are removed, as well as points whose values are 20% higher than the preceding ones;
- Data processing:
  - the same origin is set for all measured points, both in z and r coordinates. The reference coordinate $z = 0$ is defined as the average of the first five measured points. The reference coordinate $r = 0$ is set at the point immediately after the maximum, where the z-coordinate is equal to or less than 80% of that maximum;
  - the burr profile and thickness are extracted, and both mean value and scatter are computed. The thickness is defined as the radial distance from the origin to the point where the burr height decreases to 0.01 mm.

In addition, four measurements at 90° intervals are performed using DTI, from which the mean value and scatter of burr height are calculated. No information is obtained regarding the burr thickness.

Table 4.1 reports the average values and scatter of height and thickness for both entry and exit burrs. The entry burr values for the new tool were not extracted, as their dimensions were found to be negligible.

The increase in tool wear is associated with a growth in burr dimensions, both at the entry and at the exit.

As an example, four 3D images obtained from the scanning of the exit burr are also reported.

	New	**Burr 0.4** [mm]	
	Exit	**Entry**	**Exit**
Height [μm]	34 ± 23	75 ± 7	368 ± 13
Thickness [μm]	62 ± 35	135 ± 27	145 ± 9

Table 4.1: Experimental Burr dimensions

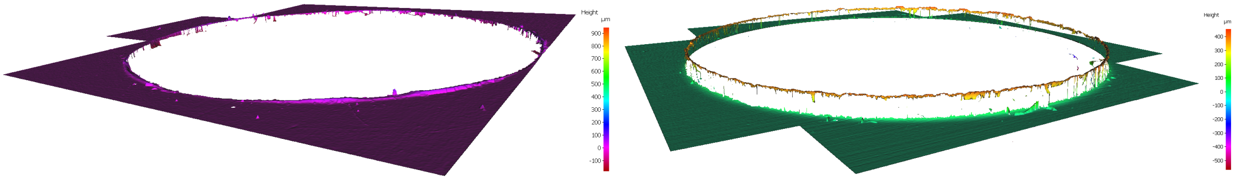

(a) Reference

(b) Burr 0.4 mm

Figure 4.4: Experimental results: 3D Burr scan

4.1.3 Fatigue Test

Once the manufacturing phase was completed, the open-hole specimens were subjected to fatigue testing.

Figure 4.5 shows the Wöhler curves for the two specimen series: the reference specimens drilled with a new tool, and those drilled with a worn tool producing burrs of approximately 0.4 mm. Experimental results indicate that specimens with larger burr dimensions exhibit a significant reduction in fatigue life, a phenomenon referred to as the *knock-down effect*.

Among the hypotheses formulated to explain this behavior, one attributes the cause to the tensile stresses that may arise in regions where large burrs are present. The FEM models aim to assess whether such stresses are indeed generated and whether residual stresses are responsible for the observed decrease in fatigue life.

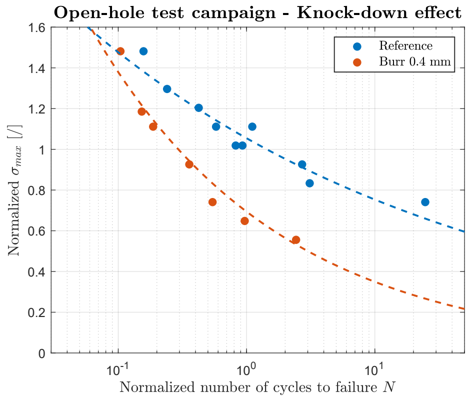

Figure 4.5: Fatigue Test: Fatigue life comparison between specimens with and without burr

4.2 Steady-State simulation

Once data collection is completed, a simulation is performed to accurately represent the drilling process.

As a first step, the positioning of the tool with respect to the workpiece is examined. Since the mesh used does not include reference systems, there are no precise indicators to ensure perfect centering and axial alignment of the drill bit. Furthermore, the general asymmetry of the mesh does not guarantee a symmetric behavior of the two cutting lips.
In drilling processes, in-plane forces and moments are negligible compared to the axial components. Consequently, an optimal positioning should exhibit this characteristic. Figure 4.6 shows the three components of both force and moment. The median values of forces and moments are close to 1% of the median value of the z-components, while their maximum values do not exceed 25% of the z-components. It is therefore concluded that the drill is adequately positioned.

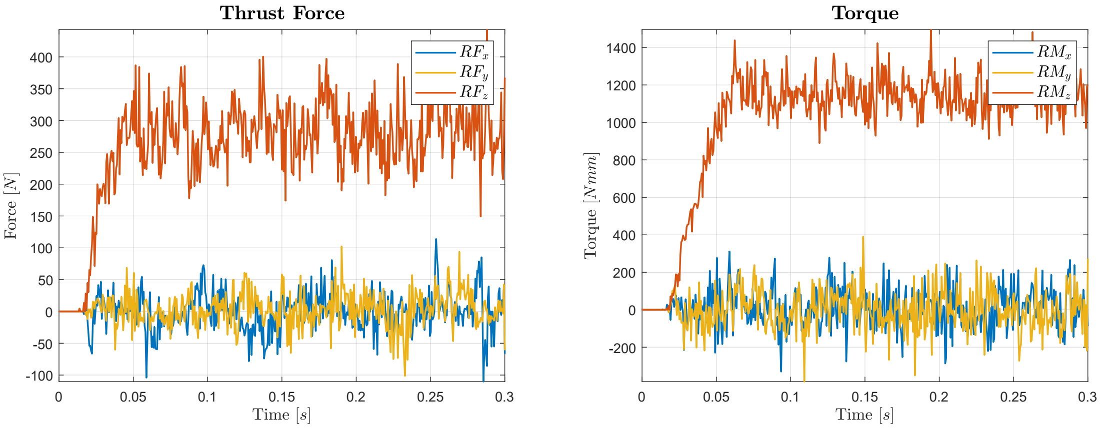

Figure 4.6: Thrust Force and Torque components at steady state

At this stage of the analysis, the median values obtained from the simulation are examined.

A convergence analysis is performed, to study the best suited value for the mesh seed. Results are shown in Figure 4.7. A value of 0.15 *mm* is selected, which ensures torque convergence and results in a 5.8% deviation for the force from the next refinement.

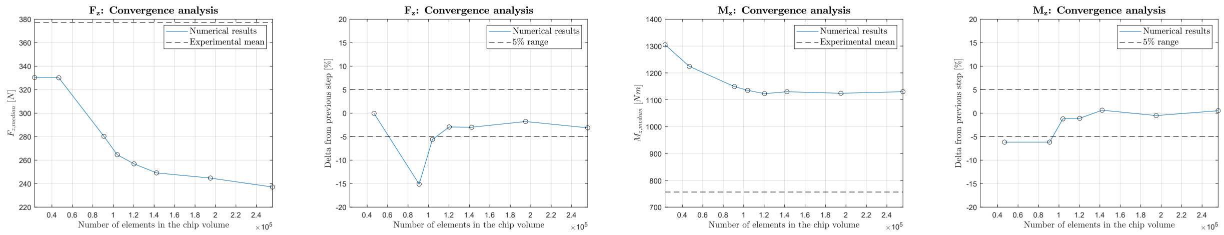

Figure 4.7: Steady-State simulation: Convergence analysis results

The simulated force is 25% lower than the experimental reference force, while the torque is overestimated by 51%. A sensitivity study of the parameters on the final result is therefore carried out. The following parameters are varied:

- Friction coefficient μ
- Fracture energy G_f
- Shear limit τ_{max}
- Temperature T

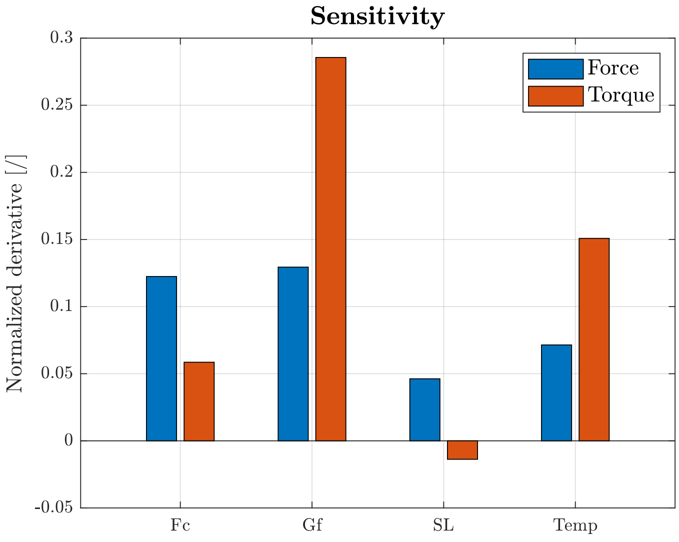

Figure 4.8: Sensitivity analysis results: parameter influence

For each parameter, two analyses are performed, evaluating a reduced and an increased value. Only for the shear limit is a single simulation carried out, where the chosen value is derived from the ratio $A/\sqrt{3}$, neglecting the temperature effect. The derivative is evaluated at the point corresponding to the initial parameter value. The result is then normalized with respect to the experimental values. In Figure 4.8, the bar charts report the influence of the parameters on both force and torque values.

As the parameters increase, a general rise in both force and torque values is observed, except for the shear limit, where the torque remains essentially unchanged. A friction coefficient of 0.6 is therefore selected, as it allows the force value to increase without excessively amplifying the torque, which is already overestimated.

Figure 4.9 shows the updated force and torque trends. The median value now differs by -0.1% for force and by +55.1% for torque. The overestimation of torque is attributed to *shear locking*. In fact, the employment of reduced integration elements are introducing artificial stiffness in azimuthal direction. A potential solution would be the use of C3D8I elements (8-node linear brick, incompatible modes); however, their excessive distortion hinders their practical use.

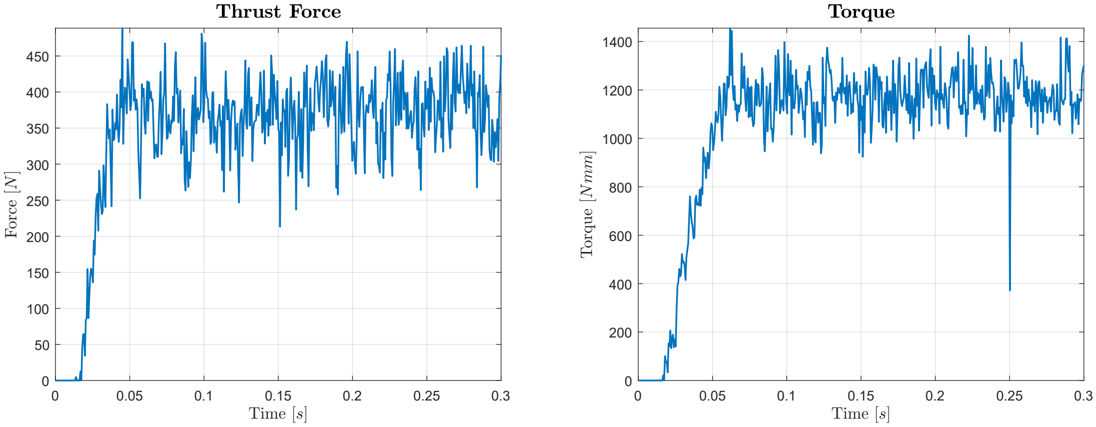

Figure 4.9: Steady-State simulation: Final Thrust Force and Torque

In the literature, some authors have reported similar issues. Abdelhafeez [2] reports a 56% deviation for torque values using Lagrangian elements, while the CEL simulation represented this value more accurately, reducing the deviation to 22%.
The torque error is therefore accepted, and $\mu = 0.6$ is established as the new baseline. In the same paper [2], Abdelhafeez states that a friction coefficient varying from 0.1 to 0.8 has just a minor influence on chip morphology (up to 15%). Given that, the μ chosen is in the range considered by authors in literature.

4.2.1 Worn tool results

The same simulation is repeated using the second drill bit, namely the one that generates a 0.6 mm burr. Considering the delayed engagement of the margins with the workpiece, 10 drill revolutions are simulated, and steady state is assumed when the entire drill bit is fully immersed.

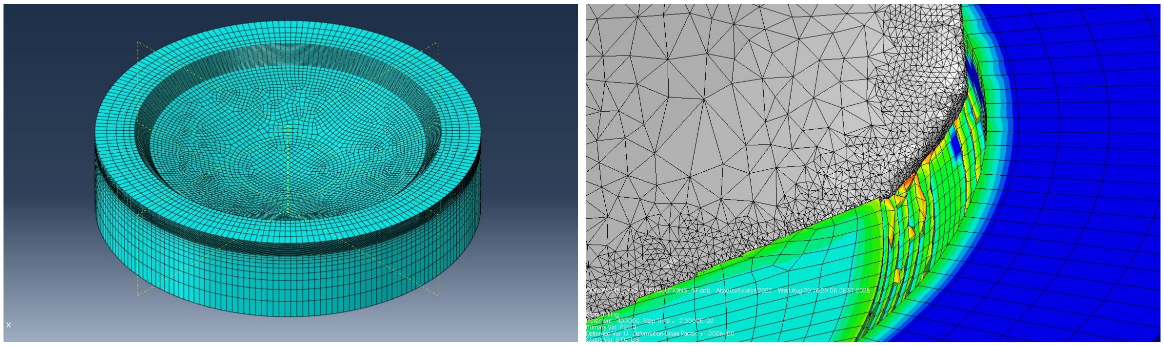

Figure 4.10: Steady-State simulation: Worn tool details

The results show a general reduction in both force and torque compared to the previous simulation. This is attributed to the lack of corner indentation, caused by the coarse mesh, which poorly represents the contact between the tool and the workpiece.

The workpiece is therefore modified by adding a partition corresponding to the drill margins, with a radial width of 4.75 *mm* and a slope of 45.45°. Twenty elements are generated in the radial direction. This new workpiece allows for a shorter simulation time and a more uniform contact representation in the region corresponding to the damaged drill margin. Figure 4.10 shows the mesh of the new part and a detailed view of the margin indentation.

The values obtained with the new model show a -40% difference in thrust force and a 65% difference in torque. Moreover, the expected force peak is not observed.

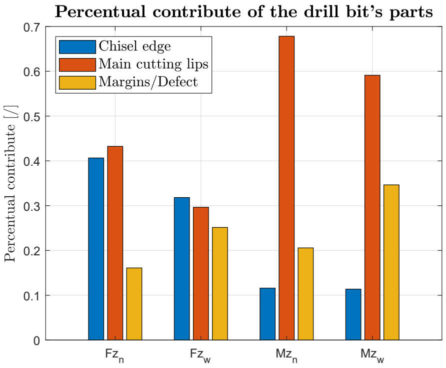

Figure 4.11: Steady-State simulation: Forces components

To study the drill bit's behavior in greater detail, a partition similar to that used in the new workpiece is created in the original one, without changing the slope of the region. Three sets are defined, corresponding to the regions where the main parts of the drill indent: the chisel edge, main cutting lips, and margins.

Figure 4.11 reports the contributions of the three parts to force and torque, normalized with respect to the experimental values of the new drill bit. As expected, 40% of the thrust force is generated by the chisel edge alone, while the torque contribution comes almost entirely from the main cutting lips and the margins. The damaged corners amplify both the force and torque signals, effectively doubling them, but this effect is mitigated by the simultaneous decrease in the signals generated by the chisel edge and cutting lips. This unexpected behavior is likely due to the way the drill initially indents the plate: during the first revolutions, only the margins engage with the workpiece, while the other two regions start cutting with a delay.

The previous analysis made it possible to verify the percentage contribution of the contacts between tool and workpiece in the simulation.
Table 4.2 reports the average values of contact pressure and frictional stress for both drill bits.

	Force [N]	**Percentual contribute [%]**	**Torque [Nmm]**	**Percentual contribute [%]**
Contact pressure	169.94	44.27	1276.50	99.27
Frictional stress	208.65	54.35	30.55	2.38

Table 4.2: Steady-State simulation: Contact contributions

The thrust force therefore depends on similar contributions from contact pressure and frictional stresses, whereas the torque is generated solely by the pressure forces.
This result justifies the choice of the friction coefficient: increasing its value has a significant effect on the thrust force, while its effect on the torque is essentially negligible, since its contribution is nearly zero. This finding can be used to choose the friction coefficient in simulations to better match experimental thrust force measurements, without substantially affecting torque predictions. This allows for a more accurate calibration of the model while keeping computational complexity low.

4.3 Full-Drilling simulation

The Steady-State simulation provided greater insight into the numerical mechanisms arising in drilling models. The parameters investigated serve as the new baseline for the subsequent models.

The Full-Drilling simulation was then performed, with the objective of reproducing the same behaviors observed in the experimental tests (Figure 4.2).

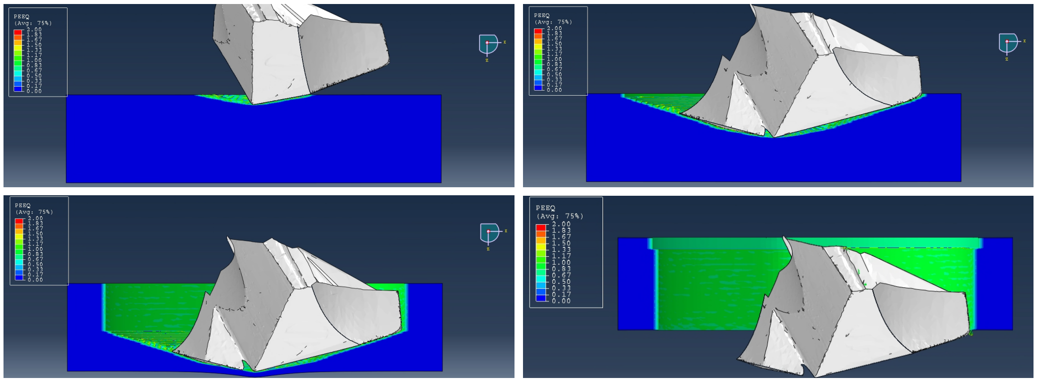

Figure 4.12: New Tool Burr Formation: Burr Formation steps

Figure 4.12 shows the evolution of the drill bit as it penetrates the workpiece: in the top-left image, the chisel edge has just entered; in the top-right, the corners engage the material; in the bottom-left, the drill reaches the lower surface of the plate; and finally, in the bottom-right, the tool exits the workpiece. Figure 4.13 illustrates the formation of the burr dome.

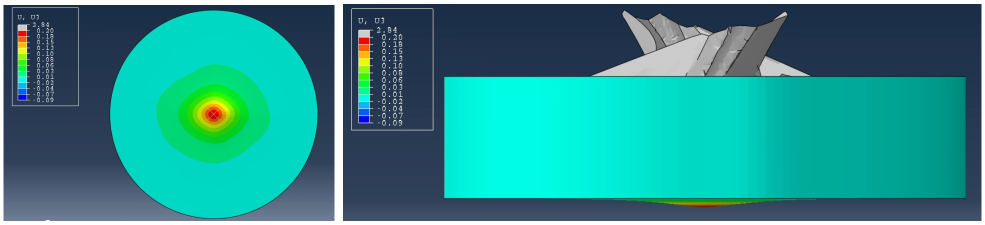

Figure 4.13: New Tool Burr Formation: Dome formation

As with the experimental data, the numerical results exhibit considerable variability between consecutive measurements. The signals were therefore filtered using the same low-pass *Butterworth* filter with a cutoff frequency of 10 Hz. Figure 4.14 shows the numerical thrust force and torque curves together with the filtered signal.

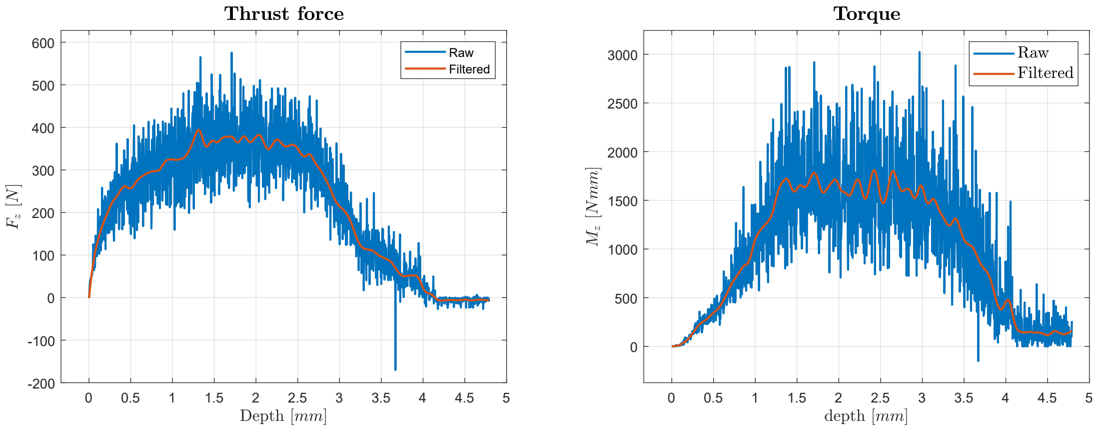

Figure 4.14: Data filtering of numerical results

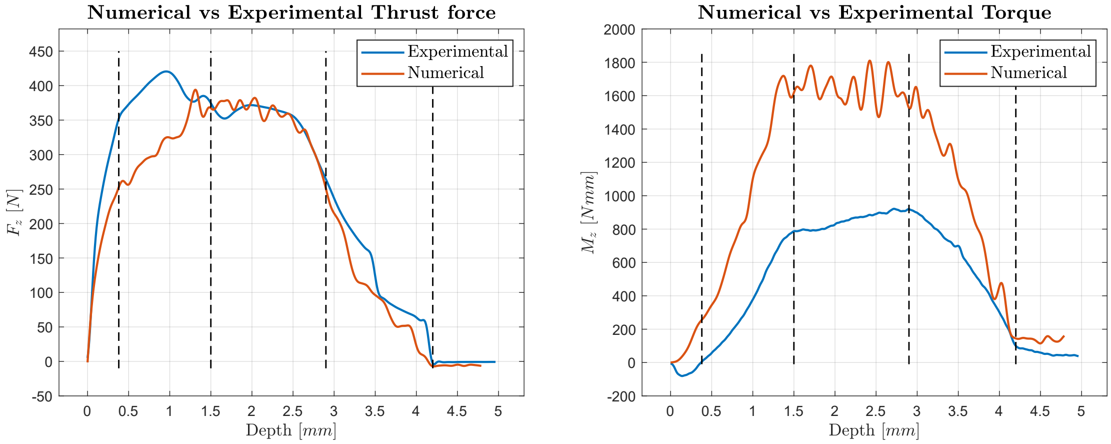

Figure 4.15: Results comparison: Experimental vs Numerical

Figure 4.15 compares the experimental and numerical curves. The thrust force signal accurately reproduces the phenomena analyzed in Section 4.1.1. Three slope changes can be observed at the beginning of penetration, corresponding respectively to the entry of the the chisel edge (center and margins) and the main cutting lips. The contribution of the chisel edge appears slightly underestimated in the initial phase. At steady state, the curves are perfectly overlapped, in agreement with the study carried out in the previous section. Furthermore, the force reductions due to the exit of the drill tip and, subsequently, of the margins from the plate are properly reproduced.

The torque signal also follows the same trends as the experimental tests; however, its amplitude is nearly doubled. An increase of 55% was already expected based on the Steady-State simulation results. In addition, the effects of increased time scaling and mass scaling, contributing another 10–15%, as well as the coarser mesh adopted, contributing an additional 5–10%, must also be considered.

4.3.1 Worn tool results

The same simulation was also reproduced using the worn tool. Figure 4.16 shows the filtering applied to the signals, while Figure 4.17 reports the comparison between the experimental and numerical curves.

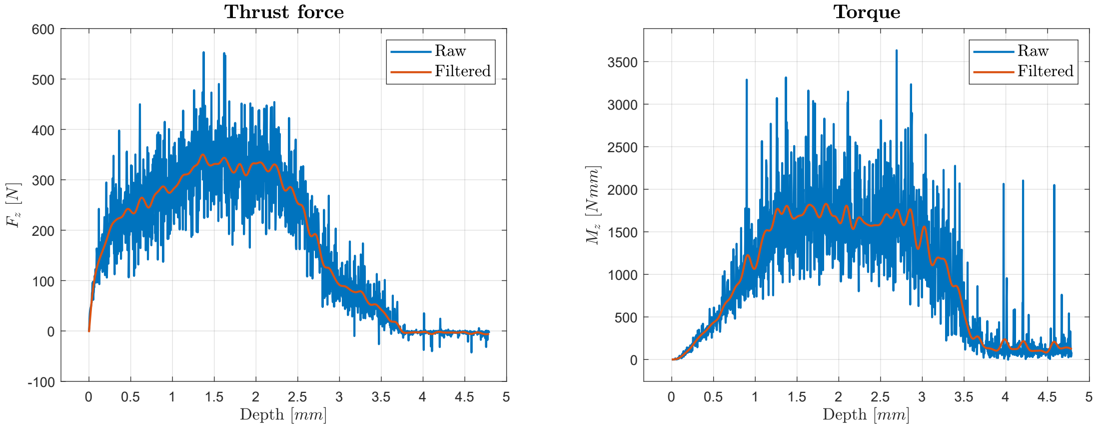

Thrust force

Torque

Figure 4.16: Data filtering of numerical results

As already discussed in the previous section, the force signal is underestimated. Furthermore, both the force and torque signals fail to capture the observed delay. This occurs due to the coarse mesh, which cannot adequately reproduce the contact at the damaged corners. In fact, the elements are eroded and removed before the margins are able to indent the workpiece. A possible solution to this issue would be to increase the number of elements in proximity to the hole walls; however, this option was not pursued in the present study due to the associated high computational cost.

As expected, at the end of the simulation the hole does not exhibit any burr formation. This outcome is again related to the overly coarse mesh: the elements are removed prematurely and do not undergo sufficient plastic deformation. In any case, their size is too large to predict the final geometry. In the following section, through the Burr Formation simulation, the final hole geometry will be analyzed.

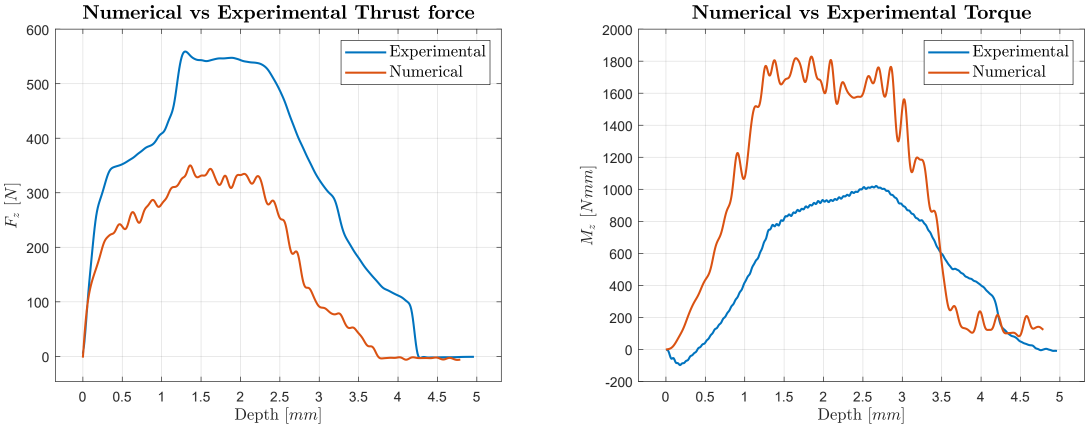

Figure 4.17: Results comparison: Experimental vs Numerical

4.4 One-Way-Assembly simulation

This section presents the results of the drilling simulation involving two stacked plates. Since no direct experimental reference is available for this configuration, a validation of the results cannot be performed. However, a qualitative comparison can be made based on the cutting forces, for which experimental data are available from tests involving the drilling of three stacked plates.

4.4.1 Forces

Figures 4.18 and 4.19 show the extracted and filtered signals of force and torque. Regarding the force trend, a first peak appears as the chisel edge enters the first plate. However, the second peak—corresponding to the entry into the underlying plate—is not observed. This second peak should appear slightly lower than the first one (Figure 4.20), and it is expected to occur even in the absence of a third plate.

In general, the trend can be described as follows: the chisel edge penetrates the plate, leading to a rapid increase in thrust force, which is considerably higher due to the presence of the backup plate. As the drill approaches the lower surface, the force initially decreases—similarly to what was observed in the Full-Drilling simulation. However, in this case, the force rises again as the tool engages the next plate. This phenomenon repeats for the third plate, and finally, the force drops to zero once the tool exits the plate stack.

The current model does not generate interface burrs and therefore cannot fully reproduce the experimental behavior. Further improvements are required to capture this phenomenon accurately.

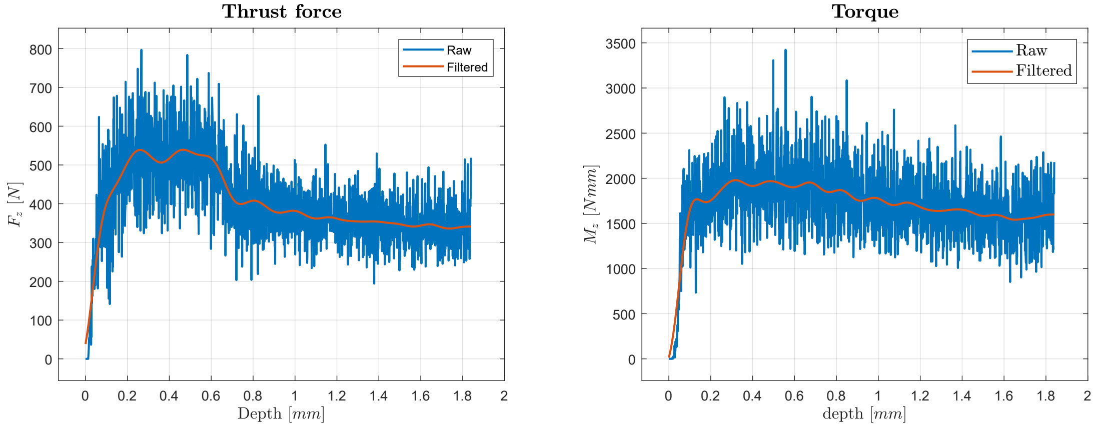

Figure 4.18: Force and Torque in the OWA simulation - New Tool

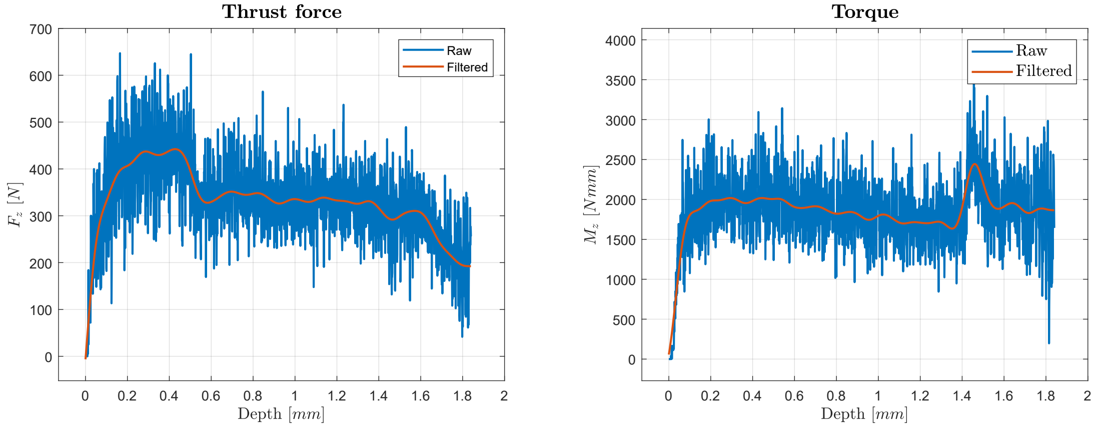

Figure 4.19: Force and Torque in the OWA simulation - Worn Tool

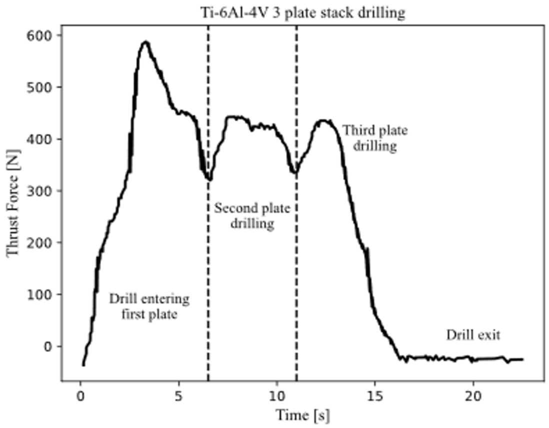

Figure 4.20: Forces in a 3-plate drilling

4.4.2 Gap Evolution

Figure 4.21 shows the relative displacement between the two plates during drilling. The result is reported for the new tool, but since no burrs are generated, the outcome is identical for the worn tool.

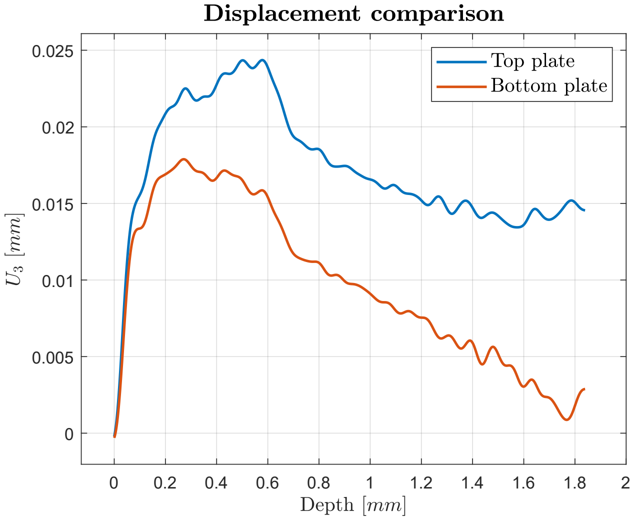

Figure 4.21: Displacement and Gap evolution in the OWA simulation

A difference in the displacement values of the two plates can be observed, confirming the occurrence of differential bending between them. However, the magnitude of this displacement is relatively small ($\sim 10\ \mu m$) and therefore not realistic. The presence of burrs would likely amplify this effect, especially when using the worn drill bit.

4.5 Burr Formation simulation

The data concerning burr geometry are now presented. The geometry at the end of drilling is compared with that obtained after reaming the hole produced with the new tool. A similar analysis is carried out with the worn tool, although in this case reaming is not performed.

Subsequently, the residual stresses on the hole walls are presented. The residual stresses extracted from the simulation with the new tool are then introduced into the subsequent Fatigue Test simulation.

4.5.1 Burr Geometry New Tool

Figure 4.22 shows several stages of the burr formation process obtained from the simulation. The top images illustrate two different instants during material removal, while the bottom ones depict the downward bending of the material followed by its final fracture, leading to the formation of the hole.

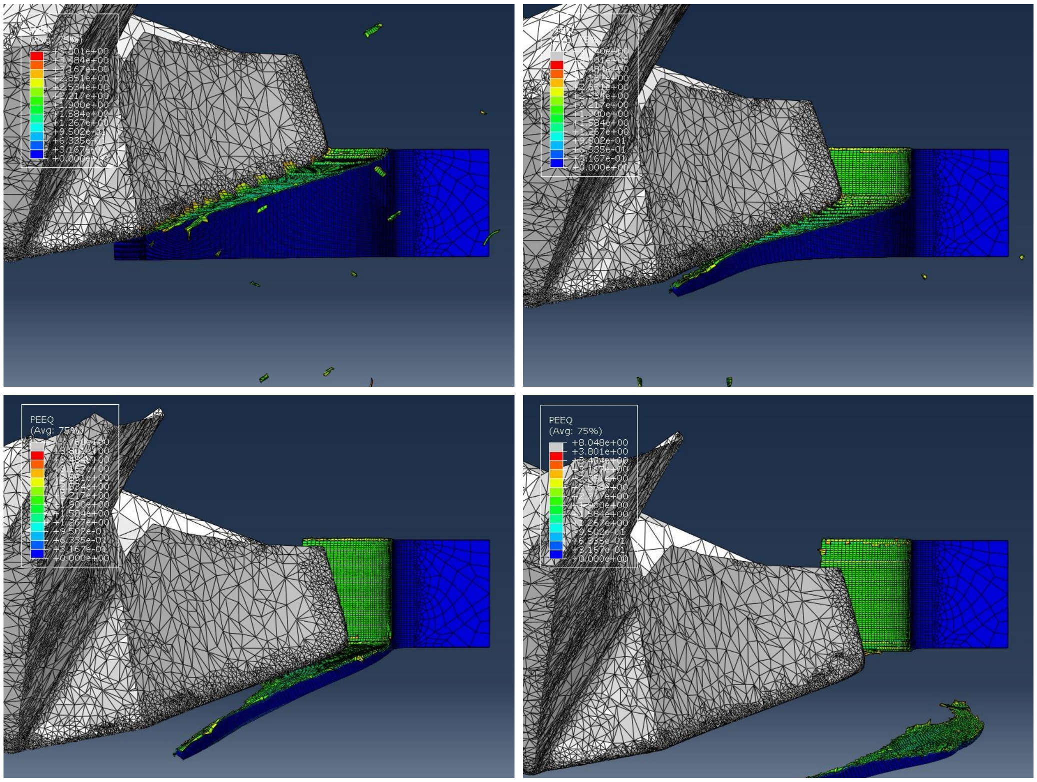

Figure 4.22: New Tool Burr Formation: Burr Formation steps

Additionally, Figure 4.23 reports two contour plots showing, respectively, the equivalent plastic strain (PEEQ) and the burr height expressed in terms of axial displacement (U_3).

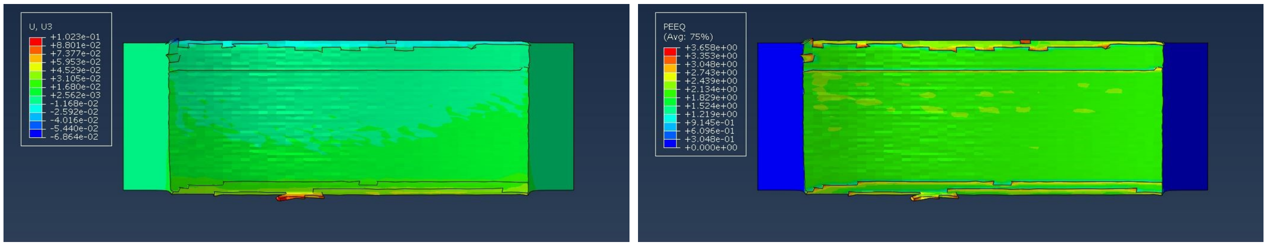

Figure 4.23: New Tool Burr Formation: PEEQ and U3 plots

Data were extracted from the model using the ABAQUS “Path” function. A cylindrical coordinate system was first defined, centered at the theoretical midpoint of the complete workpiece, with radial (r) and azimuthal (θ) axes lying on the lower plane and the z-axis pointing upward.

The axial displacement U_3 was measured for both the entry and exit burrs. The burr geometry was also evaluated by extracting the profiles at the center of the entry side and at several azimuthal positions for the exit side. The results are compared to experimental data, available only for the exit burr.

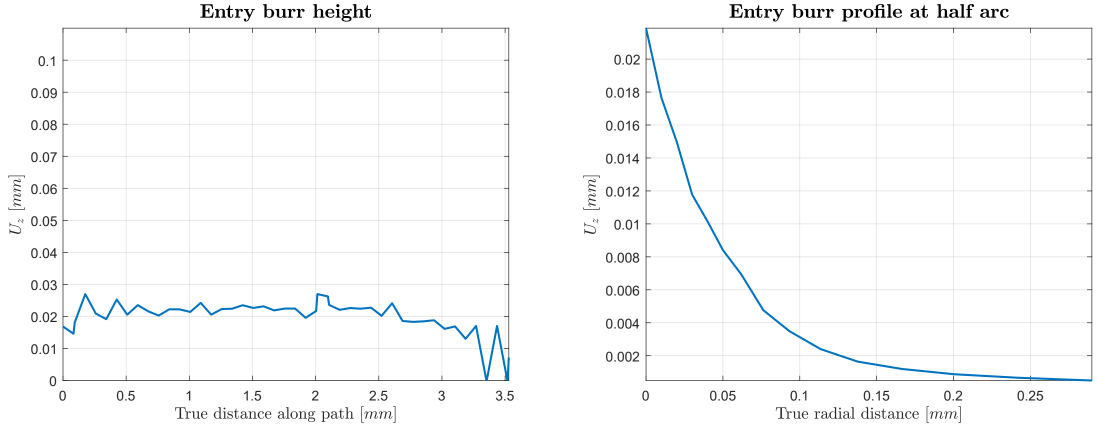

Figure 4.24: New Tool Burr Formation: Entry Burr dimensions

Figure 4.24 presents the entry burr curves. The data near the outer regions are less reliable due to model simplifications. The burr height remains relatively small, ranging between 20 and 30 μm, and the burr thickness is also reduced.

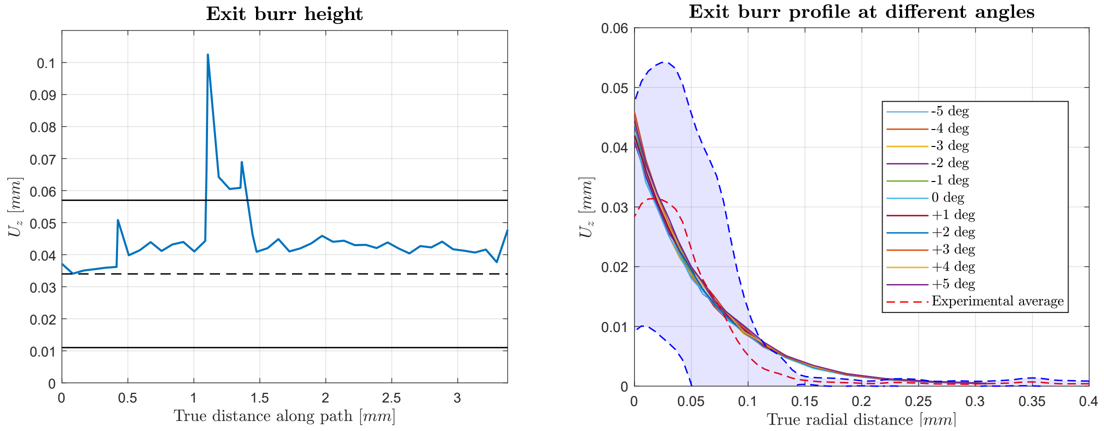

Figure 4.25: New Tool Burr Formation: Exit Burr dimensions

In Figure 4.25, the exit burr data show good agreement with the experimental evidence in the central region. The geometric profiles, extracted at various azimuthal positions, are also consistent with the experimental results.

Afterward, the simulation was restarted to perform the reaming step. Figure 4.26 shows selected stages of this process.

In the simulation, the hole radius increases from 4.76 mm to 4.79 mm. Experimental results show that burr dimensions do not significantly change between drilling and reaming operations, and the simulation appears to reproduce this trend. The burr heights remain within the experimental range, although a slight increase in exit burr thickness is observed.

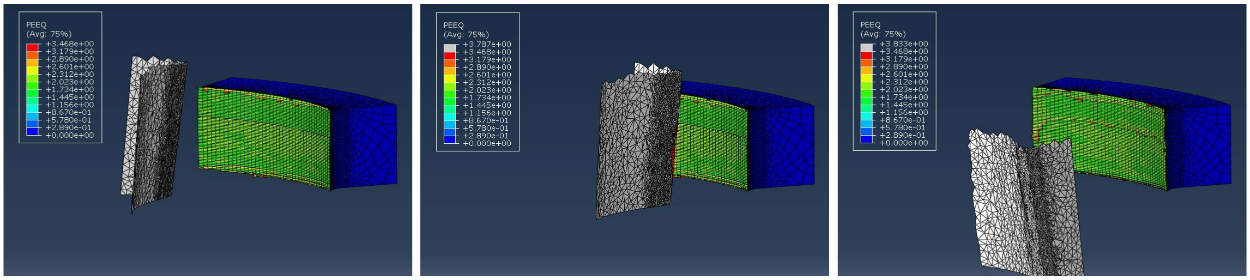

Figure 4.26: New Tool Burr Formation: Reaming steps

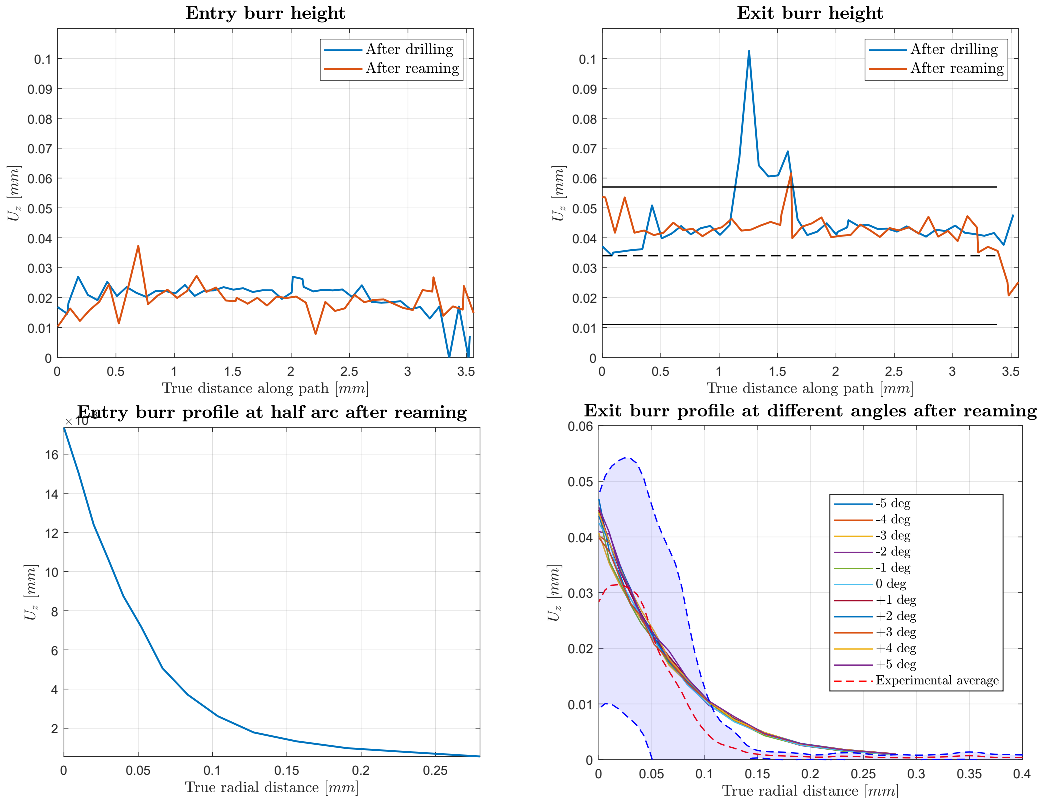

Figure 4.27: New Tool Burr Formation: Burr Heights comparison

4.5.2 Burr Geometry Worn Tool

The same simulation was repeated using the worn tool.

In this case, the material exhibited significant torsion and bending during drilling. These effects became more pronounced toward the end of the process, when the remaining material was thinner and more flexible. Vibrational effects caused wide oscillations of the burr, which was ultimately removed by impact with the flank rather than by the cutting lips.

To address this issue, two steel backup plates ($E = 210000\ MPa$, $\nu = 0.3$) were added to the simulation on both sides of the titanium workpiece to limit torsional and bending effects.

The results reported here correspond to a simulation frame in which the burr is still in its final upright position. Shortly afterward, renewed contact and vibration caused the burr to be completely detached.

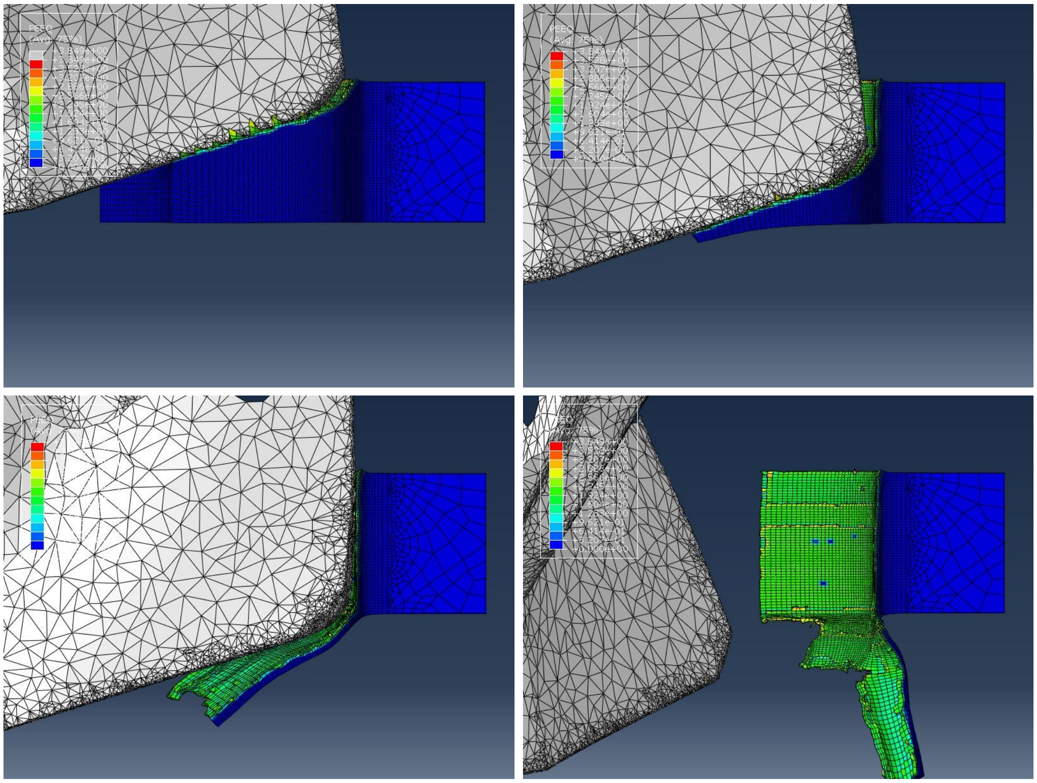

Figure 4.28: Worn Tool Burr Formation: Burr Formation steps

Figure 4.28 illustrates the burr formation mechanism. Clear differences are observed compared to the new tool: the material profile follows the detailed micro-geometry of the worn cutting edge, and the burr exhibits a stronger downward bending without dome detachment.

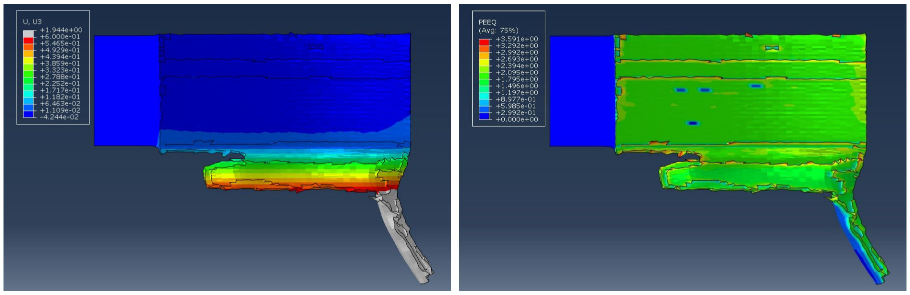

Figure 4.29: Worn Tool Burr Formation: PEEQ and U3 plots

Figure 4.29 presents the final burr geometry and equivalent plastic strain. The model remains a simplification of the real process, but its central region is sufficiently accurate for extracting results. The secondary burr visible on the right side is not considered.

Again, the geometry data were extracted using ABAQUS paths. The results correspond to the end of the drilling stage, since reaming was not simulated. Nonetheless, similar results are expected, as experimental evidence indicates that reaming removes only a few microns of material without significantly affecting burr dimensions.

In this case, experimental data are available for the entry burr. The FEM model does not reproduce this phenomenon accurately, as it is not optimized for the more complex burr formation mechanism occurring on the entry side.

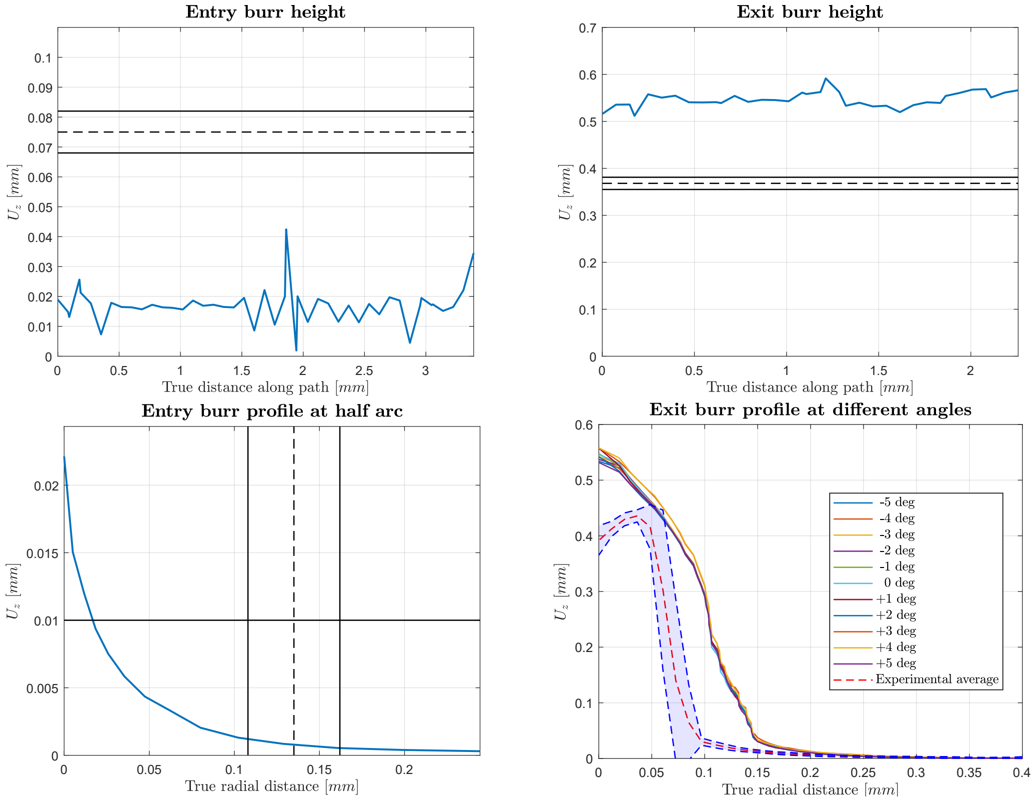

Figure 4.30: New Tool Burr Formation: Burr Heights comparison

In the bottom-right plot of Figure 4.30, burr profiles along different radial paths are reported. The predicted burr height is overestimated by about 25%, while the thickness is overestimated by roughly 50%. Nevertheless, the qualitative shape of the FEM profile shows good agreement with the experimental observations. Therefore, the model can be considered validated, and the post-manufacturing material state is expected to be consistent with the real one.

4.5.3 Residual stresses New Tool

The model, initially validated in terms of force and torque, was also validated with respect to the final burr geometry. The next step consists in extracting the residual stress profile within the material.

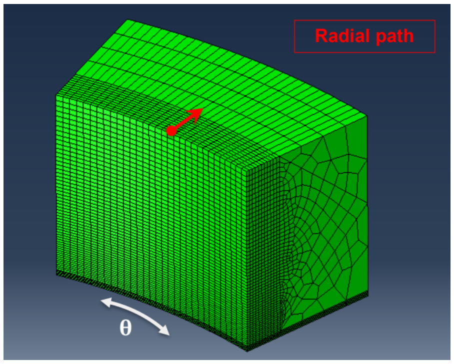

Figure 4.31: Burr Formation simulation: cylindrical coordinate system

The "Path" function is again employed to extract the stress values along the three axes of a cylindrical coordinate system (Figure 4.31). The reported values correspond to the nodal stresses along the defined radial paths. ABAQUS computes stresses at the integration points; therefore, the nodal stresses result from the averaging of the values from all elements sharing the same node. This averaging occurs only if the stress values are within 75% of each other; otherwise, the value is disregarded.

Figure 4.32 shows the stress curves for the three components, evaluated along radial paths at different heights of the workpiece. The origin is set at the lower surface. S11 corresponds to σ_{rr}, S22 to $\sigma_{\theta\theta}$ and S33 to σ_{zz}.

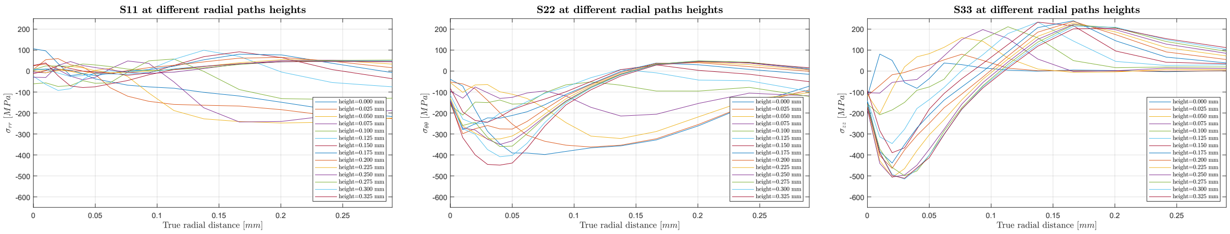

Figure 4.32: New Tool Burr Formation: Stresses on radial paths after drilling

Observing the left-hand side of the curves, corresponding to the hole wall, all three components show values close to zero. In particular, for $\sigma_{\theta\theta}$, no significant tensile stress is observed for the curves at lower heights (near the burr region).

Furthermore, beyond a radial distance of approximately 0.25–0.30 mm, the curves exhibit a very similar trend. This region, far from the free boundaries of the hole, is referred to as the *steady-state* zone. The stress distributions in this region show minimal variation and are extracted for subsequent use in the Fatigue Test simulation.

The stress state was also extracted after the reaming simulation.

Figure 4.33 presents two bands corresponding to the radial stress distributions for the three stress components, before and after reaming, in the steady-state region. The bands represent the minimum and maximum stress values at each radial position. The values of σ_{rr} are negligible both before and after reaming, whereas $\sigma_{\theta\theta}$ and σ_{zz} are compressive, with the former showing partial relaxation following reaming.

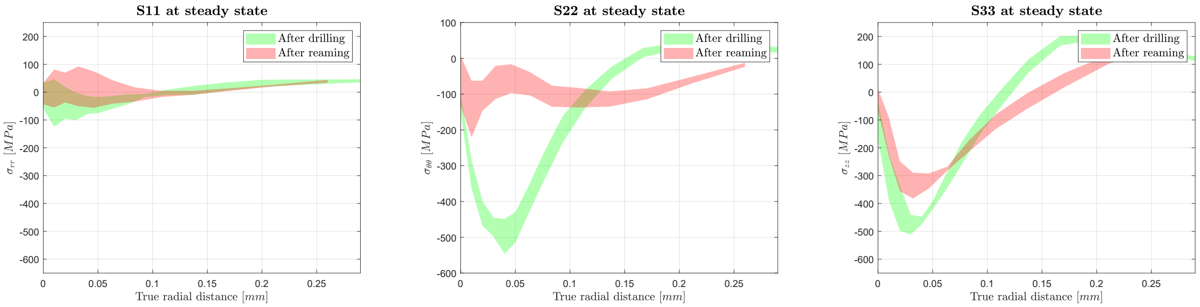

Figure 4.33: New Tool Burr Formation: Stresses on radial path at steady state - comparison

The mean value of the bands corresponding to the reamed configuration is stored and represents the stress distribution considered in the following subsection.

4.5.4 Residual stresses Worn Tool

The same procedure was applied to the simulation performed with the worn tool. In this case, however, only the drilling phase was simulated.

Figure 4.34 compares the stress bands for the two tool configurations after drilling.

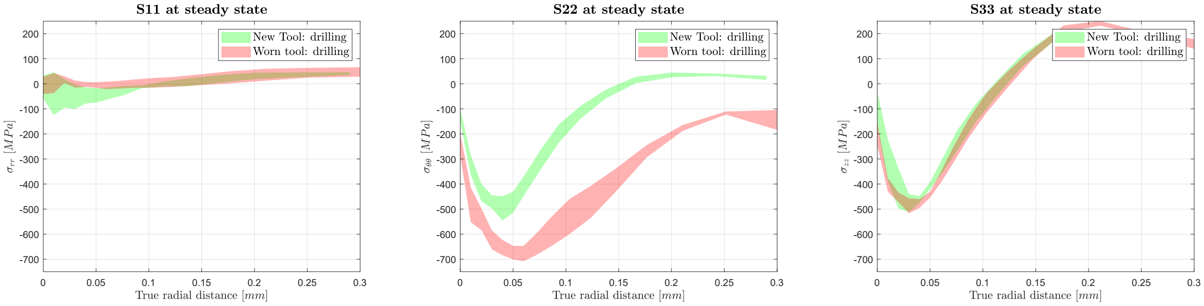

Figure 4.34: Worn Tool Burr Formation: Stresses on radial path at steady state - comparison

The curves are very similar, with slightly higher compressive values observed for $\sigma_{\theta\theta}$. Considering the overall similarity between the two cases, a comparable stress distribution to that in Figure 4.33 is expected after reaming.

4.5.5 Thermal Stresses

Once the mechanical stress distribution has been obtained, a preliminary assessment of the influence of thermal effects is performed. The Thermal Stresses simulation is carried out, and after cooling the model, the resulting residual thermal stresses are extracted.

Figure 4.35 shows the resulting stress distributions in the model and the radial paths of the three stress components. The radial and axial components are found to be negligible, while significant tensile stresses are observed in the azimuthal direction. Debard reported temperatures of approximately 500 °C in the contact zone [18]; however, such values are not uniform throughout the workpiece. The most realistic approximation for the model is likely around 200 °C, for which tensile stresses of about 200 MPa are observed.

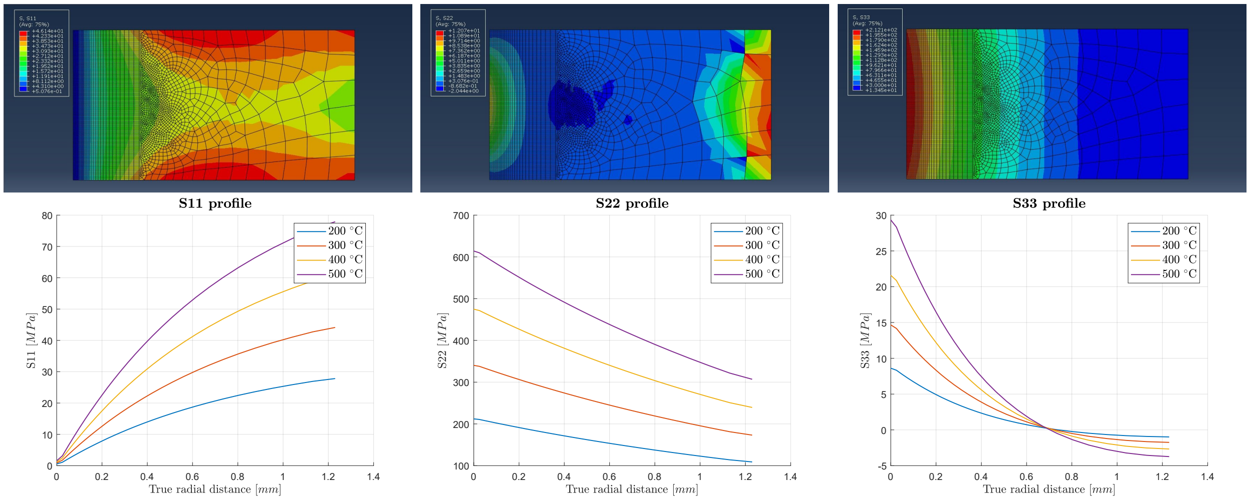

Figure 4.35: Thermal Stresses study: Stresses distribution and stresses on radial paths

4.6 Fatigue Test simulation

This subsection aims to evaluate the effect of residual stresses on the fatigue life of the specimen.

The stress field is introduced into the model using the SIGINI subroutine, followed by a relaxation step. It should be noted that the initial distribution is assumed constant through the specimen thickness.

Figure 4.36 shows the distribution of the stress $\sigma_{\theta\theta}$ along a vertical path through the thickness. The relaxed distribution, which should coincide with the steady-state region, satisfactorily reproduces the stress trend even near the burr region. This occurs because a slight stress relaxation is observed close to the free-edge, similar to the one detected near the burr.

The model therefore provides a good approximation of the post-manufacturing stress distribution, despite the simplifications introduced.

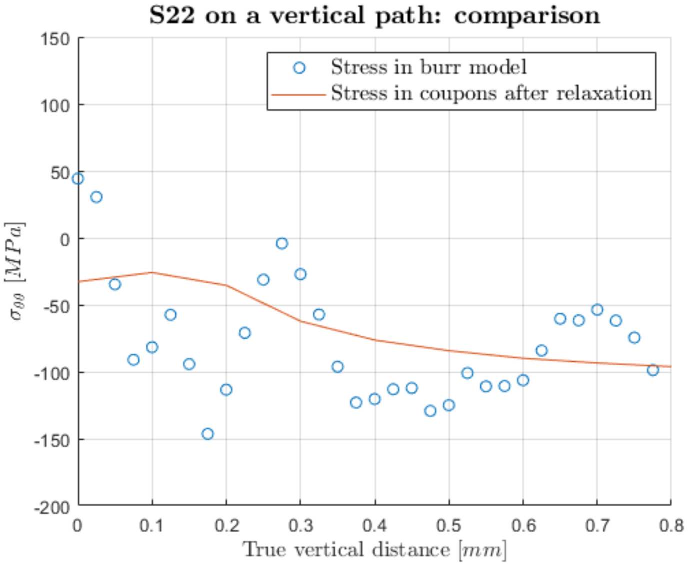

Figure 4.36: Fatigue Test: Stress $\sigma_{\theta\theta}$ profile after relaxation

Figures 4.37 and 4.38 show the stress distributions at the maximum load of the fatigue cycle. The distributions appear very similar between the cases with and without residual stresses (left and right, respectively). However, a noticeable difference is observed at the minimum load.

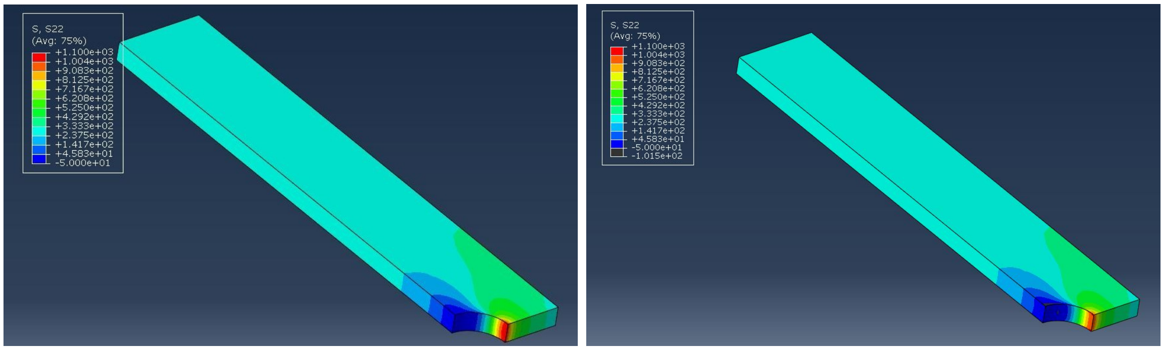

Figure 4.37: Fatigue Test: Stress σ_{yy} distribution at maximum load

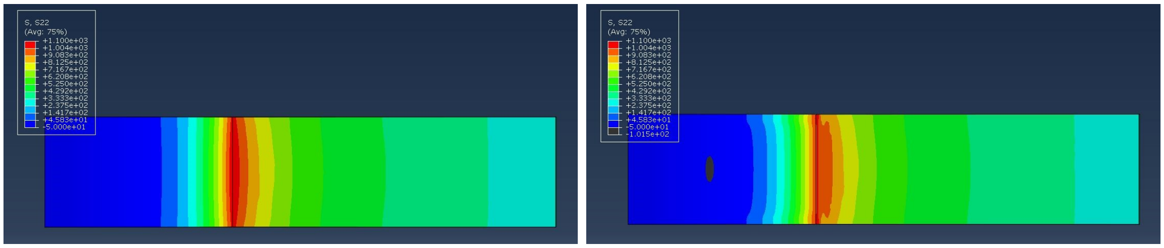

Figure 4.38: Fatigue Test: Stress σ_{yy} distribution at maximum load - hole detail

The stress concentration factor k_t is defined as:

$$k_t = \frac{\sigma_{max,local}}{\sigma_{nominal}} \tag{4.1}$$

and represents how much a geometric discontinuity, such as a hole, amplifies local stresses compared to the nominal one. For circular holes, $k_t = 3.6$.

The load ratio R is defined as:

$$R = \frac{k_{t,minload}}{k_{t,maxload}} \tag{4.2}$$

and characterizes the loading cycle:

- $R = -1$: fully reversed (tension–compression);
- $R = 0$: pulsating (from 0 to maximum load);
- $R > 0$: always positive (no load reversal).

In this simulation, a fully positive loading cycle is applied ($R > 0$). A high R value (approaching 1) has two opposite effects:

- at low loads, it implies a smaller stress amplitude, beneficial to fatigue life;
- at high loads, it results in a higher mean stress, thus penalizing fatigue life.

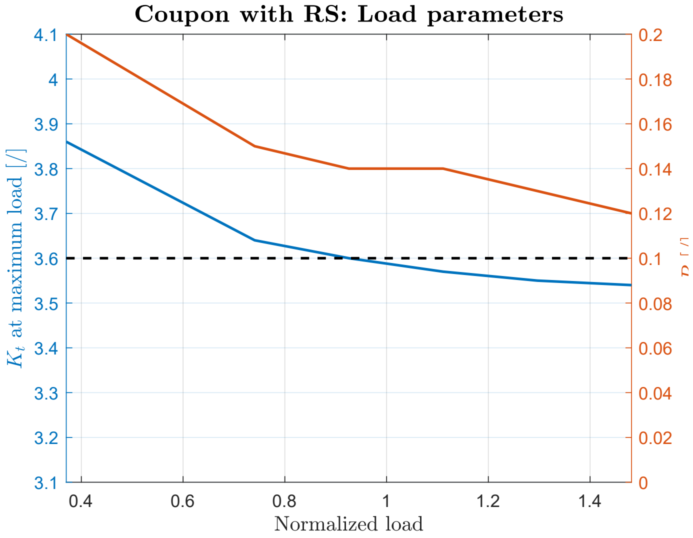

Figure 4.39: Fatigue Test: k_t and R parameters

Figure 4.39 reports the extracted parameters. The dashed line represents the k_t and R values for the specimen without residual stresses, while the blue and red curves correspond to the cases with stresses. The stress concentration factor k_t shows a maximum deviation of about 10%, confirming the qualitative similarity observed in Figure 4.38. On the other hand, R varies between 20% and 100%, with larger differences at lower load levels. This variation positively affects fatigue life, suggesting a stronger divergence between fatigue curves at lower applied loads.

Finally, the Dang Van fatigue criterion is applied to the simulation results, and the corresponding Wöhler curves are plotted for cases with and without residual stresses (Figure 4.40). The case with residual stresses is compared with the experimentally tested specimens, while the stress-free case corresponds to the thermally treated specimens. Both curves show good agreement with experiments, with a slight shift at higher loads — where the elastic material assumption becomes less accurate.

Residual compressive stresses prove beneficial for fatigue life, and the increased R values at lower loads further shift the curve to the right.

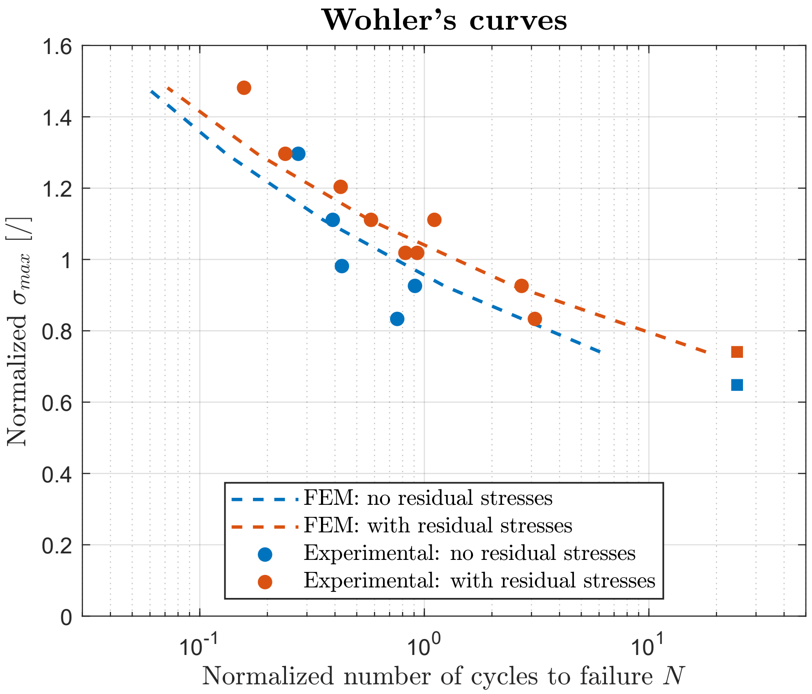

Figure 4.40: Fatigue Test: Fatigue life comparison between experimental and FEM results

Given the similarity in the residual stress profiles obtained after manufacturing with the new and worn tools, the fatigue curve for the worn tool is expected to follow a similar trend to the red one. Therefore, the knock-down effect observed experimentally is not expected to arise from residual stresses.

This conclusion is supported by experimental results (Figure 4.41), showing that specimens subjected to thermal stress-relief and untreated ones exhibit almost identical fatigue lives. Hence, the reduction in fatigue performance must originate from microstructural mechanisms triggered by burr formation rather than from residual stress effects.

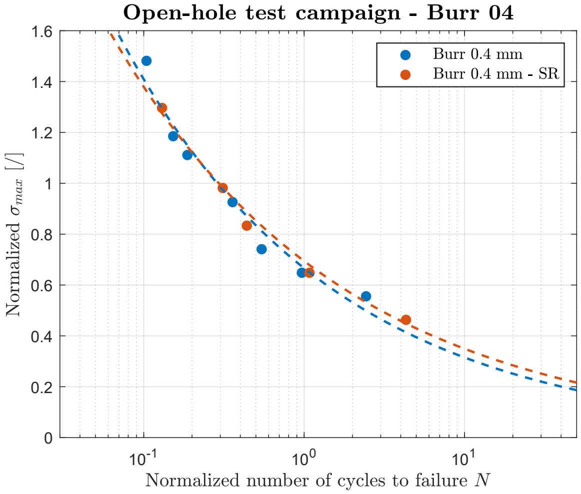

Figure 4.41: Fatigue Test: Fatigue life comparison between specimens with and without thermal treatment

5 Future Work

In this work, it has been demonstrated that residual stresses are not responsible for the knockdown effect observed in the experimental fatigue life tests. Nevertheless, several directions for further developments can be identified.

First, to reinforce the reliability of the current results, a mesh convergence study on the burr formation model should be carried out. This would allow a better understanding and reduction of mesh-dependency effects on the results, both in terms of burr dimensions and residual stress distribution.

Second, the study with the worn drill bit still needs to be completed: reaming should be performed, and the corresponding fatigue curves extracted to validate the findings.

Regarding the fatigue test simulations, an important development would be to include in the model a variable stress distribution across the specimen thickness, as well as the localized plasticity and damage observed on the hole walls. This would improve the level of detail and accuracy of the simulations.

Finally, the same methodology could be extended to interface burrs, considering the presence of a background plate as in OWA processes. Starting from the proposed model and validating it in terms of force, torque, and burr dimensions, the fatigue life of specimens produced under these conditions could also be determined.

6 Conclusions

This project enabled the reproduction of the entire life cycle of an open-hole fatigue test, from its manufacturing to the testing phase, through finite element simulations.

The overall process was divided into simpler simulation steps, which allowed first to validate the numerical model and then to extract meaningful conclusions. This modular approach was necessary to deal with the demanding mesh requirements of drilling and reaming simulations, given their inherently 3D and non-axisymmetric nature.

In the first stage, only four revolutions of the drill bit were simulated under steady-state conditions. This initial step made it possible to calibrate the model parameters and reproduce the correct amplitude of force and torque signals.

The second simulation, corresponding to the full drilling operation, successfully reproduced the entire drilling process. The force and torque curves obtained numerically showed the same trends as those observed in the experimental tests.

A third model focusing on burr formation was then developed, requiring a finer mesh to accurately capture the phenomenon. With this model, both drilling and reaming phases were simulated. The model was validated in terms of burr dimensions, namely height and thickness, showing good agreement with experimental measurements. Moreover, based on the resulting drilled hole, the post-drilling material state was analyzed by extracting the circumferential residual stresses at the hole wall. The hypothesis of having tensile stresses near the burr region was not confirmed, although a slight difference in amplitude was observed between the regions close to and farther from the burr. Compressive stresses were found in both the azimuthal and axial directions, with the former relaxing after the reaming operation.

The residual stresses extracted from a steady-state region of the distribution were then imported into the final model, used to simulate the fatigue test. Two cases were considered: one specimen without residual stresses, and another with the stresses introduced as a constant distribution through the specimen thickness. Several tensile loading conditions were applied, and using the Dang Van criterion, the fatigue life was estimated from the stress distribution within the specimen.

The results showed a rightward shift of the fatigue curves when residual stresses were included, indicating the beneficial effect of compressive stresses on fatigue life. The fatigue curves obtained from the FEM simulations exhibited excellent agreement with the experimental data.

Although the reaming simulation following drilling with the worn tool was not performed, the initial 3D stress distribution, very similar to that obtained with the new tool, suggests that the final stress state after manufacturing would also be comparable. Consequently, the corresponding fatigue curves would likely coincide. Residual stresses can therefore be ruled out as the cause of the knock-down effect observed experimentally. This finding confirms the experimental evidence: relaxing the stresses through heat treatment does not allow the specimen to recover its mechanical properties, indicating that the detrimental effect should not be attributed to the residual stresses induced by hole machining.

References

[1] M. Aamir, K. Giasin, M. Tolouei-Rad, and A. Vafadar. A review: drilling performance and hole quality of aluminium alloys for aerospace applications. *Journal of Materials Research and Technology*, 9:12484–12500, 2020. DOI: `https://doi.org/10.1016/j.jmrt.2020.09.003`.

[2] A. Abdelhafeez, S.L. Soo, and D. Aspinwall. A coupled eulerian lagrangian finite element model of drilling titanium and aluminium alloys. *SAE International Journal of Aerospace*, 2016. DOI: `https://doi.org/10.4271/2016-01-2126`.

[3] Altair Engineering Inc. *Multiaxial Fatigue – Dang Van Criterion.* Altair Engineering Inc., 2022. Accessed: 2025-10-12.

[4] S. Amini, M. Lotfi, H. Paktinat, and M. Kazemiyoun. Characterization of vibratory turning in cutting zone using a pneumatic quick-stop device. *Journal of Engineering Science and Technology*, 2017. DOI: `https://doi.org/10.1016/j.jestch.2017.03.003`.

[5] J. Aurich. *SpanSauber: Untersuchung zur Beherrschung der Sauberkeit von zerspanend hergestellten Bauteilen.* PhD thesis, Technische Universität Kaiserslautern, 2006.

[6] J.C. Aurich, D. Dornfeld, P.J. Arrazola, V. Franke, L. Leitz, and S. Min. Burrs—analysis, control and removal. *CIRP Annals*, 58:519–542, 2009. DOI: `https://doi.org/10.1016/j.cirp.2009.09.004`.

[7] M.C. Avila and D.A. Dornfeld. On the face milling burr formation mechanisms and minimization strategies at high tool. In *UC Berkeley Lab. Manufacturing Sustainability*, pages 191–200, 2004.

[8] K. Berger. Burr reduction investment - production costs - burr reduction - prediction of burrs. In *Proceedings of the HPC Workshop*, Paris, 2002. CIRP.

[9] F. Berto, A. Campagnolo, T. Welo, S. Vantadori, and A. Carpinteri. Multiaxial fatigue strength of titanium alloys. *Frattura ed Integrità Strutturale*, 11:79–89, 06 2017. DOI: `https://doi.org/10.3221/IGF-ESIS.41.12`.

[10] C. Bonnet. *Analyse multi-échelle du chargement thermomécanique induit au cours du perçage du Ti-6Al-4V.* PhD thesis, École nationale des Mines d'Albi-Carmaux, 2021. URL: `http://www.theses.fr/2021EMAC0021`.

[11] G.-L. Chern. Experimental observation and analysis of burr formation mechanisms in face milling of aluminum alloys. *International Journal of Machine Tools and Manufacture*, 46:1517–1525, 2006. DOI: `https://doi.org/10.1016/j.ijmachtools.2005.09.006`.

[12] G.-L. Chern. Study on mechanisms of burr formation and edge breakout near the exit of orthogonal cutting. *Journal of Materials Processing Technology*, 176:152–157, 2006. DOI: `https://doi.org/10.1016/j.jmatprotec.2006.03.127`.

[13] G.-L. Chern and D.A. Dornfeld. Burr/breakout model development and experimental verification. *Journal of Engineering Materials and Technology*, 118:201–206, 1996. DOI: `https://doi.org/10.1115/1.2804887`.

[14] J. Choi and S. Min. Modeling of inter-layer gap formation in drilling of a multi-layered material. Technical report, UC Berkeley Lab. Manufacturing Sustainability, 2003. URL: `https://escholarship.org/uc/item/2vb4t7gq`.

[15] J. Choi, S. Min, and D. Dornfeld. Finite element modeling of burr formation in drilling of a multi-layered material. Technical report, UC Berkeley Lab. Manufacturing Sustainability, n.d. URL: `https://escholarship.org/uc/item/2vb4t7gq`.

[16] B. Debard, M. Cherif, P.-A. Rey, and J. Barboule. Modelization and optimization of the drilling process of aeronautical structures for the "one way assembly": Cutting simulation report, 2023.

[17] B. Debard, M. Cherif, P.-A. Rey, and J. Barboule. Modelization and optimization of the drilling process of aeronautical structures for the "one way assembly": Interrupted tests report, 2023.

[18] B. Debard, P.-A. Rey, M. Cherif, T. Chiron, A. Sommier, and T. Chavatte. Experimental analysis of burr formation during ti6al4v drilling. In *Material Forming - ESAFORM 2024, Materials Research Proceedings*, volume 41, pages 2065–2074, 2024. DOI: `https://doi.org/10.21741/9781644903131-228`.

[19] A. Vazquez del Rey Perdomo. Internship report: Fem simulation of drilling burr formation, 2024.

[20] W.J. Deng, W. Xia, and Y. Tang. Finite element simulation for burr formation near the exit of orthogonal cutting. *International Journal of Advanced Manufacturing Technology*, 43:1035–1045, 2009. DOI: `https://doi.org/10.1007/s00170-008-1784-y`.

[21] S. Van der Veen. Predicting static and dynamic crack initiation accounting for stress-state and material orthotropy. *RP1507503*, 2015.

[22] D. Dornfeld and S. Min. A review of burr formation in machining. In J.C. Aurich and D. Dornfeld, editors, *Burrs - Analysis, Control and Removal*, pages 3–11. Springer Berlin Heidelberg, Berlin, Heidelberg, 2010. DOI: `https://doi.org/10.1007/978-3-642-00568-8_1`.

[23] D.A. Dornfeldl, J.S. Kim, H. Dechow, J. Hewson, and L.J. Chen. Drilling burr formation in titanium alloy, ti-6al-4v. *CIRP Annals*, 48:73–76, 1999. DOI: `https://doi.org/10.1016/S0007-8506(07)63134-5`.

[24] B.J. Durham. Determining appropriate levels of robotic automation in commercial aircraft nacelle assembly. Master's thesis, MIT Sloan School of Management, 2014. URL: `http://hdl.handle.net/1721.1/90609`.

[25] C. Efstathiou, D. Vakondios, A. Lyronis, K. Sofiakis, and A. Antoniadis. Finite element modeling and experimental study of burr formation in drilling processes. In *Proceedings of the ASME International Mechanical Engineering Congress and Exposition*, volume 2, page V002T02A021a, Phoenix, Arizona, USA, 2016. DOI: `https://doi.org/10.1115/IMECE2016-66026`.

[26] S. Frutos-Taravillo, E. Paroissien, Y. Landon, S. Schwartz, M. Fressinet, and C. Chirol. A review on metallic drilling burrs: Geometry, formation, and effect on the mechanical strength of metallic assemblies. *ASME*, 147, 2025.

[27] K.K. Gajrani, V. Divse, and S.S. Joshi. Burr reduction in drilling titanium using drills with peripheral slits. *Transactions of the Indian Institute of Metals*, 74:1155–1172, 2021. DOI: `https://doi.org/10.1007/s12666-021-02271-0`.

[28] L.K. Gillespie. *State of the Art of General Deburring*. 1974.

[29] L.K. Gillespie. Burrs produced by drilling. Technical report, 1976. DOI: `https://doi.org/10.2172/7351762`.

[30] L.K. Gillespie. Burrs produced by end milling. Technical report, 1976. DOI: `https://doi.org/10.2172/7259917`.

[31] L.K. Gillespie. Deburring precision miniature parts. *Precision Engineering*, 1:189–198, 1979. DOI: `https://doi.org/10.1016/0141-6359(79)90099-0`.

[32] L.K. Gillespie and P.T. Blotter. The formation and properties of machining burrs. *Journal of Engineering for Industry*, 98:66–74, 1976. DOI: `https://doi.org/10.1115/1.3438875`.

[33] Y.B. Guo and D.A. Dornfeld. Finite element modeling of burr formation process in drilling 304 stainless steel. *Journal of Manufacturing Science and Engineering*, 122:612–619, 2000. DOI: `https://doi.org/10.1115/1.1285885`.

[34] M. Harzallah. *Caractérisation in-situ et modélisation des mécanismes et couplages thermomécaniques en usinage : application à l'alliage de titane Ti-6Al-4V*. PhD thesis, 2018. HAL Id: tel-01861377, URL: `https://theses.hal.science/tel-01861377`.

[35] M. Hashimura, Y.P. Chang, and D. Dornfeld. Analysis of burr formation mechanism in orthogonal cutting. *Journal of Manufacturing Science and Engineering*, 121:1–7, 1999. DOI: `https://doi.org/10.1115/1.2830569`.

[36] A. Abdelhafeez Hassan, S.L. Soo, D.K. Aspinwall, D. Arnold, and A. Dowson. An analytical model to predict interlayer burr size following drilling of cfrp-metallic stack assemblies. *CIRP Annals*, 69:109–112, 2020. DOI: `https://doi.org/10.1016/j.cirp.2020.04.038`.

[37] M. Hafiz Hassan, A. Jamaluddin, G. Franz, C. Yi Shen, and R. Mahmoodian. Effects of twist drill geometry and drilling parameters on cfrp-aluminum stack up in single shot drilling. *Composites Science*, 2, 2021. DOI: `https://doi.org/10.3390/jcs5070189`.

[38] Hellstern. Investigation of interlayer burr formation in the drilling of stacked aluminium sheets. Master's thesis, Georgia Institute of Technology, 2009. URL: `http://hdl.handle.net/1853/29650`.

[39] W. Hockauf. Burr reduction investment—production costs—burr reduction—prediction of burrs. In *CIRP HPC Workshop*, Paris, 2002.

[40] J. Huang, Y.H. Xiong, J.G. Huang, and G.C. Wang. Finite element analysis of burr formation in micro-machining. *Applied Mechanics and Materials*, 487:225–229, 2014. DOI: `https://doi.org/10.4028/www.scientific.net/AMM.487.225`.

[41] O. Isbilir and E. Ghassemieh. Finite element analysis of drilling of titanium alloy. *Procedia Engineering*, 10:1877–1882, 2011. DOI: `https://doi.org/10.1016/j.proeng.2011.04.312`.

[42] ISO. Iso 13715 - sizes of edges.pdf, 2000. URL: `https://www.iso.org/standard/61328.html`.

[43] S.Y. Jin, A. Pramanik, A.K. Basak, C. Prakash, S. Shankar, and S. Debnath. Burr formation and its treatments—a review. *International Journal of Advanced Manufacturing Technology*, 107:2189–2210, 2020. DOI: `https://doi.org/10.1007/s00170-020-05203-2`.

[44] R. Jochum, A. Rufin, T. Sisco, and F. Swanstrom. Fatigue considerations in the development and implementation of mechanical joining processes for commercial airplane structures. In A. Niepokolczycki and J. Komorowski, editors, *ICAF 2019 – Structural Integrity of Additively Manufactured Components*, pages 215–227. Springer International Publishing, Cham, 2020. DOI: `https://doi.org/10.1007/978-3-030-21503-3_17`.

[45] J. Kim, S. Min, and D.A. Dornfeld. Optimization and control of drilling burr formation of aisi 304l and aisi 4118 based on drilling burr control charts. *International Journal of Machine Tools and Manufacture*, 41:923–936, 2001. DOI: `https://doi.org/10.1016/S0890-6955(00)00131-0`.

[46] L. Ko and J.E. Chang. Development of driii geometry for burr minimization in drilling. *CIRP Annals*, 51:45–48, 2001. DOI: `https://doi.org/10.1016/S0007-8506(07)60527-7`.

[47] S.-L. Ko and D.A. Dornfeld. A study on burr formation mechanism. *Journal of Engineering Materials and Technology*, 113:75–87, 1991. DOI: `https://doi.org/10.1115/1.2903385`.

[48] S.-L. Ko and J.-K. Lee. Analysis of burr formation in drilling with a new-concept drill. *Journal of Materials Processing Technology*, 113:392–398, 2001. DOI: `https://doi.org/10.1016/S0924-0136(01)00717-8`.

[49] A. Lacombe. *Influence du procédé de perçage sur l'intégrité de surface et la tenue en fatigue de pièces percées en AA2024T351.* PhD thesis, ICA - Institut Clément Ader, 2021.

[50] L.K. Lauderbaugh. Analysis of the effects of process parameters on exit burrs in drilling using a combined simulation and experimental approach. *Journal of Materials Processing Technology*, 209:1909–1919, 2009. DOI: `https://doi.org/10.1016/j.jmatprotec.2008.04.062`.

[51] S. Li, D. Zhang, C. Liu, and H. Tang. Exit burr height mechanistic modeling and experimental validation for low-frequency vibration-assisted drilling of aluminum 7075-t6 alloy. *Journal of Manufacturing Processes*, 56:350–361, 2020. DOI: `https://doi.org/10.1016/j.jmapro.2020.04.083`.

[52] T.R. Lin and R.-F. Shyu. Improvement of tool life and exit burr using variable feeds when drilling stainless steel with coated drills. *International Journal of Advanced Manufacturing Technology*, 16:308–313, 2000. DOI: `https://doi.org/10.1007/s001700050162`.

[53] H. Liu, X. Xu, J. Zhang, Z. Liu, Y. He, W. Zhao, and Z. Liu. The state of the art for numerical simulations of the effect of the microstructure and its evolution in the metal-cutting processes. *International Journal of Machine Tools and Manufacture*, 177:103890, 2022. DOI: `https://doi.org/10.1016/j.ijmachtools.2022.103890`.

[54] M. Abdel Mohsen Mahdy. Economic drilling conditions for a given deburring radius. *Journal of Materials Processing Technology*, 110:197–205, 2001. DOI: `https://doi.org/10.1016/S0924-0136(00)00876-1`.

[55] S.N. Melkote, T.R. Newton, C. Hellstern, J.B. Morehouse, and S. Turner. Interfacial burr formation in drilling of stacked aerospace materials. In J.C. Aurich and D. Dornfeld, editors, *Burrs - Analysis, Control and Removal*, pages 89–98. Springer Berlin Heidelberg, Berlin, Heidelberg, 2010. DOI: `https://doi.org/10.1007/978-3-642-00568-8_10`.

[56] M.E. Merchant. Mechanics of the metal cutting process. i. orthogonal cutting and a type 2 chip. *Journal of Applied Physics*, 16:267–275, 1945. DOI: `https://doi.org/10.1063/1.1707586`.

[57] S. Min, D.A. Dornfeld, J. Kim, and B. Shyu. Finite element modeling of burr formation in metal cutting. *Machining Science and Technology*, 5:307–322, 2001. DOI: `https://doi.org/10.1081/MST-100108617`.

[58] M. Movahhedy, M.S. Gadala, and Y. Altintas. Simulation of the orthogonal metal cutting process using an arbitrary lagrangian-eulerian finite-element method. *Journal of Materials Processing Technology*, 103:267–275, 2000. DOI: `https://doi.org/10.1016/S0924-0136(00)00480-5`.

[59] M.R. Movahhedy, Y. Altintas, and M.S. Gadala. Numerical analysis of metal cutting with chamfered and blunt tools. *Journal of Manufacturing Science and Engineering*, 124:178–188, 2002. DOI: `https://doi.org/10.1115/1.1445147`.

[60] Newman. Assessment of residual stresses and hole quality. Technical report, Federal Aviation Administration (FAA), 2009. URL: `https://www.tc.faa.gov/its/worldpac/techrpt/ar0756v1.pdf`.

[61] Oxford University Press. *Concise Oxford English Dictionary.* Oxford University Press, Oxford, UK, 13th edition, 2011.

[62] Z. Pan, S. Y. Liang, H. Garmestani, and D. S. Shih. Prediction of machining-induced phase transformation and grain growth of ti-6al-4v alloy. *International Journal of Advanced Manufacturing Technology*, 87:859—-866, 2016. DOI: `https://doi.org/10.1007/s00170-016-8497-4`.

[63] I.W. Park and D.A. Dornfeld. A study of burr formation processes using the finite element method: Part i. *Journal of Engineering Materials and Technology*, 122:221–228, 2000. DOI: `https://doi.org/10.1115/1.482791`.

[64] I.W. Park and D.A. Dornfeld. A study of burr formation processes using the finite element method: Part ii—the influences of exit angle, rake angle, and backup material on burr formation processes. *Journal of Engineering Materials and Technology*, 122:229–237, 2000. DOI: `https://doi.org/10.1115/1.482792`.

[65] R. Patil, S. Shinde, D. Marla, and S. Joshi. Experimental analysis of burr formation in drilling of ti-6al-4v alloy. *International Journal of Mechatronics and Manufacturing Systems*, 9:237, 2016. DOI: `https://doi.org/10.1504/IJMMS.2016.079591`.

[66] A. Pekelharing. Why and how does the chip curl and break. *CIRP Annals*, 12:144–147, 1964.

[67] L. Pilný. *High speed drilling of Aluminum plates.* PhD thesis, Brno University of Technology, 2011.

[68] L. Pilný, L. De Chiffre, M. Píška, and M.F. Villumsen. Hole quality and burr reduction in drilling aluminium sheets. *CIRP Journal of Manufacturing Science and Technology*, 5:102–107, 2012. DOI: `https://doi.org/10.1016/j.cirpj.2012.03.005`.

[69] A. Rana, G. Dongre, and S.S. Joshi. Analytical modeling of exit burr in drilling of ti6al4v alloy. *Sādhanā*, 44:133, 2019. DOI: `https://doi.org/10.1007/s12046-019-1114-0`.

[70] X. Rimpault, J.-F. Chatelain, J.E. Klemberg-Sapieha, and M. Balazinski. Burr height monitoring while drilling cfrp/titanium/aluminium stacks. *Mechanics & Industry*, 18:114, 2017. DOI: `https://doi.org/10.1051/meca/2015073`.

[71] J.M. Rodríguez, J.M. Carbonell, and P. Jonsén. Numerical methods for the modelling of chip formation. *Archives of Computational Methods in Engineering*, 27:387–412, 2020. DOI: `https://doi.org/10.1007/s11831-018-09313-9`.

[72] T. Régnier, B. Marcon, J. Outeiro, G. Fromentin, A. D'Acunto, and A. Crolet. Investigations on exit burr formation mechanisms based on digital image correlation and numerical modeling. *Machining Science and Technology*, 23:925–950, 2019. DOI: `https://doi.org/10.1080/10910344.2019.1636274`.

[73] L.K.L. Saunders. An exit burr model for drilling of metals. *Journal of Manufacturing Science and Engineering*, 123:562–566, 2001. DOI: `https://doi.org/10.1115/1.1383030`.

[74] F. Schäfer. *Entgraten: Theorie, Verfahren, Anlagen*. Otto-Krausskopf-Verlag, 1975.

[75] T. Shiozaki, Y. Tamai, and T. Urabe. Effect of residual stresses on fatigue strength of high strength steel sheets with punched holes. *International Journal of Fatigue*, 80:324–331, 2015. DOI: `https://doi.org/10.1016/j.ijfatigue.2015.06.018`.

[76] L.C. Da Silva, P.R. Da Mota, M.B. Da Silva, E.O. Ezugwu, and Á.R. Machado. Study of burr behavior in face milling of ph 13-8 mo stainless steel. *CIRP Journal of Manufacturing Science and Technology*, 8:34–42, 2015. DOI: `https://doi.org/10.1016/j.cirpj.2014.10.003`.

[77] T. Sisco. Achieving "one up assembly" by reduction of interface burr height in aluminum, graphite, and advanced titanium/graphite hybrid (tigr) material. pages 2003–01–2896, 2003. DOI: `https://doi.org/10.4271/2003-01-2896`.

[78] A.S. Sofronas. The formation and control of drilling burrs. Master's thesis, University of Detroit, 1975.

[79] A. Sokołowski. On burr height estimation based on axial drilling force. *Journal of Achievements in Materials and Manufacturing Engineering*, 43:734–742, n.d.

[80] M. Stalley. Investigation of manual one way assembly on primary wingbox structure. pages 2002–01–2633, 2002. DOI: `https://doi.org/10.4271/2002-01-2633`.

[81] J.S. Sun, K.H. Lee, and H.P. Lee. Comparison of implicit and explicit finite element methods for dynamic problems. *Journal of Materials Processing Technology*, 105:110–118, 2000. DOI: `https://doi.org/10.1016/S0924-0136(00)00580-X`.

[82] W. Tian, J. Hu, W. Liao, Y. Bu, and L. Zhang. Formation of interlayer gap and control of interlayer burr in dry drilling of stacked aluminum alloy plates. *Chinese Journal of Aeronautics*, 29:283–291, 2016. DOI: `https://doi.org/10.1016/j.cja.2015.11.002`.

[83] B. Yin, T. Wei, L. WenHe, H. Jian, and S. Xin. Investigation of correlation between interlayer gap and burr height in drilling of stacked al-7475 materials. *Proceedings of the Institution of Mechanical Engineers, Part B: Journal of Engineering Manufacture*, 231:1917–1930, 2017. DOI: `https://doi.org/10.1177/0954405415617671`.